

**A Novel, Planar, Microfluidic Junction for
Multiphase Flow, Exemplified through the
Production of Fusion Energy Targets,
Encapsulated Mouse Neuron Stem Cells and
Multi-Compartmental Capsules**

**By
Jin Li**

**A thesis submitted in fulfillment of the requirements for
the degree of Doctor of Philosophy in Engineering**

University of Cardiff, School of Engineering

September 2015

To Jǐnbǎo Lǐ, Jiān Wáng and Wén Xū

Table of contents

Table of contents	i
Figures	v
Tables	xxiii
Acknowledgements	xxiv
Abstract	xxvi
Abbreviation	xxviii
CHAPTER I. Introduction of Droplet Microfluidics	1
1.1 Introduction	2
1.2 Dimensionless numbers.....	4
1.3 Phase parameters	5
1.3.1 Interfacial tension	5
1.3.2 Viscosity	6
1.4 Fluid actuation	6
1.5 Droplet-forming junctions and regime	7
1.5.1 T-shaped junction	8
1.5.2 Flow focusing junction.....	9
1.5.3 Co-flow junction.....	10
1.6 Droplet processing.....	11
1.7 Applications of droplet based microfluidics.....	12
1.7.1 Synthesis of microparticles.....	12
1.7.2 Biomicrofluidics	18
1.8 Conclusion and scope of the thesis.....	22

References:	24
-------------------	----

CHAPTER II. A Novel Microfluidic Flow-Focusing Junction for the Generation of Multiple Emulsions Droplets and Microcapsules..... 41

2.1 Basic principles of multiple emulsions.....	42
---	----

2.2 Droplet microfluidics for solvent emulsification	44
--	----

2.3 The experiment.....	47
-------------------------	----

2.3.1 Chemicals and materials.....	47
------------------------------------	----

2.3.2 Microfluidic chip manufacture	48
---	----

2.3.3 Microfluidic device setup	49
---------------------------------------	----

2.3.4 Experiment and measurement	50
--	----

2.3.5 Computational fluid dynamic simulation	50
--	----

2.4 Result and discussion	51
---------------------------------	----

2.4.1 Cross-shaped flow focusing junction.....	51
--	----

2.4.2 Description of bat-wing junction geometry.....	51
--	----

2.4.3 Study of droplet formation in the bat-wing junction	52
---	----

2.4.4 Study of double emulsion droplets formation in the bat-wing junction.....	55
---	----

2.4.5 Further discussion.....	59
-------------------------------	----

2.5 Conclusion	59
----------------------	----

References:	60
-------------------	----

CHAPTER III. Mass Production of Polymeric Microcapsules for Inertial Confinement Fusion Target Fabrication via Planar Droplet Microfluidics 69

3.1 A brief overview of controllable nuclear fusion.....	70
--	----

3.1.1 Magnetic confinement fusion	71
3.1.2 Magnetized target fusion	72
3.1.3 Inertial confinement fusion.....	72
3.1.4 Current progress of ICF target fabrication	74
3.1.5 Droplet microfluidic for ICF target formation	77
3.2 Free radical polymerization	83
3.2.1 Thermal-initiated free radical polymerization.....	84
3.2.2 Photoinitiated free radical polymerization	84
3.3 Experiment	89
3.3.1 Material and chemicals.....	89
3.3.2 Solvent preparation.....	90
3.3.3 Photopolymerization of double emulsion droplets.....	90
3.3.4 MWCNT-TMPTA polymer nanocomposite preparation (MWCNT)	91
3.4 Results and discussion.....	92
3.4.1 Double emulsion formation.....	93
3.4.2 Photoinitiated polymerization of double emulsion droplets.....	96
3.4.3 MCNT-TMPTA nanocomposite	104
3.5 Conclusion.....	106
References:	108

CHAPTER IV. Mouse Neuron Stem Cell Encapsulation in Alginate

Microspheres via Droplet Microfluidics.....	113
4.1 Spinal cord injury	114
4.2 Stem cell therapy	117
4.3 Cell encapsulation using microfluidics	119

4.4 Experiment	120
4.4.1 Culture protocol for mouse neural stem cells	120
4.4.2 Passage procedure	121
4.4.3 Microfluidic experiment	122
4.4.4 Measurement	123
4.5 Result and discussion	123
4.5.1 Droplet formation	123
4.5.2 On-chip gelation of the alginate microgels	124
4.5.3 Live and dead cell assays	126
4.6 Conclusion	128
References:	129

CHAPTER V. Encapsulated Droplet Interface Bilayers via Droplet Microfluidics

.....	134
5.1 Synthetic biology	135
5.2 The experiment	141
5.2.1 Solvent preparation	141
5.2.2 Microfluidic device fabrication	141
5.2.3 Droplets generation and collection	142
5.3 Result and discussion	142
5.3.1 Formation of the double emulsion droplets	142
5.3.2 Bilayer formation	144
5.3.3 Interfacial reactions	147
5.4 Conclusion	153
References:	155

CHAPTER VI. Main Conclusions and Suggestions for Future Work	158
6.1 Main conclusions.....	159
6.2 Suggestion for future work.....	161

Figures

Figure 1.1 Demonstrations of microfluidics. **A.** A multi-inlet microfluidic chips for bio-application. **B.** Typical laminar flow in a microfluidic channel. **C.** A coin-size microfluidic device runs thousands of experiments at once. **D.** Photograph of a multiplexed latching valve test microfluidic device [15]. 2

Figure 1.2 Droplet-based microfluidics. **A.** The generation of monodispersed 30 μ m diameter oil-in-water droplets on a planar microfluidic chip. **B.** Bifurcation channels for breakup of droplets into small volumes. The scale bar is 200 microns [24]. 3

Figure 1.3 A. Parabolic-shaped velocity profile in a microchannel under conditions of pressure driven flow. **B.** Schematic drawing of electroosmotic flow, which is governed by the applied voltage, channel dimension, surface charge density, and the pH of the fluid. 7

Figure 1.4 Schematic drawings of main droplet forming junctions for microfluidics. The black lines indicate the layout of junctions. The blue shapes indicate the dispersed phase. The white shapes indicate the continuous phase. **A.** T-shaped junction. **B.** Flow focusing junction. **C.** Co-flowing junction..... 8

Figure 1.5 T-shaped droplet forming junction. **A.** Top view of a T-shaped junction fabricated on a PMMA substrate [46]. **B.** Three regimes of droplet formation in a T-shaped junction as a function of flow velocity (U) and capillary number (Ca) [45]..... 9

Figure 1.6 Schematic drawing of droplet formation regime in a flow focusing junction. **A.** Squeezing regime. **B.** Dripping regime. **C.** Threading regime. **D.** Jetting regime [51]. 9

Figure 1.7 Microfluidic devices for droplet processing. **A.** Rapid mixing of fluids inside droplets by chaotic advection via the winding channel. [70] **B.** Time sequence images for droplet coalescence in a symmetrical chamber. [71] **C.** ESPCI LBC droplet sorting device. **D.** Droplet trapping and parking in a microfluidic array device. **E.** Inertial spiral-shaped microparticles separator [72]...... 11

Figure 1.8 Applications of droplet microfluidics. **A.** Highly uniform porous alginate scaffold generated by microfluidics devices. [73] **B.** Non-spherical microparticles with high aspect ratio. [74] **C.** High order multiple emulsions droplets. [75] **D.** Confocal images of triple polymersomes. [76] **E.** Microreactors for synthesis nanoparticles. [77] **F.** Polymeric microcapsules with a dimpled surface. [78] 12

Figure 1.9 Spherical microparticles produced via droplet microfluidics for drug delivery. **A.** High rate formation of Dex-HEMA microdroplets in a flow focusing junction. The scale bar represents 100 microns. [95] **B.** Monodispersed alginate beads produced via commercial microfluidic droplet generation system DG-200. The scale bar represent 200 microns. **C.** Monodispersed PLA microparticles for drug loading, produced via a capillary device [96]...... 14

Figure 1.10 Janus microparticles. **A.** Schematic drawing of Janus droplet formation in a flow focusing device [100]. **B.** Black-red photonic ETPTA Janus balls. Red

hemispheres contain 198nm silica particles [106]. **C.** DIC and corresponding fluorescent (insert) images of magnetic Janus particles, one containing magnetic nanoparticles, and the other containing rhodamine [105]. 15

Figure 1.11 Non-spherically shaped microparticles produced via droplet microfluidics. **A.** Micro fiber attained by the polymerization of a flowing polymer filament [115]. **B.** Dumbbell-shaped microparticles produced from hybrid Janus droplets. The scale bar represents 100 microns [116]. **C.** Monodispersed doughnut-shaped silica microparticles [117]. 16

Figure 1.12 Microcapsules for carbon capture and storage [124]. **A.** Carbonate/Semicoil double emulsion droplets formation in a capillary-based flow-focusing device. **B.** Cured Semicoil microcapsules on a microscope slide. **C, D.** Before and after the semicoil microcapsules have absorbed CO₂ within a continuous CO₂/N₂ flow up to 100 Celsius degrees. 18

Figure 1.13 Cell encapsulation via droplet microfluidics. **A.** A single cell encapsulation into a picolitre droplet [138]. **B.** Immortalized human cells encapsulated in alginate beads. **C.** Confocal images of cell-containing microgels stained with live/dead stains (24 hrs post-encapsulation) [139]. 19

Figure 1.14 Free interface diffusion in a Slipchip [147, 148]. **a.** A schematic of the SlipChip. Multiple precipitants, as well as multiple diffusion times for mixing the protein with each precipitant, can be applied on the same SlipChip. **b-e.** Schematic drawings of the protein (yellow) and precipitant mixing through sliding of the two

chip panels. **f.** The effect of diffusion time on the crystallization of the reaction centre of *Blastochloris viridis*. From left to right, the diffusion time is increases and more crystals are obtained. 20

Figure 1.15 Self-digitalized chip (SD). [156, 157] **A.** Schematic drawings of the circuit configuration and sequence images of sample digitalization procedure. **B.** An array contains 810 digitalized aqueous samples in immiscible oil phase. The scale bar represents 600 microns. **C.** Digital loop-mediated DNA amplification in a SD chip, which is used to quantify the relative and absolute changes in DNA concentration... 21

Figure 2.1 Schematic drawings of single emulsions and double emulsions...... 43

Figure 2.2 Schematic drawings of double emulsion formations via diverse layouts of microfluidic channels. **A.** Double emulsion droplets are formed in two-step method via serially connected double T-shaped junctions [30]. **B.** Double emulsion droplets are formed in one-step method via counter flow capillary devices. **C.** Double emulsion droplet are formed in two-step method via serially connect capillary devices [31]. 45

Figure 2.3 Bat-wing junction geometry and droplet formation regimes. **a,** Schematic drawing of the bat-wing junction geometry. The sizes of all the bat-wing junctions shown in this paper are as the one in this image. **b,** One-phase flow simulations with and without bifurcations when single phase fluid, flows from both the top and side inlets. The top inflow rate is 1ml/hour and the right and left inflows are both 1.6ml/hour. **c,** Two-phase simulations of water-in-oil droplet formation in jetting, dripping and squeezing regimes. The W/P input flow rates were 5/8, 2/8 and

2/0.96 ml/hour, respectively. In row a(i), the yellow films illustrate the boundary between water phase and oil phase. The blue vacancies in yellow illustrate the water phase touching the top channel wall. **d**, Experimental images of water droplet (blue) formation in laminar oil phase (clear and red) in dripping regime (left and middle) and squeezing (right) regime with the blue/clear/red phases flow rate 2/32/8 and 2/0.28/0.28 ml/hour, respectively. All the emulsions are formed on the PTFE microfluidic chip. 47

Figure 2.4 Continuous phase flow oscillation at bi-furcate geometry. **a**, Time sequence images of droplet formation in sub squeezing regime 1. Water (blue) phase blocks the upstream bifurcations and the oil phase (clear and red) flows to the downstream bifurcations. The blue/clear/red phases flow rate are 2/8/8 ml/hr. **b**, Time sequence images of droplet formation in sub squeezing regime 2. Dispersed phase blocks all the bifurcations and continuous phase flows into the expansion zone from two directions. The blue/clear/red phases flow rates are 2/2.4/2.4 ml/hr. **c**, Time sequence images of two-phase droplet breakup simulation in sub squeezing regime 2. The arrows show the local flow direction. Eddy flow appears where the blockage happening (the expansion zone and the bifurcations) and the size changes by time. Colour gradient shows the pressure distribution. The top inlet is 1ml/hour and the side inlets are both 0.5ml/hour. **d**, Average continuous flow rates in the bifurcations in different droplet formation regimes. Numerical data was obtained from the CFD simulations result. The average flow rate at downstream bifurcation is measured at the cross section at the short white line shown in Figure 2.4c. The average continuous phase flow rate through the upstream bifurcation to the joint area was obtained by the total input (long white line) minus average bottom flow rate. 53

Figure 2.5 Control of droplet breakup location at bat-wing junction. **a**, coupled CFD simulations and laboratory experiments illustrate the different water droplet breakup location in oil at bat-wing junction. All dispersed phases input rate are 2ml/hr. The continuous phase flow rate, from left to right, are 0.28ml/hour, 0.52ml/hour, 0.64ml/hour and 1.60ml/hour, respectively. **b**, The relationship between the continuous phase flow rate with droplet breakup point and droplet size. When the continuous phase flow rate is increased, the droplet breakup location moves upward with droplet size reduction. 54

Figure 2.6 Multiple emulsions preparations at bat-wing junction. **a**, Schematic drawing of water/polymer/oil double emulsion formation in a stepwise mechanisms. **b**, Passive satellite droplet extinction. The time sequence images are showing the formation of satellite droplet, the stationary position of satellite droplet, and the coalescence of satellite droplet with incoming dispersed phase, respectively. **c**, Different volume ratios of W/P emulsion, from left to right, 0.03, 1, 1 and 2.33, respectively. The difference of the second and third images is the oil phase input flow rates, which are 1.8ml/hour and 2.2 ml/hour. The emulsion shear-off point is changed, and a secondary water droplet is produced and allocated in the following polymer segment. **d**, Single core water/TMPTA segment production frequency. Each point was measured from 30 sequenced produced segments recorded by high-speed camera. The average error is 0.78%. **e**, Size control of the asymmetric water cores. The water and the polymer phase flow rates are 0.25 ml/hour and 0.12 ml/hour for all the images and the oil phase flow rates are 1.24, 1.38, 1.65 and 1.80 ml/hour, respectively. **f**, Multicore double emulsion formation. From left to right, the core number is 7 (W/P

volume ratio=0.5), 7 (W/P volume ratio=1.5), 15 and 30, respectively. **g**, Various size water droplets with different dyes encapsulated in the polymer segments. 56

Figure 2.7 Solid polymeric capsules with various morphologies produced by our MFFD. All the scale bars indicate 500 microns. **a**, thin shell thickness, single core TMPTA capsule (water/polymer input ratio =3). **b-o**, Multicore NOA 61 capsules with controllable core number, produced by the same microfluidic system with the bat-wing junction. The water and polymer input rates are both 0.1ml/hr. The core numbers increase from 2 to 15 by changing oil phase flow rate gradually which are 4.5, 3, 2.4, 2, 1.8, 1.4, 1.3, 1.2, 1.1, 1.08, 1.02, 0.97, 0.48 and 0.31 (ml/hr), respectively. **r-t**, Polymeric capsules with multiple reagents water droplets inside. .. 58

Figure 3.1 Schematic drawing of the nuclear fusion of a deuterium molecule and a tritium molecule. The fusion creates a helium molecule, a free neutron, and releases 17.59 MeV energy. The temperature of the Sun’s core where the fusion reaction takes place is 15,000,000C, whereas on Earth the temperature in a fusion reactor needs to reach 150,000,000C..... 70

Figure 3.2 Magnetic confinement fusion. A. Schematic drawing of a Tokamak device and the principle of plasma confinement with magnetic fields. **B.** Photographs of JET’s internal structure. The attached image on the right shows its working condition, and the bright zone indicates where the fuel plasma has a lower temperature. 71

Figure 3.3 Magnetized target fusion. **A.** Schematic drawing of a magnetized target fusion reactor. **B.** Photograph of a MTF reactor developed by General Fusion. (Images source: <http://www.generalfusion.com/>) 72

Figure 3.4 Inertial fusion reaction. **A.** Schematic drawing of the directive drive laser ICF that high power laser beams deliver energy to the center of the reactor where **B.** a fusion target is sent to. **C.** Schematic drawing of the indirect drive laser ICF that a fusion target is placed in a ‘hohlraum’ and high intensity X-rays are used to trigger the fusion reaction. **D.** Schematic drawing of ICF target ignition..... 73

Figure 3.5 Inertial confinement fusion targets. **A.** Schematic drawing of ICF targets. **B-H.** Solid shells from diverse materials for ICF target fabrication. **B.** Beryllium [27]. **C.** Glass [23]. **D.** Silicone aerogel. [28] **E.** Diamond [29]. **F.** RF foam [30]. **G.** DVB foam. [44]. **H.** TMPTA foam [33]. 75

Figure 3.6 The procedure of TMPTA shell fabrication via capillary microfluidic devices. From top to bottom, the double emulsion droplets were formed using a triple orifice droplet generator, thermopolymerized in long tubing, and collected in a rotating flask. [ref5]..... 79

Figure 3.7 The reported work on RF foam shells for ICF target fabrication in University of Rochester, America. **A.** A planar microfluidic chip with double T-junctions for the oil/water/oil double emulsion droplets formation. **B.** Sequence images of EWOD process for the formation of oil/water/air double emulsion droplets.

C, D. Centering of double emulsion droplets suspended in a density gradient by applying an AC electric field..... 81

Figure 3.8 Factors influenced the performance of photopolymerization. A. Gel effect. **B.** Volume shrinkage and related internal stress during the photopolymerization..... 88

Figure 3.9 Formation of monodispersed water/TMPTA/mineral oil double emulsion droplets via a planar PTFE microfluidic chip. A. The double emulsion droplets were formed in a bat-wing junction without satellite droplets. The channel dimension is same as the ones demonstrated in Chapter 2. **B-D.** Double emulsion droplets flowed in the channel without coalescence. **E.** Primary droplets and satellite droplets. The large droplet tended to stay in the centerline while the small ones flowed near the wall [65]..... 93

Figure 3.10 Defects of solid TMPTA microcapsules. A-C. Photographs of solid TMPTA microcapsules with open windows on the surface. **A.** Water core leaks out from the open window. **D, E.** Photographs of solid TMPTA microcapsules with an axe-cleavage-like defect on the surface. **F.** Core offset of the solid TMPTA microcapsule. **G.** Photographs of non-spherical intact TMPTA microcapsules. All the scale bars are 250 microns except the one in G..... 97

Figure 3.11 Photopolymerization of water/TMPTA/mineral oil double emulsion droplets in straight tubing with single UV LED. A. Photograph of the experimental setup. **B.** Solid TMPTA microcapsules were collected in a glass beaker filled with

mineral oil. **C, D.** Monodispersed TMPTA microcapsules. Scale bars are 1 mm. **E.** Photograph of water core offsetting in spherical TMPTA microcapsules. Scale bar is 500 microns. **F-H.** X-ray tomography scans of a TMPTA microcapsule. **F, G.** Fitpoint deviation measurement of sample target showing deviation ($\pm 7\mu\text{m}$) around mean diameter of 1.44mm, equating to ~99% sphericity. **H.** X-ray tomography scan of water core offset. **I, J.** SEM images of a sample TMPTA microcapsule. **I.** Cracked TMPTA microcapsule. **J.** Surface of the shell..... 99

Figure 3.12 Photopolymerization of water/TMPTA/mineral oil double emulsion droplets in straight tubing with multiple UV LEDs. **A-C.** Photographs of the experimental setup. In **A**, the black arrow shows the straight outlet tubing in which the solid microcapsules flowed upwards. The chamber can hold up to four UV LEDs. In **C**, white plasticine was used to confine the UV irradiation area. **D-L.** Photographs of cured TMPTA microparticles with different number and arrangement of UV LEDs. All the other experiment setups were same. **D, E.** Photopolymerization via one UV LED. **D.** Small water core. The white circle indicated that the stress of polymerization broke up the water core. **E.** Large water core. The water leaked out from the microcapsule as the open window on the surface. **F, G.** Photopolymerization with two UV LEDs. **F.** The two LEDs were placed in the opposite position. White circles indicated the leakage of water core. **G.** The two LEDs were placed in the neighbor position with right angle. **H.** Photopolymerization with three UV LEDs. **I-L.** Photopolymerization with four UV LEDs. The results indicated that evenly UV irradiation improved the quality of microcapsules. Scale bar: **D**, 150 micron. **E-L**, 1mm..... 101

Figure 3.13 Photographs of solid TMPTA microcapsules produced by photopolymerization with four UV LEDs placed in the devised UV LED chamber. A-D are from the same experiment when the flow rates combination was 0.6/0.4/2.0/50.0 ml/hour for water phase/TMPTA phase/mineral oil phase/additional mineral oil phase. The scale bars are 500 microns. B and D are dark field images. Others are bright field images. E, F. The flow rates combination for this experiment was 0.5/0.2/0.8/50.0 ml/hour. The average shell thickness of microcapsules is 60 microns. The scale bars are 1mm. G. The flow rates combination for this experiment was 0.6/0.6/3.0/50.0 ml/hour. The concentricity of the capsule is 99.63%. The scale bar is 1mm. H. Different from other samples photopolymerized by continuous UV irradiation, this microcapsule was photopolymerized by 30ms UV irradiation in related experiment. The scale bar is 500 microns. 102

Figure 3.14 Sphericity (circles) and concentricity (triangles) of individual target shells. Capsule number does not imply the sequence production of shells. Dotted circles denotes minimum specification levels (‰) for use in an IFE reactor. Average sphericity is 98.43% with a 0.68% standard deviation. Best is 99.69%. Average concentricity is 98.44% with a 0.62% standard deviation. Best is 99.72 %. This group of samples has an average diameter 892.52µm with a 7.52 µm standard deviation, and average shell thickness is 65.23 µm with a 4.42 µm standard deviation. The yield rate of intact capsule is 100%. 102

Figure 3.15 FTIR absorbance spectra for the microcapsules with different UV irradiation times. Partially cured samples appear in the area between the uncured sample (dotted red) and the cured sample (dotted black). Note that all the samples

appear within the banding of the accuracy of the system (upper and lower dotted black), implying that they are all fully cured. The offset in tops of the peaks could be caused by the scans being random on different days and the calibration of the spectrometer changing..... 104

Figure 3.16 Photopolymerization of functionalized MCNT-TMPTA. A. The TEM images of functionalized MCNT dispersion in solid TMPTA. **B** indicates the edge of the TMPTA sample. **C.** Solid functionalized MCNT-TMPTA microcapsules. The black dots on the surface are MCNT aggregation. The scale bar is 1mm..... 105

Figure 3.17 Energy-dispersive X-ray spectroscopy of cured functionalized MCNT-TMPTA sample. A. EDX spectrum of the cured sample. **B.** Electron image of a high-density area. **C.** Carbon detection image of the same area as B. **D.** Si detection image of the same area as B..... 105

Figure 4.1 Schematic showing the sequence of interventions in the treatment of spinal-cord injury. Description of numbers in text [21]. 116

Figure 4.2 Stem-cell therapy for central neuron system disorders [53]. 117

Figure 4.3 Mouse neuron stem cells *in vitro*. A. Neuronspheres (Passage 13). Scale bar is 200 microns **B.** Single neuron stem cells, dissociated from P13 neuronspheres. (Passage 14). Scale bar is 100 microns. 121

Figure 4.4 Alginate microspheres formation. **A.** Sheath flow was formed at the first flow focusing junction on our planar PTFE microfluidic chip. The dark line was culture medium and the light ones were 3% alginate solution. The white arrow indicates the flow direction. The scale bar is 600 microns. **B.** The alginate droplet was sheared off at the bat-wing junction. The scale bar is 1.2 mm. **C.** The alginate microspheres flowed through outlet of the chip. The scale bar is 1.2 mm. 123

Figure 4.5 Three approaches for alginate microspheres gelation on chip. **A, B.** Shielding flow for the alginate gelation. Experiment reproduced from reference 65. **A.** Black arrow indicates the alginate solution. White arrow indicates neat mineral oil flow. Red arrow indicates the mineral oil with acetic acid. Scale bar is 800 microns. **B.** Alginate coalescence occurred in the channel. Scale bar is 800 microns. **C.** Acetic-bearing mineral oil was injected for alginate microspheres gelation from a bottom inlet. The black arrow indicates the bottom inlet. Scale bar is 1 mm. **D-F.** Acetic-bearing mineral oil (red) was injected from lateral channel. The black circles and the red circles indicate the adjacent alginate droplets. Scale bar is 300 microns. 126

Figure 4.6 Gelled hydrogel microparticles. **A, B.** Monodispersed alginate microgels produced using the manner of Figure 5C. **A.** Scale bar is 2mm. **C.** Monodispersed PEGDA microparticles produced using the manner of Figure 5D with photopolymerization. Scale bar is 100 microns. 126

Figure 4.7 Cells encapsulation in alginate microspheres. Images were produced by Miss Lorena Hidalgo. **A, B.** Photographs of mouse neuron stem cells encapsulated in alginate microspheres. **A.** Scale bar is 400 microns. **B.** Scale bar is 250 microns. **C, D.**

Fluorescence image of GFP expressing dental pulp stem cells. Scale bar is 300 microns. **E.** First 3-day viability and proliferation of the encapsulated cells in alginate microspheres were measured with MTT assay. This is evidence that the cells can stand the encapsulation process and survive inside the microgels *in vitro*. 127

Figure 5.1 Compartment based microfluidic chip for simultaneous determination of gene expression and enzyme activity [28]..... 137

Figure 5.2 Functionalized microfluidics modules for biological researches. A. Schematic drawings of droplet solid phase extraction system for DNA extraction [32]. **B.** Photograph of a microfluidic device to generate fluid gradients [30]. **C.** Schematic drawing of optical tweezers utilized in microfluidics for cells and particles sorting [33]. 138

Figure 5.3 Bilayers and multisomes. A. Schematic drawing of three main structures of phospholipid assemblies in solution. **B.** Schematic drawing of a water/oil/water double emulsion droplet with encapsulated double interface bilayers. **C.** Schematic drawing of the multisomes with communication network by planting proteins in bilayers. **D-F.** Photographs of multisomes with diverse inner droplets [41]..... 140

Figure 5.4 Water/squalene/TMPTA double emulsion formation on a PMMA microfluidic chip. A. Water droplets were sheared off by squalene phase at the first droplet-forming junction. Scale bar is 600 microns. **B, C.** Double emulsion droplets formed at the bat-wing junction. **D.** Water droplets moved out from squalene segments without DPhPC when flowed in the channel. **E, F.** With the presence of

DPhPC in squalene phase, the double emulsion droplets were stabilized in the continuous flow. **G, H.** Squalene droplets with two water cores. B-H scale bars represent 1.2mm. 143

Figure 5.5 Photographs of bilayer formation on PMMA microfluidic chips. A. Two-core water/DPhDC-squalene/TMPTA double emulsion droplets stayed still in the curved PMMA channel. The white scale bar is 1.2mm. **B.** After 30s, most of the water droplets in squalene segments were coalesced to one. **C,D.** Two-core water/DPhDC-squalene/TMPTA double emulsion droplets in the devised chamber, forming bilayers at the water droplets interfaces. White arrow indicates the flow direction. The black scale bar is 250 microns. 145

Figure 5.6 Photographs of water/DPhDC-squalene droplet interface bilayer assemblies. The diameter of water droplet units is 250 microns. A-G. Diverse layouts of DIB networks. The squalene double emulsion droplets were merged together, and the encapsulated DIB assemblies combined with each other and formed diverse structures. **H-I.** The DIBs were disrupted by the droplet coalescence. **J-L.** These three images focused on the same DIB network and indicated that the DIBs were flexible, which could move around the water droplet surface (as seen of the ‘tail’). 146

Figure 5.7 Photographs of encapsulated DIBs of water/DPhDC-squalene/TMPTA double emulsion droplets. All scale bars are 250 microns. A. Two-core squalene microdroplets with encapsulated DIBs that the inner droplets were same. **B, C.** Two-core squalene microdroplets with encapsulated DIBs that the inner

droplets had different reagents and size. **D-F.** Diverse number of water droplets with DIBs confined in squalene droplets..... 146

Figure 5.8 Photographs of multisomes made from the water/DPhDC-squalene/alginate double emulsion template. A-I, Diverse layouts of multisome. A, B, E, and F have shown that bilayers were formed between internal water droplets and external alginate solution. **J, K.** The multisomes colonized together without coalescence and formed tissue-like structure. 147

Figure 5.9 A demonstration of Marangoni effect. A, B. Pepper was evenly sprinkled into the water in a petri dish. **C.** A drop of soap solution was dispensed to the center of the petri dish, which will create an interfacial tension gradient. **D, E.** After the soap droplet was dropped into the water, Marangoni instability drove the pepper to the edge of petri dish. 148

Figure 5.10 Mechanism of droplet motility in the solution environment [46-48].
A. Schematic drawing of the initial stages of oil droplet movement. Details can be found in related literature. **B.** Oleic anhydride was hydrolyzed in the presence of water at high pH and room temperature to form two amphiphiles. **C.** A demonstration of droplet (red) motility. The white line from top left to bottom right was the trail of the droplet movement, which was low pH and visualized by using pH-sensitive dye. 148

Figure 5.11 Time sequence images of the disruption of a double emulsion droplet with encapsulated DIBs. The scale bar is 500 microns. A. A squalene droplet with encapsulated DIBs flowed into the high pH water pool from a bottom inlet. **B-E.** The

squalene membrane containing oleic anhydride was disrupted as soon as the hydrolyzation reaction commenced. The bright boundary indicated where the reaction occurred and the squalene segments were repelled from the droplet to the edge of pool, which was dominated by the Marangoni effect. **F-H**. When the squalene had driven away, the water droplet based DIBs network was collapsed from outside to inside..... 149

Figure 5.12 Release of squalene droplets with encapsulated DIBs. **A**. Photograph of water/squalene/TMPTA/water multiple emulsions. Scale bar is 500 microns. **B-I**. Scale bars are 250 microns. **B, C**. While the squalene droplets moved to the boundary of TMPTA and water, the hydrolyzation of oleic anhydride commenced at the interface and drew the whole squalene segment out of the TMPTA phase to the external high pH water environment. **D**. The squalene membrane was disrupted and the DIBs network begun to collapse. The white dot circle showed the explosion of a water droplet. The white dusts are the product of oleic anhydride hydrolyzation. **E-I**. Sequence images of the squalene droplet release. **E**. Moving to the boundary. **F, G**. Oleic anhydride hydrolyzation and squalene membrane disruption. **H, I**. DIBs network collapse and water content release. 151

Figure 5.13 Photographs of squalene droplet motility with rotating encapsulated DIBs. **A-C**. The rotating of encapsulated DIBs network. The white arrow indicates the rotating direction of the water droplets. The water droplets would be released from the squalene droplets eventually. The white circle indicates the low pH zone that initiates the droplet movement. The scale bar is 1.5mm. **D-F**. The movement and ‘preying’ of squalene segment in high pH water solution. The squalene droplet moved

towards a double emulsion droplet with encapsulated DIBs, engulf it, and released the water content. This brought more oleic anhydride molecules into the primary squalene droplets, and repeating this process sustained the motility more than 20 minutes. The white arrows indicate the moving direction of the primary squalene droplets. The white circle indicates the 'food'. The black circle indicates other initiating squalene droplets. Somehow, they didn't move but oscillation at the original place. The scale bar is 1.5mm. 152

Tables

Table 1. Parameters of the droplet breakup models in COMSOL Multiphysics	51
Table 2. Specifications of ICF targets.	74
Table 3. Calculated concentricity and sphericity values of microcapsules cured with diverse UV exposure time.	103
Table 4. The Young's Modulus of photopolymerized polymer with ultrasonically mixed multi-walled Carbon nanotubes, with and without functional groups.	106
Table 5. Culture medium for mouse neural stem cell.....	121

Acknowledgements

First of all, I would like to express my sincere gratitude to my supervisor Prof. David Barrow for his continuous guidance and support on this study, for creative ideas and constructive advices to inspire the work, and for expertise and knowledge in microfluidics. Also, I would like to thank him for giving me the opportunities to cooperate with other research groups both inside and outside Cardiff University. It was a privilege for me to work with David.

Next, I would like to thank my colleagues, Dr. Alex Morgan, Miss Lily Giles, Dr. Erica Loizidou, Mr. Divesh Baxani, Miss Lorena Hidalgo, and their co-supervisor Prof. Bing Song and Dr. Oliver Castell for a successful collaboration. I would like to thank undergraduate students, Mr. Richard Sandberg, Mr. Mehrshad Ghahfarokhi, Mr. Jack Lindley-Start and Mr. Rishi Karla to work with me during their projects.

I would like to express my thanks to the technicians in the departments of Engineering, Chemistry, Bioscience, Dentistry, Optometry and Pharmacy, Cardiff University who helped me in their laboratories.

Most importantly, I would like to thank my father Dr. Jinbiao Li, and my mother Jian Wang, to whom this dissertation is dedicated. Without their encouragements and financial supports, I would not survive and complete my PhD study in UK. I would also like to express my thanks to Miss Wen Xu, who took care of every small part of my life in 2015, so that I could focus on the writing of my thesis. Every single letter, every single page in this thesis exists by virtue of these people to whom I am indebted.

DECLARATION

This work has not been submitted in substance for any other degree or award at this or any other university or place of learning, nor is being submitted concurrently in candidature for any degree or other award.

SignedDate

STATEMENT 1

This thesis is being submitted in partial fulfillment of the requirements for the degree of(insert MCh, MD, MPhil, PhD etc, as appropriate)

Signed Date

STATEMENT 2

This thesis is the result of my own independent work/investigation, except following collaboration: (i) Optical, fluorescence images of cell-bearing alginate microspheres, and MTT assay in Chapter IV were made by Lorena Hidalgo; (ii) DPhPC-bearing squalene and oleic anhydride water solution in Chapter V were prepared by Divesh Baxani.

Other sources are acknowledged by explicit references. The views expressed are my own.

Signed Date

STATEMENT 3

I hereby give consent for my thesis, if accepted, to be available for photocopying and for inter-library loan, and for the title and summary to be made available to outside organisations.

SignedDate

Abstract

Droplet microfluidics has been extensively studied in last two decades and found various applications in diverse research fields. In this thesis, we focused on the development of planar microfluidic devices, and explored their utility for the formation of multiple emulsions and microparticle fabrication. Here, a geometry variant flow-focusing junction was exhibited to control the location position of droplet breakup, and eliminate the satellite droplets. Then, this junction was tested to form monodispersed, multi-cored, double-emulsion droplets with controllable core numbers (up to 35) in a stepwise emulsification mechanism.

Based on the above device, three diverse applications of droplet microfluidics have been conducted: (1) the mass fabrication of polymeric microcapsules with high sphericity and concentricity for inertial confinement fusion (ICF) target fabrication; (2) the production of microgels to encapsulate mouse neuron stem cells for stem cell therapy in the treatment of spinal cord injury; and (3) the formation of squalene droplets with motility and encapsulated droplet interface bilayers for the ultimate creation of artificial cells.

Through the above, the following was achieved: (1) Single-core water/polymer/oil double emulsion droplets, as ICF target shells (for which sphericity and concentricity are paramount), were produced at tunable rates up to 20Hz. The polymeric microcapsules were solidified by using photopolymerization (minimum ultra violet exposure duration is 30ms) with an average $98.43\pm 0.68\%$ sphericity (best 99.69%), an average $98.44\pm 0.62\%$ concentricity (best 99.72%) and 100% yield rate; (2) Mouse neuron stem cells were encapsulated in alginate microspheres at 1 million cells/mL alginate. MTT assays were conducted to provide evidence that the cells survived the encapsulation process with continuous proliferation *in vitro*; and (3)

Various arrangements of encapsulated droplet interface bilayer network were observed, and the motility of double emulsion droplets was realized by continuous interfacial reactions, through which the expulsion and capture actions of squalene droplets were identified.

Abbreviation

AC	Alternating current
BSA	Bovine serum albumin
CAD	Computer-aided design
CEA	French alternative energies commission
CFD	Computational fluid dynamic
CNC	Computer numerical control
CNS	Central neuron system
CNT	Carbon nanotube
ddPCR	Droplet digital polymerase chain reaction
DIB	Droplet interface bilayer
DPhPC	Diphytanoylphosphatidylcholine
DT	Deuterium-tritium
DVB	Divinylbenzene
EDAX	Energy dispersive X-ray Spectroscopy
FEP	Fluorinated ethylene propylene
FTIR	Fourier transform infrared spectroscopy
GFP	Green fluorescent protein
HLB	Hydrophilic-lipophilic balance
HRTEM	High-resolution transmission electron microscope
ICF	Inertial confinement fusion
IPA	Isopropyl alcohol
ITER	International thermonuclear experimental reactor
JET	Joint European torus

LED	Light-emitting diode
LMJ	Le laser mégajoule
MCF	Magnetic confinement fusion
MCNT	Multi-walled carbon nanotubes
MEMS	Microelectromechanical systems
MFFD	Microfluidic flow focusing device
MTF	Magnetized target fusion
NSC	Neuron stem cell
PAN	Polyacrylonitrile
PCL	Polycaprolactone
PCR	Polymerase chain reaction
PDMS	Polydimethylsiloxane
PE	Polyethylene
PEEK	Polyether ether ketone
PEGDA	Polyethylene (glycol) diacrylate
PLA	Poly(lactic acid)
PLGA	Poly(lactic-co-glycolic acid)
PMMA	Poly(methyl methacrylate)
PNIPAm	Poly(N-isopropylacrylamide)
PS	Polystyrene
PTFE	Polytetrafluoroethylene
PVC	Polyvinyl chloride
RF	Resorcinol formaldehyde
SEM	Scanning electron microscope
SCI	Spinal cord injury

TMPTA	Trimethylolpropane triacrylate
UV	Ultra violet
VRMS	Voltage root mean square

CHAPTER I

Introduction of Droplet Microfluidics

1.1 Introduction

Microfluidic technology was developed in order to explore fluidic applications in micro scale [1-3]. Known as the ‘lab-on-a-chip’ or the micro total analysis system, it was originally designed to replicate most major chemical and biological laboratory experiments, but with reduced the reagent and energy consumption and with high feasibility and rapid response [4, 5]. Within this miniaturized apparatus, the fluid delivery is constrained in the laminar flow regime and dominated by surface forces. This offers several unparalleled advantages, such as short molecular diffusion distances and precise fluid delivery manipulation, as well as improvement to functional elements, including mixers [6], heaters [7], valves [8], and sensors [9,10]. Nowadays, microfluidics is a multidisciplinary field intersecting soft matter physics [11], analytical chemistry [12], engineering, and biotechnology [13], whereby low volume fluids are utilized to achieve multiplexing, automation and high-throughput screening [14] (Figure 1.1).

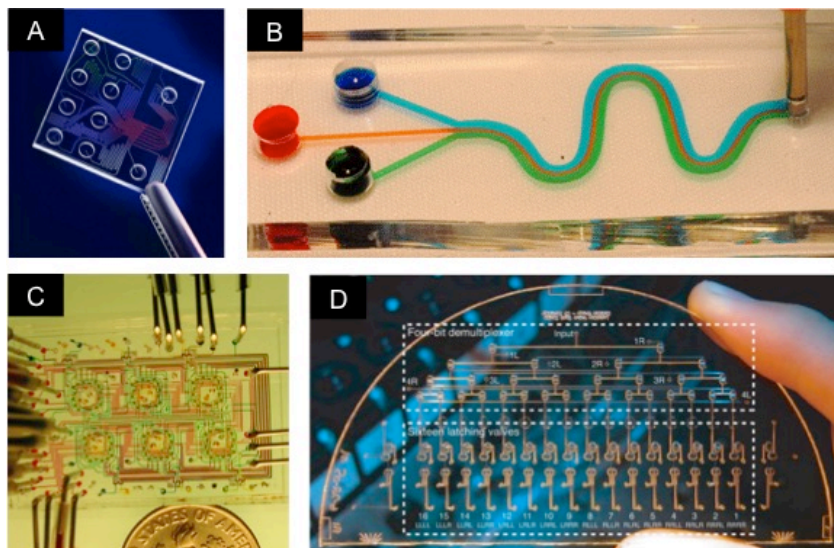


Figure 1.1 Demonstrations of microfluidics. **A.** A multi-inlet microfluidic chips for bio-application. **B.** Typical laminar flow in a microfluidic channel. **C.** A coin-size microfluidic device runs thousands of experiments at once. **D.** Photograph of a multiplexed latching valve test microfluidic device [15].

Droplet-based microfluidic technology, a subcategory of the microfluidics, involves the investigation of droplet formation, migration, and processing in laminar flow regimes [16,17]. As shown in Figure 1.2, it provides an efficient approach for producing monodispersed droplets at a high production rate and allows precise control of droplet size and morphology [18-21]. In a droplet microfluidic system, these microdroplets can be manipulated individually, and this offers the feasibility of conducting a large number of parallel reactions for high throughput experiments [22]. In the past decade, interest in droplet-based microfluidics systems has been growing substantially, and a diverse group of researchers are seeking novel solutions for chemical and biological applications that are superior to conventional techniques [23].

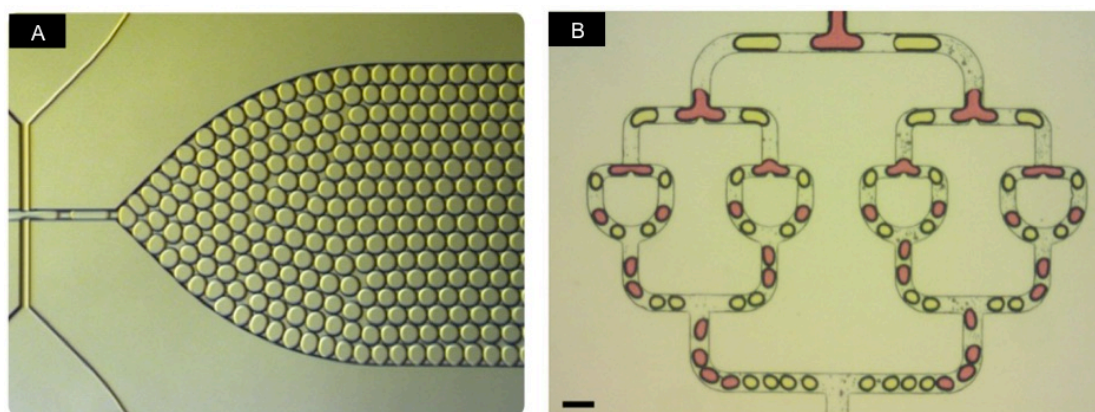


Figure 1.2 Droplet-based microfluidics. **A.** The generation of monodispersed 30 μ m diameter oil-in-water droplets on a planar microfluidic chip. **B.** Bifurcation channels for breakup of droplets into small volumes. The scale bar is 200 microns [24].

To devise an applicable droplet microfluidic device, it is necessary to have a clear understanding of the hydrodynamics and fluid behaviors in the laminar flow regime [25-27]. Three factors, including the channel geometry, the fluid properties and the inflow conditions, contribute to the multiphase flow that can be explained using dimensionless numbers [28].

1.2 Dimensionless numbers

In comparison to macro-hydronechanics, fluid delivery in multiphase microfluidics mainly depends on viscous, inertial, and interfacial forces. The Reynolds number (Re) is the most important dimensionless number in fluid dynamics to describe the ratio of inertial force to viscous force-

$$Re = \frac{\rho l u}{\mu},$$

whereby, ρ is fluid density, l is characteristic length scale (the dimension to define the scale of the fluidic system), u is velocity characteristic, and μ is fluid dynamic viscosity. In microfluidics, the value of Reynolds number is normally less than 10 due to the low velocity and miniature scale, and the fluid flow appears as typical parallel layers, namely laminar flow.

Another important dimensionless number in multiphase flow is the Bond number, which indicates the ratio of gravitational forces to interfacial forces-

$$Bo = \frac{\Delta\rho l^2 g}{\gamma},$$

whereby, $\Delta\rho$ is the density difference of the fluid, g is gravitational acceleration and γ is the interfacial tension. The value of Bond number is also small, since as in the laminar flow regime, the volume force is dominated by the surface force.

The Capillary number describes the relationship between viscous force and interfacial tension:

$$Ca = \frac{\mu u}{\gamma},$$

When the value of Capillary number is small, the effect of interfacial tension is greater than that of viscous force, and the droplet assumes a spherical form with a minimum surface area to volume ratio. With a high Capillary number, the viscous

force is dominated by the fluid delivery and it is difficult for droplets to maintain a spherical shape.

Other dimensionless numbers such as the Weber number (We) and Ohnesorge (Oh) number are used to describe the importance of the forces impacting on the hydrodynamics of multiphase microfluidics:

$$We = Re \cdot Ca = \frac{\rho u^2 l}{\gamma}, \quad Oh = \left(\frac{Ca}{Re}\right)^{1/2} = \frac{\mu}{(\rho l \gamma)^{1/2}}$$

1.3 Phase parameters

As described above, the surface forces dominate the fluid delivery in microfluidic system due to the downscaling of the fluidic devices and channel configurations [29]. The impact of gravity and inertial forces on multiphase flow rheology are negligible, while the shear and stress forces play important roles on dispersed phase breakup, and droplet movement. Several properties of fluidics are important for determining the droplet behavior in microfluidic systems, including interfacial tension and viscosity.

1.3.1 Interfacial tension

Interfacial tension is the elastic tendency that forces the liquids to acquire the least surface area possible. Due to the large surface-to-volume ratio of the droplets in microfluidics, the control of interfacial effects is essential for achieving replicated droplet formation. The addition of surfactants in the dispersed phase and continuous phase, are common methods for modifying interfacial tension [30,31], and their concentrations directly influence the droplet size formed in different droplet formation regimes of both T-shaped junctions and flow focusing junctions. The effects of the surfactant on the droplet formation process are complicated, in that the presence of surfactants not only reduces the equilibrium interfacial tension between

the immiscible fluids, but also induces an interfacial tension gradient in the dynamic droplet breakup.

1.3.2 Viscosity

The viscosity of a fluid is the parameter that describes its resistance to shape deformation, due to the velocity differences of the neighboring particles in fluids, by applied forces such as tensile stress and shear stress. In droplet microfluidics, the viscosities of both the dispersed phase and continuous phase influence the droplet size, depending on the microchannel properties and geometries. For instance, in straight-through microchannels, the droplet size is related more with dispersed phase viscosity rather than continuous phase viscosity [32]. To simplify the measurement of droplet formation physics, the viscous effect on droplet morphology is generally described using the dimensionless number Ca .

1.4 Fluid actuation

Two common methods are used to drive fluids in microchannels. One is pressure driven flow, whereby the fluid is pumped via positive displacement pumps such as syringe pumps [33]. An important phenomenon in pressure driven laminar flow is that the fluid velocity near the channel wall is extremely slow. This can be depicted using a parabolic velocity profile, which indicates the distribution of molecules transported within a channel (Figure 1.3A). Pressure driven flow can be a relatively simple and reproducible approach for delivering solvents to micro devices. With the development of the functional micro pumps, pressure driven flow is also amenable to miniaturization.

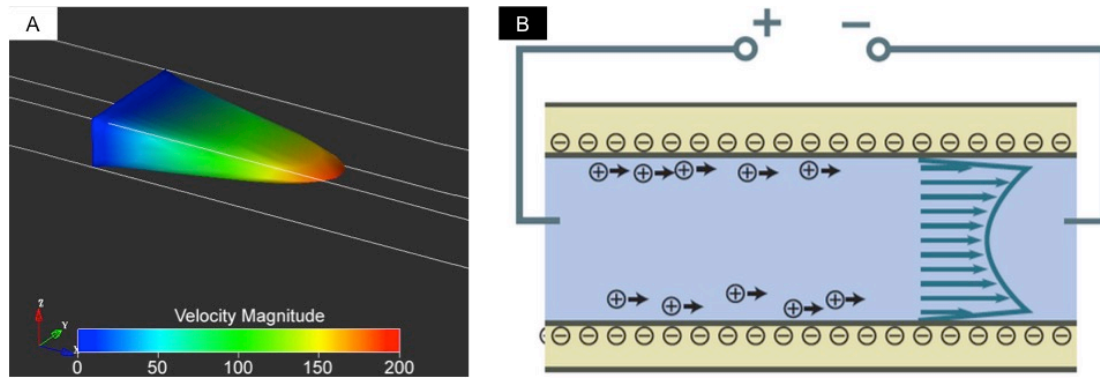


Figure 1.3 **A.** Parabolic-shaped velocity profile in a microchannel under conditions of pressure driven flow. **B.** Schematic drawing of electroosmotic flow, which is governed by the applied voltage, channel dimension, surface charge density, and the pH of the fluid.

Another common method for pumping fluids in microfluidic systems is electroosmotic flow [34]. This is achieved by applying an electric field across open microchannels, where there exists a highly charged surface, such as on silica, that force the ions in the electric double layer, and along the channel surface, to move towards the electrode of opposite polarity. This creates movement of the fluid near the walls, which translates via viscous forces into convective motion of the bulk fluid (Figure 1.3B). In comparison with pressure driven flow, the velocity profile of electroosmotic flow is uniform across the width of the channel, which prevents many diffusion non-uniformities. However, this manner often requires relatively high voltages, frequently of several kilovolts, dependent upon the capillary length, making it a difficult technology to miniaturize without off-chip power supplies.

1.5 Droplet-forming junctions and regime

A comprehensive microfluidic system contains several functional modules. Each module performs a specific operation on the passing fluids. The droplet-forming devices are the most important modules of the droplet-based microfluidics. They are utilized to disperse discrete droplets in an immiscible phase. Their structures play an important role on influencing dispersed phase breakup and attained droplet morphology [35]. At least three types of droplet forming devices have been developed:

the T-shape junction [36], flow focusing junction [37] and co-flow junction [38] (Figure 1.4). Their configurations, droplet breakup mechanisms, and droplet forming

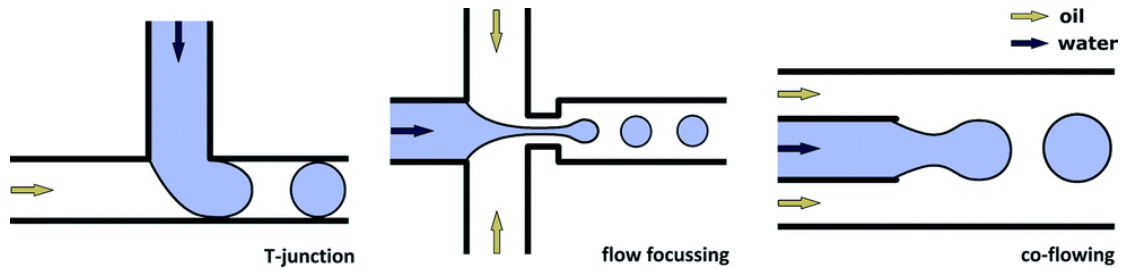


Figure 1.4 Schematic drawings of main droplet forming junctions for microfluidics. The black lines indicate the layout of junctions. The blue shapes indicate the dispersed phase. The white shapes indicate the continuous phase. **A.** T-shaped junction. **B.** Flow focusing junction. **C.** Co-flowing junction.

regimes are described in the following sub-sections.

1.5.1 T-shaped junction

The T-shaped junction is the most common droplet-forming junction used to generate droplets in microfluidics [39-42]. It generally appears as a T-shaped intersection of two perpendicular channels, which are the meeting point of the dispersed phase and the continuous phase [36, 43]. The ratio of the channels widths (or ω , defined as $W_{vertical}/W_{horizontal}$), affects the performance of a T-junction. As shown in Figure 1.5B, when the dispersed phase is introduced from the perpendicular channel, different regimes of droplet formation arise (which are affected by the Capillary number value) [44, 45]. Since $\omega < 1$ and Ca is large ($\sim > 2.2 \times 10^{-2}$), the dispersed phase is more likely to intrude into the horizontal channel, forming a long neck in the continuous phase flow. The droplet is ruptured off when the interfacial tension, holding the dispersed phase neck, is disrupted by the shear force of the continuous phase flow. This mechanism of droplet formation is defined as the dripping regime [36, 42]. In another scenario, whereby $\omega \sim 1$ and the value of Ca is small ($\sim < 7.6 \times 10^{-4}$), the dispersed phase fills the horizontal channel and blocks the continuous phase flow. The increase in pressure difference across the dispersed

phase finger induces droplet breakup. This mechanism is called the squeezing regime. On some occasions, the two channels of the T-junction connect at an acute angle rather than at a right angle, so that the local flow pattern, pressure distribution and droplet formation can be modified [41].

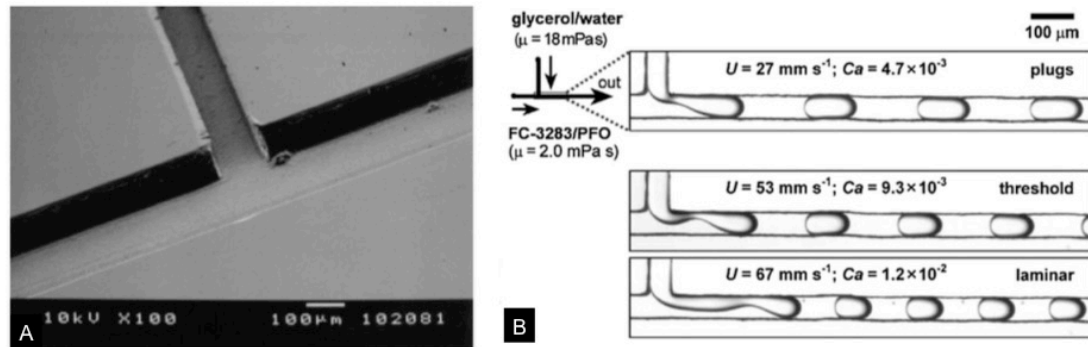


Figure 1.5 T-shaped droplet forming junction. **A.** Top view of a T-shaped junction fabricated on a PMMA substrate [46]. **B.** Three regimes of droplet formation in a T-shaped junction as a function of flow velocity (U) and capillary number (Ca) [45].

1.5.2 Flow focusing junction

The flow focusing junction is another popular droplet forming junction that has been described in several previous studies [47, 48]. It normally has a cross-shaped layout, wherein the dispersed phase is injected from the middle channel and pitched by the continuous phase from the sides. During droplet breakup, the Re value is normally very small (~ 0.01 to 1), and the viscous force dominates dynamic flow. The droplet is sheared off from its stream due to the capillary instability induced by the spatial constraints. Jetting [49], dripping, and squeezing droplet formation regimes have been observed, which are regulated by input flow rate and inlet pressure [50].

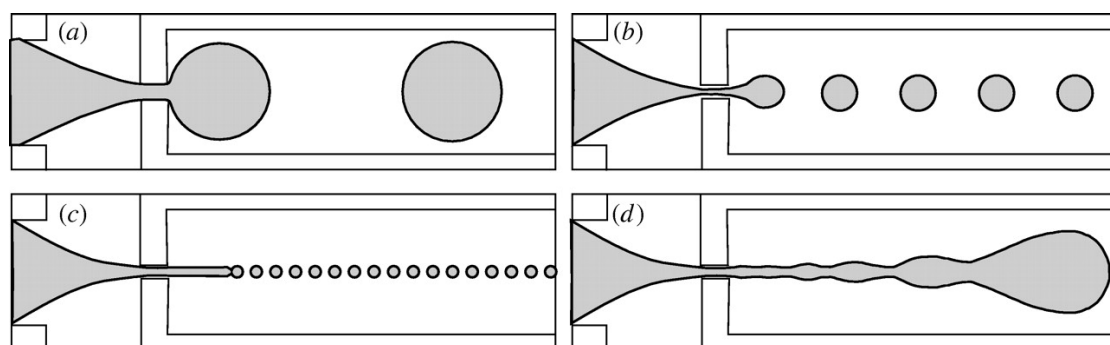


Figure 1.6 Schematic drawing of droplet formation regime in a flow focusing junction. **A.** Squeezing regime. **B.** Dripping regime. **C.** Threading regime. **D.** Jetting regime [51].

Compared with the T-junction, the flow focusing junction exhibits better control over the attained droplet size and monodispersity, resulting in increased productivity.

1.5.3 Co-flow junction

Co-flow junctions are also widely applied in droplet microfluidics [52, 53]. As shown in Figure 1.4, the dispersed phase is introduced in the middle of a continuous phase stream through a capillary [53, 54]. A sheath flow is formed as the dispersed phase is completely surrounded by the continuous phase. The level of Kelvin-Helmholtz instability induces droplet breakup when a linear velocity difference ($> 0.1m/s$) exists between the two involved phases. As in the case with flow focusing devices, three co-flow junction droplet formation regimes have been devised. The advantage of this type of junctions is that channel wetting issues can be avoided due to the dispersed phase does not contact with the wall during the droplet formation, thus preventing the failure of droplet formation.

Other droplet forming junctions, such as Y-shaped junctions and terrace-like junctions [55] have also been developed to fulfill specific requirements. In spite of the diversity of these layouts, droplet-forming junctions can be fabricated only from a limited range of materials. For capillary-based microfluidics, borosilicate glass is machined to form nozzles using a laser capillary puller [56], and precise alignments are required for the capillaries' interconnections [57, 58]. Metal needles and plastic tubes are inserted into the assembly, and epoxy glue is utilized to fix and seal the equipment. For a planar microfluidic system, a range of plastic materials (e.g. PDMS [59], PMMA, PTFE, PEEK) can be used as substrates. Lithographical methods [60, 61], etching techniques [62] and micromilling are used in the manufacture of functional modules on the planar chips.

1.6 Droplet processing

In addition to the droplet forming junctions, other functional modules have been developed. These modules either have fixed channel geometries, or they contain embedded MEMS elements that manipulate fluid delivery and sample processing [63]. Several examples of microfluidic modules that have been devised for specific objectives are shown in Figure 1.7, including detection and sorting, coalescence [64] and splitting [65, 66], and cooling and heating [67]. By integrating more microfluidic modules, a complex droplet based microfluidic system can be established to achieve specific biological or chemical functionalities, such as enzyme kinetic analysis [68] and molecule extraction [69].

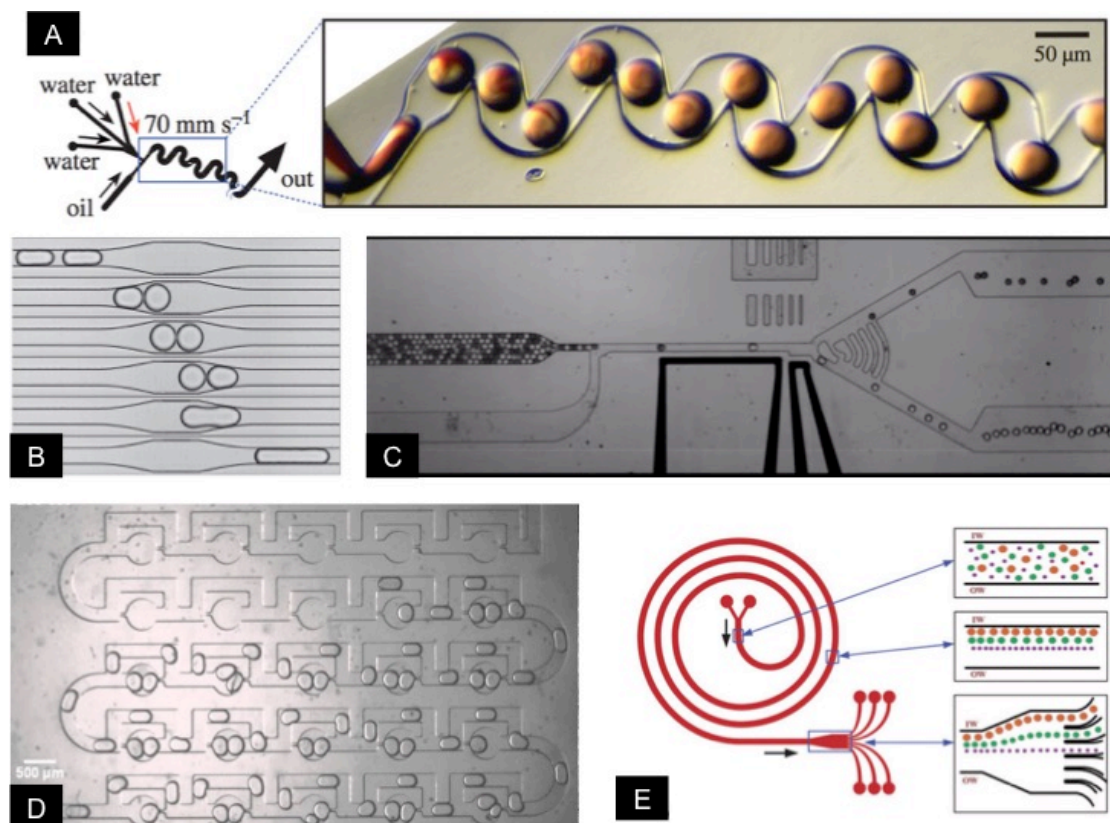


Figure 1.7 Microfluidic devices for droplet processing. A. Rapid mixing of fluids inside droplets by chaotic advection *via* the winding channel. [70] B. Time sequence images for droplet coalescence in a symmetrical chamber. [71] C. ESPCI LBC droplet sorting device. D. Droplet trapping and parking in a microfluidic array device. E. Inertial spiral-shaped microparticles separator [72].

1.7 Applications of droplet based microfluidics

As described above, droplet based microfluidic technology provides a platform on which to produce monodispersed droplets and to conduct high-level operations on them. This is a significant contribution to the synthesis of colloidal materials and analysis of the biological samples, in which high-throughput experimental results are difficult to attain using conventional methods. Several examples are shown in Figure 1.8. In this section, the current progress of droplet microfluidics in diverse fields has been reviewed.

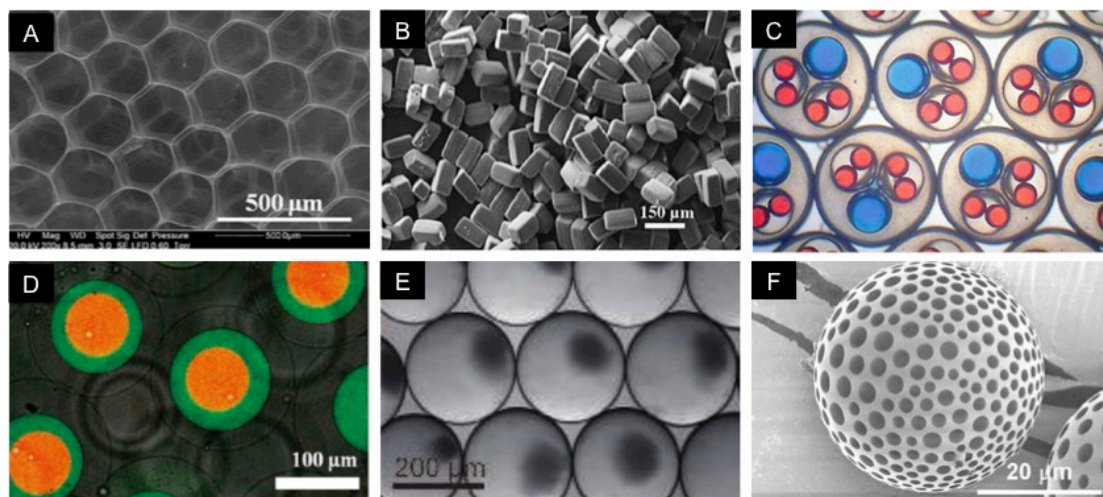


Figure 1.8 Applications of droplet microfluidics. **A.** Highly uniform porous alginate scaffold generated by microfluidics devices. [73] **B.** Non-spherical microparticles with high aspect ratio. [74] **C.** High order multiple emulsions droplets. [75] **D.** Confocal images of triple polymersomes. [76] **E.** Microreactors for synthesis nanoparticles. [77] **F.** Polymeric microcapsules with a dimpled surface. [78]

1.7.1 Synthesis of microparticles

An important application of droplet based microfluidics is the fabrication of highly uniform microparticles. Monodispersed emulsion droplets formed at microfluidic junctions are ideal templates for microparticles. Their size and morphology are determined by the channel configuration and the inflow parameters [79, 80]. Phase solidification can be completed in an on-chip microreactor *via* suitable

consolidation mechanisms, such as phase evaporation [81] or the free radical polymerization [82-84]. In this section, several types of microparticles that can be produced in microfluidic devices are described, and applications covering a diverse range of fields are listed.

1.7.1.1 Spherical shape microparticles

In microfluidics, spherically shaped microparticles are produced from single emulsion droplets, provided that the dispersed phase is curable or contains curable reagents (Figure 1.9) [85]. Depending on the precursors, the generation processes of the droplets can be intricate, and they can produce particles of a wide variation in properties such as the porosity [86]. Spherical shape microparticles have been widely employed in the drug delivery research [87]. Drug ingredients are confined in the discrete droplets and are immobilized inside the solid matrix. The ingredients can be released consistently into circulation due to the high uniformity and narrow size distribution of the microparticles. With polymeric microparticles (e.g. PLGA [87, 88], PLA [89, 90], PCL [91]), the encapsulated drugs are released passively by diffusion or *via* degradation of the polymer. Microgels, which are composed of microparticles made from hydrogels, serve as smart drug couriers [92], in that the release of ingredients can be actively controlled. This is realized by the shrinking or swelling of the microgels in response to stimuli from the environment, such as a change in the pH, or in temperature. For instance, poly(N-isopropylacrylamide) (PNIPAm) is a common thermo responsive hydrogel material utilized to produce drug-encapsulated microparticles [93]. It shrinks dramatically, and releases the water (which contains the dissolved molecules) when the ambient temperature exceeds the volume phase transition temperature. In addition, the microgels can be functionalized by surface

treatment with antibodies or proteins, which performs advanced drug-targeting *via* the cell recognition and binding [94].

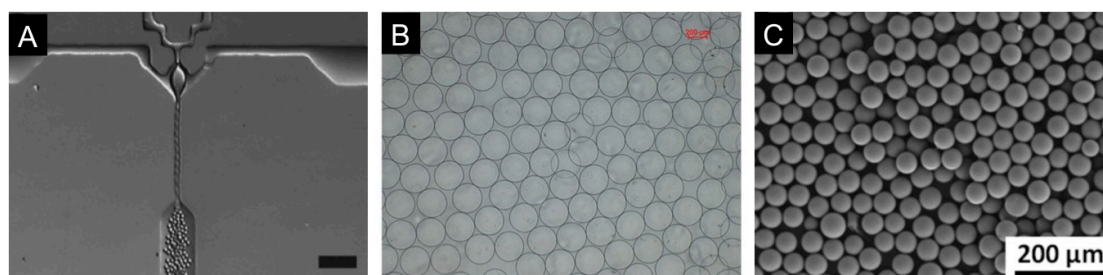


Figure 1.9 Spherical microparticles produced via droplet microfluidics for drug delivery. **A.** High rate formation of Dex-HEMA microdroplets in a flow focusing junction. The scale bar represents 100 microns. [95] **B.** Monodispersed alginate beads produced via commercial microfluidic droplet generation system DG-200. The scale bar represent 200 microns. **C.** Monodispersed PLA microparticles for drug loading, produced via a capillary device [96].

1.7.1.2 Janus microparticles

Multiphase anisotropic microparticles can be produced from droplets composed of several distinct phases [97]. In droplet based microfluidics, these droplets can be formed by injecting multiple dispersed phases into a single droplet generator, or by inserting capillary arrays inside the channel. Since the Reynolds numbers is always small, the stream remains parallel with negligible mixing between the fluid layers. Circulatory flow appears in each dispersed phase of the droplets and is confined in its own domain until the external stimuli disrupts it. As shown in Figure 1.10A, Janus microparticles are anisotropic microparticles fabricated from biphasic droplets [98-102]. The shape and surface properties of the two poles can be tuned by modifying the generation process [98]. These microparticles can gain multiple functionalities based on the ingredients, for instance, amphiphilic polymer microparticles [103]. In addition, advanced Janus colloidal microparticles can be produced by adding chemicals to one of the two phases (Figures 1.10B and 1.10C).

Solid/porous structure Janus microparticles are fabricated with the presence of a porogen in one of the monomers. Magnetic/non-magnetic Janus microparticles are produced by mixing magnetic nanoparticles with a precursor solution [104], and they can respond to a magnetic field with outputting diverse signals [100, 105].

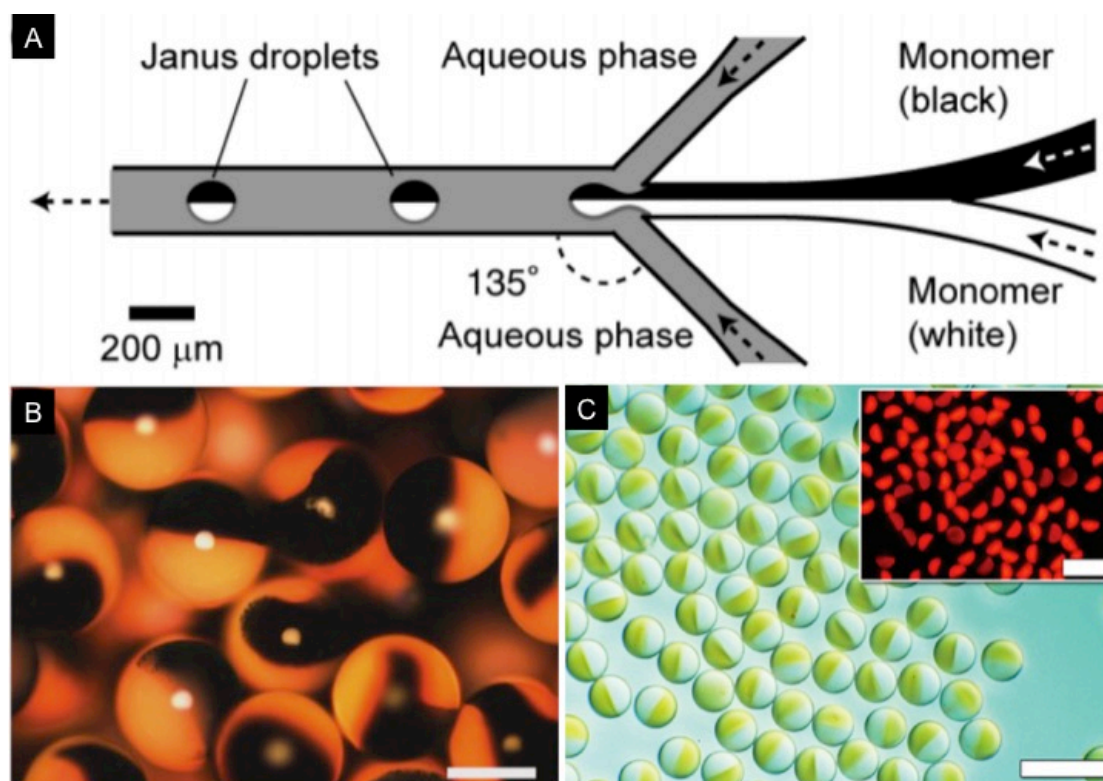


Figure 1.10 Janus microparticles. **A.** Schematic drawing of Janus droplet formation in a flow focusing device [100]. **B.** Black-red photonic ETPTA Janus balls. Red hemispheres contain 198nm silica particles [106]. **C.** DIC and corresponding fluorescent (insert) images of magnetic Janus particles, one containing magnetic nanoparticles, and the other containing rhodamine [105].

1.7.1.3 Non-spherically shaped microparticles

For droplet based microfluidics, the non-spherically shaped microparticles can be fabricated using a variety of methods [107]. The most directly approach is to utilize the spatial constraints of the channel to shape the emulsion droplets [108-110]. As the droplets moves through a capillary, (which is smaller than the droplets in at least one dimension), the dispersed phase will form slugs, or non-spherically shaped

droplets in the continuous phase. In this way, disc-shaped [111], rod-shaped [112], and wire-shaped [113-115] microparticles can be yielded with the assistance of in-situ solidification (Figure 1.11A). Another approach is to produce non-spherical microparticles from multiphase droplets [116]. Hemispherically shaped or dumbbell-shaped microparticles (Figure 1.11B) are yielded *via* a partial or full solidification process. An interesting method has been reported, whereby doughnut-shaped microparticles (Figure 1.11C) can be generated by an anisotropic dispersed phase diffusion and shrinkage within a dynamic continuous phase flow. [117, 118] The morphologies of these microparticles can be controlled since the flow rates affect the solvent diffusion rate.

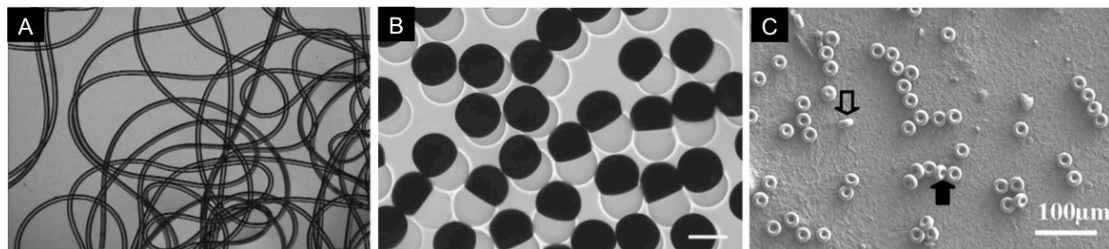


Figure 1.11 Non-spherically shaped microparticles produced via droplet microfluidics. **A.** Micro fiber attained by the polymerization of a flowing polymer filament [115]. **B.** Dumbbell-shaped microparticles produced from hybrid Janus droplets. The scale bar represents 100 microns [116]. **C.** Monodispersed doughnut-shaped silica microparticles [117].

1.7.1.4 Microcapsules

Uniform multiple emulsions droplets can be produced from serially connected droplet generators in multiphase microfluidic systems [119, 120]. The simplest multiple emulsions, double emulsions, consist of three phases: the inner phase, the shell phase and the continuous phase. The appearance of droplets is determined by the spreading parameter S , expressed as

$$S = \gamma_{\text{continuous phase,inner phase}} - (\gamma_{\text{continuous phase,shell phase}} + \gamma_{\text{inner phase,shell phase}}),$$

whereby $\gamma_{x,y}$ is the interfacial tension between the x and y fluids. Since the value of S is positive, intact core-shell shaped double emulsion droplets are formed, whereby the

inner phase is fully encapsulated in the shell phase. On the other hand, when S has a negative value, the inner phase is only partially engulfed by the shell phase, and the double emulsion droplets form an acorn shape. The core-shell shaped multiple emulsions droplets are used as templates for which the microcapsules are fabricated. The encapsulated inner phase provides a solvent medium for storing the reagents that enable further droplet processing. The shell phase serves as a barrier that physically separates the inner phase from the external environment. Selective mass transfers can be feasible, depending on the porosity of the hardened shell. Droplet based microfluidic systems enable the precise fabrication of microcapsules from customized multiple emulsions [121-123] with specific properties. For instance, gas permeable microcapsules made from Semicosil (a commercial silicon polymer) were fabricated *via* capillary microfluidic devices for carbon capture and storage (Figure 1.12). [124] The encapsulated inner phase contained saturated carbonates, solvent and a catalyst, whereby the solvent reacts with the carbon dioxide (CO_2) in the air to form bicarbonate. The captured carbon can be released by heating the microcapsules to 100 degree Celsius to reverse the reaction. Compared with other approaches, the method of encapsulating carbonates principally involves a much higher surface area of solvent in contact with the air, and thus allows for a significantly higher CO_2 absorbance rate. The microcapsules can be reused for more than 80 cycles of the CO_2 sorption and desorption, and have been explored for use in the purification of flue gas emissions in power stations.

Furthermore, multiple emulsions with complex inner morphologies can be formed in microfluidic devices. [125] This enables the fabrication of microcapsules containing multiple components that encapsulate various interacting materials [126, 127]. The microcapsule properties (such as shell thickness and reagent concentration)

are easy to adjust by tuning the flow rates. Their high uniformity allows for consistent microcapsule performance. It is not difficult to think of a microcapsule-based network that can be established to perform serial activities with high accuracy, for instance, chain chemical reactions, and sequential ingredients ejection. With the development of robust and easy-to-use devices, droplet based microfluidics will become more prominent in chemical and biological research.

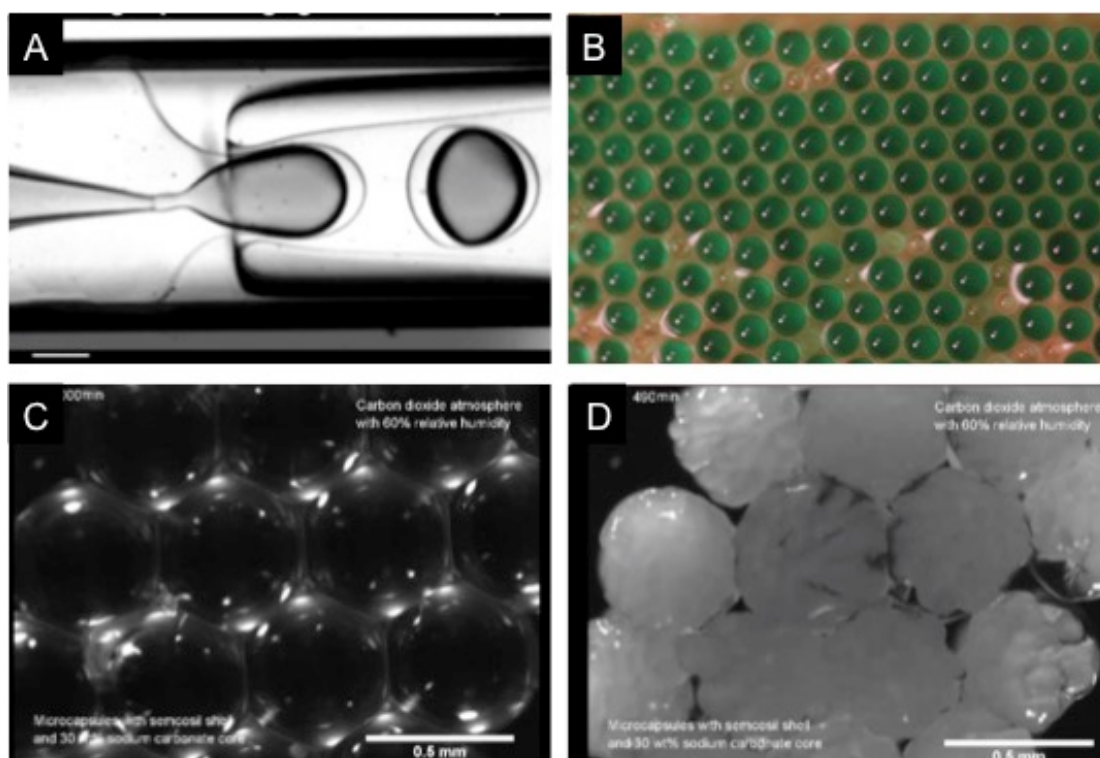


Figure 1.12 Microcapsules for carbon capture and storage [124]. A. Carbonate/Semicoil double emulsion droplets formation in a capillary-based flow-focusing device. B. Cured Semicoil microcapsules on a microscope slide. C, D. Before and after the semicoil microcapsules have absorbed CO₂ within a continuous CO₂/N₂ flow up to 100 Celsius degrees.

1.7.2 Biomicrofluidics

The development of microfluidics has significant implications for biology research. It not only allows for reduced consumption of reagents and samples [128, 129], but also allows for reduced experimental time, and increases the reliability and reproducibility of experimental results. In comparison with conventional buck

methods, droplet based microfluidics works as an efficient tool to supply large, samples-based throughput. The attained monodispersed microdroplets, which are ideal vessels for biological applications, provides thousands of parallel individual reactions with the economical usage of ingredients. The miniaturized fluid environment has specific heat and mass transfer, due to the laminar flow, that increases the reaction kinetics, as well as sample processing accuracy. The hydrodynamic flows enable the precise manipulation of each droplet, and thousands of samples can be analyzed in only a few seconds in functional microfluidic modules such as microarrays. For these reasons, droplet microfluidics has been employed in a variety of biological studies such as the enzymatic kinetics [130, 131], protein & DNA recognition [132], and cells behavior [133].

One significant application of droplet microfluidic technology in biological research is the encapsulation of living cells in monodispersed microgels made from biocompatible and biodegradable materials such as alginate [134] and PEGDA [135] (Figure 1.13). [136] As described previously, the droplet size, nutrient concentration and the samples' mechanical properties [137] are regulated by the fabrication process. The encapsulation of cells in microgels can protect them from the adverse external factors, such as a host's immune system, while allowing for selective molecular transfer to support the cells in-vivo [140-143]. This method has benefitted stem cell

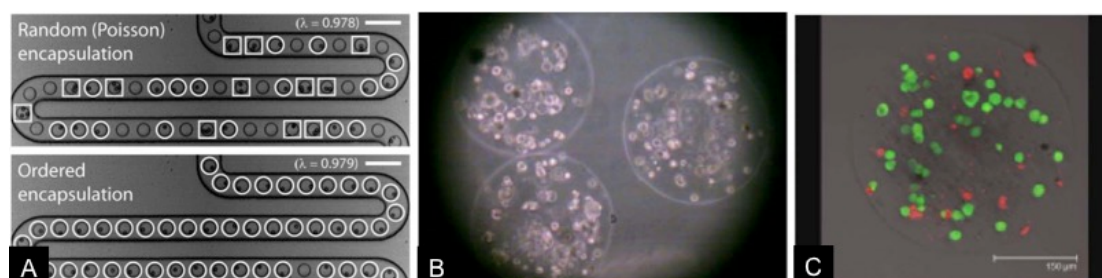


Figure 1.13 Cell encapsulation via droplet microfluidics. **A.** A single cell encapsulation into a picolitre droplet [138]. **B.** Immortalized human cells encapsulated in alginate beads. **C.** Confocal images of cell-containing microgels stained with live/dead stains (24 hrs post-encapsulation) [139].

therapy, whereby encapsulated living cells are injected in an effort to treat diseases such as Type I diabetes [144].

Another successful application of droplet microfluidics in biological research is the droplet digital polymerase chain reaction (ddPCR) [145, 146]. Polymerase chain reaction (PCR) assays have been developed to detect the presence and absence of specific DNA sequences in a sample through the enzymatic amplification of the target DNA sequence in a repeating thermocycling process. In comparison with traditional bulk PCR, ddPCR assays are composed of monodispersed droplets, and have the advantage of faster reaction kinetics, as well as accommodating a large number of samples for data collection (Figures 1.14 and 1.15). The produced droplets are collected off-chip in Eppendorf tubes, and then undergo thermocycling, or are transferred into a cytometer chip for data acquisition and analysis.

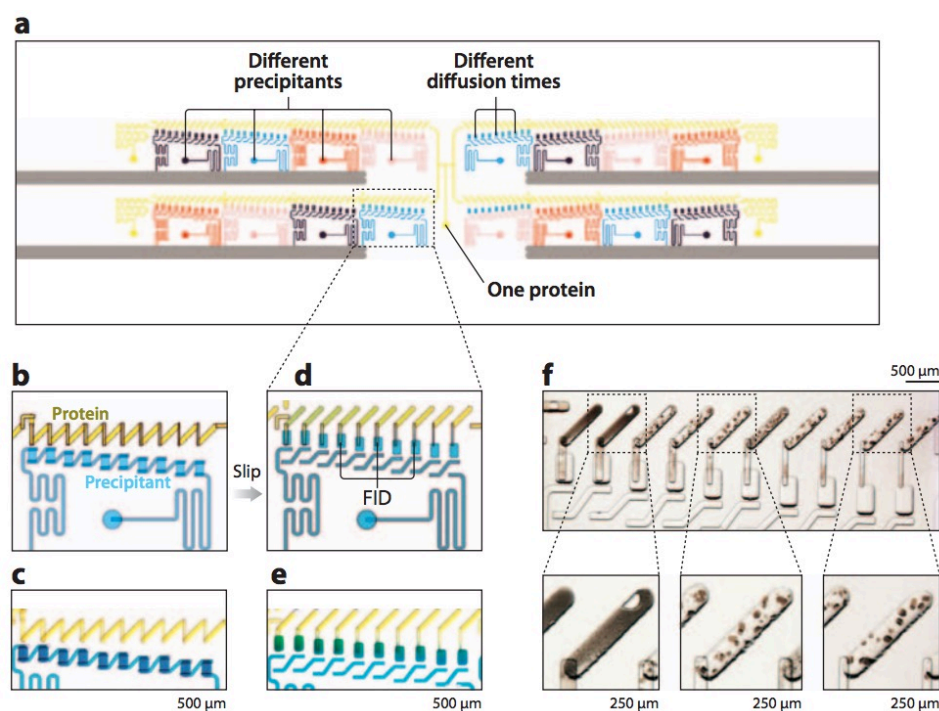


Figure 1.14 Free interface diffusion in a Slipchip [147, 148]. **a.** A schematic of the SlipChip. Multiple precipitants, as well as multiple diffusion times for mixing the protein with each precipitant, can be applied on the same SlipChip. **b-e.** Schematic drawings of the protein (yellow) and precipitant mixing through sliding of the two chip panels. **f.** The effect of diffusion time on the crystallization of the reaction centre of *Blastochloris viridis*. From left to right, the diffusion time is increases and more crystals are obtained.

With further development of microfluidic technology, the next generation of ddPCR is expected to perform a multistep process on a modulus-based microfluidic system. Droplet generation, thermocycling and the data generation will all be performed using the same substrate. This requires on-line droplet docking modules [149-155] that immobilize the samples for the chemical reactions and data read-out, and a feedback circuit for controlling the experimental parameters (e.g. temperature, pH, residence time). Based on this strategy, two ddPCRs have been designed, including the so-called SlipChip [148-150] and the self-digitalized chip (SD) [157, 158], both of which possess unique droplet formation and digitalization features.

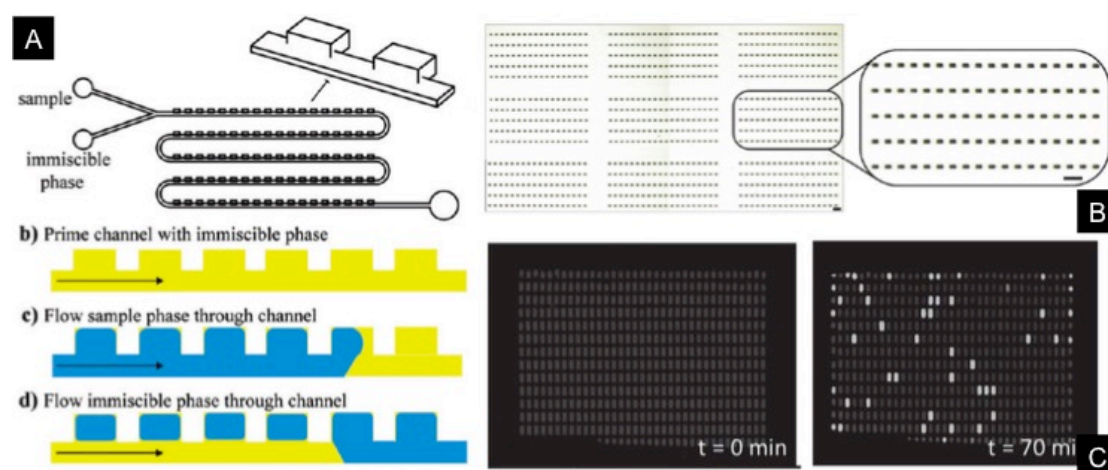


Figure 1.15 Self-digitalized chip (SD). [156, 157] **A.** Schematic drawings of the circuit configuration and sequence images of sample digitalization procedure. **B.** An array contains 810 digitalized aqueous samples in immiscible oil phase. The scale bar represents 600 microns. **C.** Digital loop-mediated DNA amplification in a SD chip, which is used to quantify the relative and absolute changes in DNA concentration.

Nowadays, more biology researchers are embracing the application of droplet microfluidics, including uses for single-cell screening, protein-crystal growth, and enzyme kinetic analysis [159-162]. The progress of new research fields such as synthetic biology require advanced tools to precisely manipulate miniaturized liquid samples for biological molecule recognition and modification [163]. On the other hand, the development of microfluidic technology is shifting from the design of individual functional elements to the building of comprehensive fluidic analysis

systems. This will be largely driven by multidisciplinary work, and should be enabled by future breakthroughs in integrated engineering.

1.8 Conclusion and scope of the thesis

Given the extensive evidence in recent literatures, it cannot be denied that the droplet microfluidics is a powerful tool for customized droplet synthesis and processing. Compared with conventional methods, droplet microfluidics provides an efficient solvent emulsification process, whereby a high standard in production properties can be attained. Indeed, this technology offers much to a wide range of research disciplines, but challenges also remain, especially the need for the development of robust, easy-to-use microfluidic devices for routine utilization.

This thesis concerns the design of planar microfluidic devices and the production of microparticles from selected emulsions templates for (1) inertial confinement target shell fabrication, (2) mouse neuron stem cell encapsulation, and (3) encapsulated droplet interface bilayers. The influence of channel configuration on the control of droplet formation, migration, and collection is investigated. On-chip droplet processing is also conducted, including phase consolidation and interfacial reactions, and several consequent phenomena are reported.

In Chapter II, a novel flow focusing junction called the bat-wing junction is detailed, and the droplet formation process in both computational fluidic dynamic simulations and laboratory experiments is described. The bat-wing junction is utilized for multiphase emulsification, and the generation of monodispersed multicore polymeric capsules with controllable morphologies.

In Chapter III, the mass production of single-core TMPTA polymeric capsules *via* the PTFE microfluidic devices for inertial confinement fusion (ICF) target fabrication is described. A water/TMPTA/oil double emulsion was employed as the

template, and formed in a two-step mechanism. The double emulsion droplets were consolidated by on-chip photoinitiated free radical polymerization, and the factors influencing the sphericity and concentricity of the solid shells have been studied. The incorporation of multiwall carbon nanotubes within the polymer matrix was also applied in order to enhance the mechanical property of the shells.

Chapter IV contains a method for the encapsulation of mouse neuron stem cells in the hydrogel microparticles in planar microfluidic devices. A detailed process for the encapsulation is provided, and the cell viability is briefly investigated. The ultimate objective of these microhydrogels is their use in stem cell therapy for the treatment of spinal cord injury.

In chapter V, the production of the encapsulated droplet interface bilayers on a planar PMMA microfluidic chip is exhibited. The functionalization of the attained droplets for the inducement of motility and for mimicking simple metabolisms by chain interfacial reactions are discussed. These are integral to the creation of an artificial biological membrane system, the purpose of which is to produce proto-cells for synthetic biology research.

The main conclusions of this thesis and suggestions for future research are prescribed in Chapter VI.

References:

1. Stone, H. A., Stroock, A. D., and Ajdari, A., "Engineering flows in small devices: microfluidics toward a lab-on-a-chip," *Annual Review of fluid Mechanics*, vol. 36, pp. 381-411, 2004.
2. Gravesen, P., Branebjerg, J., and Jensen, O. S., "Microfluidics-a review," *Journal of Micromechanics and Microengineering*, vol. 3, no. 4, p.168, 1993.
3. Xia, Y., Whitesides, G. M., "Soft lithography," *Annual Review of Materials Science*, vol. 28, no. 1, pp. 153-184, 1998.
4. Sinclair, J., Pihl, J., Olofsson, J., Karlsson, M., Jardemark, K., Chiu, D. T., and Orwar, O., "A cell-based bar code reader for high-throughput screening of ion channel-ligand interactions," *Analytical Chemistry*, vol. 74, no. 24, pp. 6133-6138, 2002.
5. Pihl, J., Karlsson, M., and Chiu, D. T., "Microfluidic technologies in drug discovery," *Drug Discovery Today*, vol. 10, no. 20, pp. 1377-1383, 2005.
6. Noroozi, Z., Kido, H., Micic, M., Pan, H., Bartolome, C., Princevac, M., Zoval, J., and Madou, M., "Reciprocating flow-based centrifugal microfluidics mixer," *Review of Scientific Instruments*, vol. 80, no. 7, pp. 075102, 2009.
7. Sadler, D. J., Changrani, R., Roberts, P., Chia-Fu, C., Frederic, Z., "Thermal management of BioMEMS: temperature control for ceramic-based PCR and DNA detection devices," *Components and Packaging Technologies, IEEE Transactions on*, vol. 26, no. 2, pp. 309-316, 2003.
8. Jeon, N. L., Chiu, D. T., Wargo, C. J., Wu, H. K., Choi, I. S., Anderson, J. R., and Whitesides, G. M., "Microfluidics section: design and fabrication of integrated passive valves and pumps for flexible polymer 3-dimensional microfluidic systems," *Biomedical Microdevices*, vol. 4, no. 2, pp. 117-121, 2002.
9. Ferguson, B. S., Buchsbaum, S. F., Swensen, J. S., Hsieh, K., Lou, X. H., and Soh, H. T., "Integrated microfluidic electrochemical DNA sensor," *Analytical Chemistry*, vol. 81, no. 15, pp. 6503-6508, 2009.
10. Kim, J., Junkin, M., Kim, D. H., Kwon, S., Shin, Y. S., Wong, P. K., and Gale, B. K., "Applications, techniques, and microfluidic interfacing for

- nanoscale biosensing,” *Microfluidics and Nanofluidics*, vol. 7, no. 2, pp. 149-167, 2009.
11. Shum, H. C., Abate, A. R., Lee, D., Studart, A. R., Wang, B., Chen, C. H., Thiele, J., Shan, R. K., Krummel, A., and Weitz, D. A., “Droplet microfluidics for fabrication of non-spherical particles,” *Macromolecular Rapid Communications*, vol. 31, no. 2, pp. 108-118, 2010.
 12. Fair, R. B., Khlystov, A., Taylor, T. D., Ivanov, V., Evans, R. D., Griffin, P. B., Vijay, S., Pamula, V. K., Pollack, M. G., and Zhou, J., “Chemical and biological applications of digital-microfluidic devices,” *Design & Test of Computers, IEEE*, vol. 24, no.1, pp. 10-24, 2007.
 13. Schaerli, Y., Hollfelder, F., “The potential of microfluidic water-in-oil droplets in experimental biology,” *Molecular Biosystems*, vol. 5, no. 12, pp. 1392-1404, 2009.
 14. Melin, J., and Quake, S. R., “Microfluidic large-scale integration: the evolution of design rules for biological automation,” *Annu. Rev. Biophys. Biomol. Struct.*, vol. 36, pp. 213-231, 2007.
 15. Grover, W. H., Ivester, R. H. C., Jensen, E. C., and Mathies, R. A., “Development and multiplexed control of latching pneumatic valves using microfluidic logical structures,” *Lab On A Chip*, vol. 6, no. 5, pp. 623-631, 2006.
 16. Chokkalingam, V., Herminghaus, S., and Seemann, R., “Self-synchronizing pairwise production of monodisperse droplets by microfluidic step emulsification,” *Applied Physics Letters*, vol. 93, no. 25, pp. 254101, 2008.
 17. Samie, M., Salari, A., and Shafii, M. B., “ Breakup of microdroplets in asymmetric T junctions,” *Physical Review E*, vol. 87, no. 5, pp. 053003, 2013.
 18. Serra, C., *Handbook of Micro Process Engineering*. Weinheim: Wiley-VCH, 2009.
 19. Serra, C. A., and Chang, Z., “Microfluidic-assisted synthesis of polymer particles,” *Chemical Engineering & Technology*, vol. 31, no. 8, pp. 1099-1115, 2008.

20. Hessel, V., Serra, C., Löwe, H., and Hadziioannou, G., "Polymerisationen in mikrostrukturierten reaktoren: ein überblick," *Chemie Ingenieur Technik*, vol. 77, no. 11, pp. 1693-1714, 2005.
21. Steinbacher, J. L., and McQuade, D. T., "Polymer chemistry in flow: new polymers, beads, capsules, and fibers," *Journal of Polymer Science Part A: Polymer Chemistry*, vol. 44, pp. 6505-6533, 2006.
22. Mukhopadhyay, R., "Diving into droplets," *Analytical Chemistry*, vol. 78, no. 5, pp. 1401-1404, 2006.
23. Mukhopadhyay, R., "Microfluidics: on the slope of enlightenment," *Analytical Chemistry*, vol. 81, no. 11, pp. 4169-4173, 2009.
24. Um, E., Rogers, M. E., and Stone, H. A., "Combinatorial generation of droplets by controlled assembly and coalescence," *Lab On A Chip*, vol. 13, no. 23, pp. 4674-4680, 2013.
25. Baroud, C. N., and Willaime, H., "Multiphase flows in microfluidics," *Comptes Rendus Physique*, vol. 5, no. 5, pp. 547-555, 2004.
26. Günther, A., and Jensen, K. F., "Multiphase microfluidics: from flow characteristics to chemical and materials synthesis," *Lab On A Chip*, vol. 6, no. 12, pp. 1487-1503, 2006.
27. Cristini, V., and Tan, Y. C., "Theory and numerical simulation of droplet dynamics in complex flows - a review," *Lab On A Chip*, vol. 4, no. 4, pp. 257-264, 2004.
28. Zhao, C. X., and Middelberg, A. P. J., "Two-phase microfluidic flows," *Chemical Engineering Science*, vol. 66, no. 7, pp. 1394-1411, 2011.
29. Stone, H. A., and Kim, S., "Microfluidics: basic issues, applications, and challenges," *AIChE Journal*, vol. 47, no. 6, pp. 1250-1254, 2001.
30. Xu, J. H., Luo, G. S., Li, S. W., and Chen, G. G., "Shear force induced monodisperse droplet formation in a microfluidic device by controlling wetting properties," *Lab On A Chip*, vol. 6, no. 1, pp. 131-136, 2006.
31. Wu, N., Zhu, Y., Leech, P. W., Sexton, B. A., Brown, S., and Easton, C., "Effects of surfactants on the formation of microdroplets in the flow focusing microfluidic device," *Biomems and Nanotechnology III*, vol. 6799, pp. 84-91, 2007.
32. Kobayashi, I., Mukataka, S., Nakajima, M., "Effects of type and physical properties of oil phase on oil-in-water emulsion droplet formation in

- straight-through microchannel emulsification, experimental and CFD studies,” *Langmuir*, vol. 21, no. 13, pp. 5722-5730, 2005.
33. Kamholz, A. E., and Yager, P., “Theoretical analysis of molecular diffusion in pressure-driven laminar flow in microfluidic channels,” *Biophysical Journal*, vol. 80, no. 1, pp. 155-160, 2001.
 34. Gaudioso, J., and Craighead, H. G., “Characterizing electroosmotic flow in microfluidic devices,” *Journal of Chromatography A*, vol. 971, no. 1, pp. 249-253, 2002.
 35. Nunes, J. K., Tsai, S. S. H., Wan, J., and Stone, H. A., “Dripping and jetting in microfluidic multiphase flows applied to particle and fibre synthesis,” *Journal of Physics D: Applied Physics*, vol. 46, no. 11, pp. 114002, 2013.
 36. Garstecki, P., Fuerstman, M. J., Stone, H. A., and Whitesides, G. M., “Formation of droplets and bubbles in a microfluidic T-junction-scaling and mechanism of break-up,” *Lab On A Chip*, vol. 6, no. 3, pp. 437-446, 2006.
 37. Anna, S. L., Bontoux, N., and Stone, H. A., “Formation of dispersions using “flow focusing” in microchannels,” *Applied Physics Letters*, vol. 82, no. 3, pp. 364-366, 2003.
 38. Xiong, R., Bai, M., and Chung, J. N., “Formation of bubbles in a simple co-flowing micro-channel,” *Journal of Micromechanics and Microengineering*, vol. 17, no. 5, pp.1002-1011, 2007.
 39. Zhao, L. B., Pan, L., Zhang, K., Guo, S. S., Liu, W., Wang, Y., Chen, Y., Zhao, X. Z., and Chan, H. L. W., “Generation of Janus alginate hydrogel particles with magnetic anisotropy for cell encapsulation,” *Lab On A Chip*, vol. 9, no. 20, pp. 2981-2986, 2009.
 40. Xu, J. H., Li, S. W., Tan, J., and Wang, Y. J., “Preparation of highly monodisperse droplet in a T - junction microfluidic device,” *AIChE Journal*, vol. 52, no. 9, pp. 3005-3010, 2006.
 41. Tan, J., Li, S. W., Wang, K., and Luo, G. S., “Gas-liquid flow in T-junction microfluidic devices with a new perpendicular rupturing flow route,” *Chemical Engineering Journal*, vol. 146, no. 3, pp. 428-433, 2009.

42. Xu, J. H., Li, S. W., Tan, J., and Luo, G. S., "Correlations of droplet formation in T-junction microfluidic devices: from squeezing to dripping," *Microfluidics and Nanofluidics*, vol. 5, no. 6, pp. 711-717, 2008.
43. Thorsen, T., Roberts, R. W., Arnold, F. H., and Quake, S. R., "Dynamic pattern formation in a vesicle-generating microfluidic device," *Physical Review Letters*, vol. 86, no. 18, pp. 4163-4166, 2001.
44. Tice, J. D., Lyon, A. D., and Ismagilov, R. F., "Effects of viscosity on droplet formation and mixing in microfluidic channels," *Analytica Chimica Acta*, vol. 507, no. 1, pp. 73-77, 2004.
45. De Menech, M., Garstecki, P., Jousse, F., and Stone, H. A., "Transition from squeezing to dripping in a microfluidic T-shaped junction," *Journal of Fluid Mechanics*, vol. 595, pp. 141-161, 2008.
46. Nisisako, T., Torii, T., and Higuchi, T., "Droplet formation in a microchannel network," *Lab On A Chip*, vol. 2, no. 1, pp. 24-26, 2002.
47. Utada, A. S., Fernandez-Nieves, A., Stone, H. A., and Weitz, G. A., "Dripping to jetting transitions in coflowing liquid streams," *Physical Review Letters*, vol. 99, no. 9, pp. 094502, 2007.
48. Eun, Y. J., Utada, A. S., Copeland, M. F., Takeuchi, S., and Weibel, D. B., "Encapsulating bacteria in agarose microparticles using microfluidics for high-throughput cell analysis and isolation," *ACS Chemical Biology*, vol. 6, no. 3, pp. 260-266, 2011.
49. Zhou, C., Yue, P., and Feng, J. J., "Formation of simple and compound drops in microfluidic devices," *Physics of Fluids*, vol. 18, no. 9, pp. 092105, 2006.
50. Abkarian, M., and Stone, H. A., "Microfluidic flow focusing: drop size and scaling in pressure versus flow-rate-driven pumping," *Electrophoresis*, vol. 26, pp. 3716-3724, 2005.
51. Sullivan, M. T., and Stone, H. A., "The role of feedback in microfluidic flow-focusing devices," *Philosophical Transactions of the Royal Society of London A: Mathematical, Physical and Engineering Sciences*, vol. 366, no. 1873, pp. 2131-2143, 2008.
52. Cramer, C., Fischer, P., and Windhab, E. J., "Drop formation in a co-flowing ambient fluid," *Chemical Engineering Science*, vol. 59, no. 15, pp. 3045-3058, 2004.

53. Hong, Y., and Wang, F., "Flow rate effect on droplet control in a co-flowing microfluidic device," *Microfluidics and Nanofluidics*, vol. 3, no. 3, pp. 341-346, 2007.
54. Hua, J., Zhang, B., and Lou, J., "Numerical simulation of microdroplet formation in coflowing immiscible liquids," *AIChE Journal*, vol. 53, no. 10, pp. 2534-2548, 2007.
55. Sugiura, S., Nakajima, M., Tong, J., Nabetani, H., and Seki, M., "Preparation of monodispersed solid lipid microspheres using a microchannel emulsification technique," *Journal of Colloid and Interface Science*, vol. 227, no. 1, pp. 95-103, 2000.
56. Quevedo, E., Steinbacher, J., and McQuade, D. T., "Interfacial polymerization within a simplified microfluidic device: capturing capsules," *Journal of the American Chemical Society*, vol. 127, no. 30, pp. 10498-10499, 2005.
57. Shum, H. C., Bandyopadhyay, A., Bose, S., and Weitz, D. A., "Double emulsion droplets as microreactors for synthesis of mesoporous hydroxyapatite," *Chemistry of Materials*, vol. 21, no. 22, pp. 5548-5555, 2009.
58. Utada, A. S., Lorenceau, E., Link, D. R., Kaplan, P. D., Stone, H. A., and Weitz, D. A., "Monodisperse double emulsions generated from a microcapillary device," *Science*, vol. 308, no. 5721, pp. 537-541, 2005.
59. Qiu, C., Chen, M., Yan, H., and Wu, H., "Generation of uniformly sized alginate microparticles for cell encapsulation by using a soft-lithography approach," *Advanced Materials*, vol. 19, no. 12, pp. 1603-1607, 2007.
60. Duffy, D. C., McDonald, J. C., Schueller, O. J. A., and Whitesides, G. M., "Rapid prototyping of microfluidic systems in poly (dimethylsiloxane)," *Analytical Chemistry*, vol. 70, no. 23, pp. 4974-4984, 1998.
61. McDonald, J. C., and Whitesides, G. M., "Poly (dimethylsiloxane) as a material for fabricating microfluidic devices," *Accounts of Chemical Research*, vol. 35, no. 7, pp. 491-499, 2002.
62. Perry, J. M., Harms, Z. D., and Jacobson, S. C., "3D nanofluidic channels shaped by electron - beam - induced - etching," *Small*, vol. 8, no. 10, pp. 1521-1526, 2012.

63. Tarn, M. D., Lopez-Martinez, M. J., and Pamme, N., "On-chip processing of particles and cells *via* multilaminar flow streams," *Analytical and Bioanalytical Chemistry*, vol. 406, no. 1, pp. 139-161, 2014.
64. Song, H., Tice, J. D., and Ismagilov, R. F., "A microfluidic system for controlling reaction networks in time," *Angewandte Chemie International Edition*, vol. 42, no. 7, pp. 792-796, 2003.
65. Skelley, A. M., Kirak, O., Suh, H., Jaenisch, R., and Voldman, J., "Microfluidic control of cell pairing and fusion," *Nature Methods*, vol. 6, no. 2, pp. 147-152, 2009.
66. Baroud, C. N., Gallaire, F., and Dangla, R., "Dynamics of microfluidic droplets," *Lab On A Chip*, vol. 10, no. 16, pp. 2032-2045, 2010.
67. Sgro, A. E., Allen, P. B., and Chiu, D. T., "Thermoelectric manipulation of aqueous droplets in microfluidic devices," *Analytical Chemistry*, vol. 79, no. 13, pp. 4845-4851, 2007.
68. Urban, P. L., Goodall, D. M., and Bruce, N. C., "Enzymatic microreactors in chemical analysis and kinetic studies," *Biotechnology Advances*, vol. 24, no. 1, pp. 42-57, 2006.
69. Yager, P., Edwards, T., Fu, E., Helton, K., Nelson, K., Tam, M. R., and Weigl, B. H., "Microfluidic diagnostic technologies for global public health," *Nature*, vol. 442, no. 7101, pp. 412-418, 2006.
70. Bringer, M. R., Gerdts, C. J., Song, H., Tice, J. D., and Ismagilov, R. F., "Microfluidic systems for chemical kinetics that rely on chaotic mixing in droplets," *Philosophical Transactions of the Royal Society of London A: Mathematical, Physical and Engineering Sciences*, vol. 362, no. 1818, pp. 1087-1104, 2004.
71. Bremond, N., Thiam, A. R., and Bibette, J., "Decompressing emulsion droplets favors coalescence," *Physical Review Letters*, vol. 100, no. 2, pp. 024501, 2008.
72. Kuntaegowdanahalli, S. S., Bhagat, A. A. S., Kumar, G., and Papautsky, I., "Inertial microfluidics for continuous particle separation in spiral microchannels," *Lab On A Chip*, vol. 9, no. 20, pp. 2973-2980, 2009.
73. Wang, C. C., Yang, K. C., Lin, K. H., Liu, H. C., and Lin, F. H., "A highly organized three-dimensional alginate scaffold for cartilage tissue

- engineering prepared by microfluidic technology,” *Biomaterials*, vol. 32, no. 29, pp. 7118-7126, 2011.
74. Baah, D., Tigner, J., Bean, K., Walker, N., Britton, B., and Floyd-Smith, T., “Microfluidic synthesis and post processing of non-spherical polymeric microparticles,” *Microfluidics and Nanofluidics*, vol. 12, no. 1-4, pp. 657-662, 2012.
75. Wang, W., Xie, R., Ju, X. J., Luo, T., Liu, L., Weitz, D. A., and Chu, L. Y., “Controllable microfluidic production of multicomponent multiple emulsions,” *Lab On A Chip*, vol. 11, no. 9, pp. 1587-1592, 2011.
76. Kim, S. H., Shum, H. C., Kim, J. W., Cho, J. C., and Weitz, D. A., “Multiple polymersomes for programmed release of multiple components,” *Journal of the American Chemical Society*, vol. 133, no. 38, pp. 15165-15171, 2011.
77. Jung, J. H., Park, T. J., Lee, S. Y., and Seo, T. S., “Homogeneous biogenic paramagnetic nanoparticle synthesis based on a microfluidic droplet generator,” *Angewandte Chemie*, vol. 124, no. 23, pp. 5732-5735, 2012.
78. Watanabe, T., Kimura, Y., and Ono, T., “Microfluidic fabrication of monodisperse polylactide microcapsules with tunable structures through rapid precipitation,” *Langmuir*, vol. 29, no. 46, pp. 14082-14088, 2013.
79. Xu, J. H., Chen, R., Wang, Y. D., and Luo, G. S., “Controllable gas/liquid/liquid double emulsions in a dual-coaxial microfluidic device,” *Lab On A Chip*, vol. 12, no. 11, pp. 2029-2036, 2012.
80. Wan, J., Bick, A., Sullivan, M., and Stone, H. A., “Controllable microfluidic production of microbubbles in Water-in-Oil Emulsions and the Formation of Porous Microparticles,” *Advanced Materials*, vol. 20, no. 17, pp. 3314-3318, 2008.
81. Shum, H. C., Lee, D., Yoon, I., Kodger, T., and Weitz, D. A., “Double emulsion templated monodisperse phospholipid vesicles,” *Langmuir*, vol. 24, no. 15, pp. 7651-7653, 2008.
82. Yang, B., Lu, Y., and Luo, G., “Controllable preparation of polyacrylamide hydrogel microspheres in a coaxial microfluidic device,” *Industrial & Engineering Chemistry Research*, vol. 51, no. 26, pp. 9016-9022, 2012.

83. Jagadeesan, D., Nasimova, I., Gourevich, I., Starodubtsev, S., and Kumacheva, E., "Microgels for the encapsulation and stimulus - responsive release of molecules with distinct polarities," *Macromolecular Bioscience*, vol. 11, no. 7, pp. 889-896, 2011.
84. Jeong, W. C., Lim, J. M., Choi, J. H., Kim, J. H., Lee, Y. J., Kim, S. H., Lee, G., Kim, J. D., Yi, G. R., and Yang, S. M., "Controlled generation of submicron emulsion droplets *via* highly stable tip-streaming mode in microfluidic devices," *Lab On A Chip*, vol. 12, no. 8, pp. 1446-1453, 2012.
85. Wang, J. T., Wang, J., and Han, J. J., "Fabrication of Advanced Particles and Particle - Based Materials Assisted by Droplet - Based Microfluidics," *Small*, vol. 7, no. 13, pp. 1728-1754, 2011.
86. Dubinsky, S., Zhang, H., Nie, Z., Gourevich, I., Voicu, D., Deetz, M., and Kumacheva, E., "Microfluidic synthesis of macroporous copolymer particles," *Macromolecules*, vol. 41, no. 10, pp. 3555-3561, 2008.
87. Xu, Q., Hashimoto, M., Dang, T. T., Hoare, T., Kohane, D. S., Whitesides, G. M., Langer, R., and Anderson, D. G., "Preparation of monodisperse biodegradable polymer microparticles using a microfluidic flow - focusing device for controlled drug delivery," *Small*, vol. 5, no. 13, pp. 1575-1581, 2009.
88. Enlow, E. M., Luft, J. C., Napier, M. E., and DeSimone, J. M., "Potent engineered PLGA nanoparticles by virtue of exceptionally high chemotherapeutic loadings," *Nano Letters*, vol. 11, no. 2, pp. 808-813, 2011.
89. Lassalle, V., and Ferreira, M. L., "PLA nano - and microparticles for drug delivery: an overview of the methods of preparation," *Macromolecular Bioscience*, vol. 7, no. 6, pp. 767-783, 2007.
90. Watanabe, T., Ono, T., and Kimura, Y., "Continuous fabrication of monodisperse polylactide microspheres by droplet-to-particle technology using microfluidic emulsification and emulsion-solvent diffusion," *Soft Matter*, vol. 7, no. 21, pp. 9894-9897, 2011.
91. Yang, C. H., Huang, K. S., Lin, Y. S., "Microfluidic assisted synthesis of multi-functional polycaprolactone microcapsules: incorporation of CdTe quantum dots, $Fe_3 O_4$ superparamagnetic nanoparticles and tamoxifen anticancer drugs," *Lab On A Chip*, vol. 9, no. 7, pp. 961-965, 2009.

92. Velasco, D., Tumarkin, E., and Kumacheva, E., "Microfluidic encapsulation of cells in polymer microgels," *Small*, vol. 8, no. 11, pp. 1633-1642, 2012.
93. Huang, S., Zeng, S., He, Z., and Lin, B. C., "Water-actuated microcapsules fabricated by microfluidics" *Lab On A Chip*, vol. 11, no. 20, pp. 3407-3410, 2011.
94. Zhang, Y., Chan, H. F., and Leong, K. W., "Advanced materials and processing for drug delivery: the past and the future," *Advanced Drug Delivery Reviews*, vol. 65, no. 1, pp. 104-120, 2013.
95. De Geest, B. G., Urbanski, J. P., Thorsen, T., Demeester, J., and Smedt, S. C. D., "Synthesis of monodisperse biodegradable microgels in microfluidic devices," *Langmuir*, vol. 21, no. 23, pp. 10275-10279, 2005.
96. Vladislavljević, G. T., Duncanson, W. J., Shum, H. C., and Weitz, D. A., "Emulsion templating of poly (lactic acid) particles: droplet formation behavior," *Langmuir*, vol. 28, no. 36, pp. 12948-12954, 2012.
97. Shah, R. K., Kim, J. W., and Weitz, D. A., "Janus supraparticles by induced phase separation of nanoparticles in droplets," *Advanced Materials*, vol. 21, no. 19, pp. 1949-1953, 2009.
98. Nie, Z., Li, W., Seo, M., Xu, S. Q., and Kumacheva, E., "Janus and ternary particles generated by microfluidic synthesis: design, synthesis, and self-assembly," *Journal of the American Chemical Society*, vol. 128, no. 29, pp. 9408-9412, 2006.
99. Nisisako, T., Torii, T., and Higuchi, T., "Novel microreactors for functional polymer beads," *Chemical Engineering Journal*, vol. 101, no. 1, pp. 23-29, 2004.
100. Nisisako, T., Torii, T., Takahashi, T., and Takizawa, Y., "Synthesis of monodisperse bicolored janus particles with electrical anisotropy using a microfluidic co - flow system," *Advanced Materials*, vol. 18, no. 9, pp. 1152-1156, 2006.
101. Shepherd, R. F., Conrad, J. C., Rhodes, S. K., Link, D. R., Marquez, M., Weitz, D. A., and Lewis, J. A., "Microfluidic assembly of homogeneous and janus colloid-filled hydrogel granules," *Langmuir*, vol. 22, no. 21, pp. 8618-8622, 2006.

102. Marquis, M., Renard, D., and Cathala, B., "Microfluidic generation and selective degradation of biopolymer-based Janus microbeads," *Biomacromolecules*, vol. 13, no. 4, pp. 1197-1203, 2012.
103. Chen, C. H., Shah, R. K., Abate, A. R., and Weitz, D. A., "Janus particles templated from double emulsion droplets generated using microfluidics," *Langmuir*, vol. 25, no. 8, pp. 4320-4323, 2009.
104. Kim, J. W., Utada, A. S., and Fernández-Nieves, A., "Colloidal assembly route for responsive colloidosomes with tunable permeability," *Nano Letters*, vol. 7, no. 9, pp. 1819-1822, 2007.
105. Yuet, K. P., Hwang, D. K., Haghgoie, R., and Doyle, P. S., "Multifunctional superparamagnetic Janus particles," *Langmuir*, vol. 26, no. 6, pp. 4281-4287, 2010.
106. Kim, S. H., Jeon, S. J., Jeong, W. C., Park, H. S., and Yang, S. M., "Optofluidic synthesis of electroresponsive photonic janus balls with isotropic structural colors," *Advanced Materials*, vol. 20, no. 21, pp. 4129-4134, 2008.
107. Yang, S. M., Kim, S. H., Lim, J. M., and Yi, G. R., "Synthesis and assembly of structured colloidal particles," *Journal of Materials Chemistry*, vol. 18, no. 19, pp. 2177-2190, 2008.
108. Champion, J. A., Katare, Y. K., and Mitragotri, S., "Making polymeric micro-and nanoparticles of complex shapes," *Proceedings of the National Academy of Sciences*, vol. 104, no. 29, pp. 11901-11904, 2007.
109. Xu, S. Q., Nie, Z. H., Seo, M., Lewis, P., Kumacheva, E., Stone, H. A., Garstecki, P., Weibel, D. B., Gitlin, I., and Whitesides, G. M., *Generation of monodisperse particles by using microfluidics: Control over size, shape, and composition*. *Angew. Chem., Int. Ed.* 2005, 5, pp. 724-728.
110. Hwang, D. K., Dendukuri, D., and Doyle, P. S., "Microfluidic-based synthesis of non-spherical magnetic hydrogel microparticles," *Lab On A Chip*, vol. 8, no. 10, pp. 1640-1647, 2008.
111. Dendukuri, D., Tsoi, K., Hatton, T. A., and Doyle, P. S., "Controlled synthesis of nonspherical microparticles using microfluidics," *Langmuir*, vol. 21, no. 6, pp. 2113-2116, 2005.

112. Seo, M., Nie, Z., Xu, S. Q., Lewis, P. C., and Kumacheva, E., "Microfluidics: from dynamic lattices to periodic arrays of polymer disks," *Langmuir*, vol. 21, no.11, pp. 4773-4775, 2005.
113. Dror, Y., Salalha, W., Avrahami, R., Zussman, E., Yarin, A. L., Dersch, R., Greiner, A., and Wendroff, J. H., "One-Step production of polymeric microtubes by co-electrospinning," *Small*, vol. 3, no. 6, pp. 1064-1073, 2007.
114. Puigmartí-Luis, J., Schaffhauser, D., Burg, B. R., and Dittrich, P. S., "A microfluidic approach for the formation of conductive nanowires and hollow hybrid structures," *Advanced Materials*, vol. 22, no. 20, pp. 2255-2259, 2010.
115. Jeong, W., Kim, J., Kim, S., Lee, S., Mensing, G., and Beebe, D. J., "Hydrodynamic microfabrication via "on the fly" photopolymerization of microscale fibers and tubes," *Lab On A Chip*, vol. 4, no. 6, pp. 576-580, 2004.
116. Prasad, N., Perumal, J., Choi, C. H., Lee, C. S., and Kim, D. P., "Generation of monodisperse inorganic-organic janus microspheres in a microfluidic device," *Advanced Functional Materials*, vol. 19, no. 10, pp. 1656-1662, 2009.
117. Fang, A., Gaillard, C., and Douliez, J. P., "Template-free formation of monodisperse doughnut-shaped silica microparticles by droplet-based microfluidics," *Chemistry of Materials*, vol. 23, no. 21, pp. 4660-4662, 2011.
118. Wang, B., Shum, H. C., and Weitz, D. A., "Fabrication of monodisperse toroidal particles by polymer solidification in microfluidics," *ChemPhysChem*, vol. 10, no. 4, pp. 641-645, 2009.
119. Chen, P. W., and Erb, R. M., "Studart A R. Designer polymer-based microcapsules made using microfluidics," *Langmuir*, vol. 28, no. 1, pp. 144-152, 2012.
120. Foster, T., Dorfman, K. D., and Davis, H. T., "Giant biocompatible and biodegradable PEG - PMCL vesicles and microcapsules by solvent evaporation from double emulsion droplets," *Journal of Colloid and Interface Science*, vol. 351, no. 1, pp. 140-150, 2010.

121. Nisisako, T., Okushima, S., and Torii, T., "Controlled formulation of monodisperse double emulsions in a multiple-phase microfluidic system," *Soft Matter*, vol. 1, pp. 23-27, 2005.
122. Okushima, S., Nisisako, T., Torii, T., and Higuchi, T., "Controlled production of monodisperse double emulsions by two-step droplet breakup in microfluidic devices," *Langmuir*, vol. 20, no. 23, pp. 9905-9908, 2004.
123. Saeki, D., Sugiura, S., Kanamori, T., Sato, S., and Ichikawa, S., "Microfluidic preparation of water-in-oil-in-water emulsions with an ultra-thin oil phase layer," *Lab On A Chip*, vol. 10, no. 3, pp. 357-362, 2010.
124. Aines, R. D., Spadaccini, C. M., Duoss, E. B., Stolaroff, J. K., Vericella, J., Lewis, J. A., and Farthing, G., "Encapsulated solvents for carbon dioxide capture," *Energy Procedia*, vol. 37, pp. 219-224, 2013.
125. Kim, S. H., Kim, J. W., Cho, J. C., and Weitz, D. A., "Double-emulsion drops with ultra-thin shells for capsule templates," *Lab On A Chip*, vol. 11, no. 18, pp. 3162-3166, 2011.
126. Ren, P. W., Ju, X. J., Xie, R., and Chu, L. Y., "Monodisperse alginate microcapsules with oil core generated from a microfluidic device," *Journal of Colloid and Interface Science*, vol. 343, no. 1, pp. 392-395, 2010.
127. Liu, L., Yang, J. P., Ju, X. J., Xie, R., Liu, Y. M., Wang, W., Zhang, J. J., Niu, H., and Chu, L. Y., "Monodisperse core-shell chitosan microcapsules for pH-responsive burst release of hydrophobic drugs," *Soft Matter*, vol. 7, no. 10, pp. 4821-4827, 2011.
128. Chang, Y. H., Lee, G. B., Huang, F. C., and Lin, J. L., "Integrated polymerase chain reaction chips utilizing digital microfluidics," *Biomedical Microdevices*, vol. 8, no.3, pp. 215-225, 2006.
129. Jary, D., Chollat-Namy, A., Fouillet, Y., Boutet, J., Chabrol, C., Castellan, G., Gasparutto, D., and Peponnet, C., "DNA repair enzyme analysis on EWOD fluidic microprocessor," *NSTI Nanotech 2006 Technical Proceedings*, vol. 2, pp. 554-557, 2006.
130. Di Carlo, D., Aghdam, N., and Lee, L. P., "Single-cell enzyme concentrations, kinetics, and inhibition analysis using high-density hydrodynamic cell isolation arrays," *Analytical Chemistry*, vol. 78, no. 14, pp. 4925-4930, 2006.

131. Di Carlo, D., Wu, L. Y., and Lee, L. P., "Dynamic single cell culture array," *Lab On A Chip*, vol. 6, no. 11, pp. 1445-1449, 2006.
132. Srisa-Art, M., deMello, A. J., and Edel, J. B., "High-throughput DNA droplet assays using picoliter reactor volumes," *Analytical Chemistry*, vol. 79, no. 17, pp. 6682-6689, 2007.
133. Yin, H., and Marshall, D., "Microfluidics for single cell analysis," *Current Opinion In Biotechnology*, vol. 23, no. 1, pp. 110-119, 2012.
134. Tan, W. H., Takeuchi, S., "Monodisperse alginate hydrogel microbeads for cell encapsulation," *Advanced Materials*, vol. 19, no. 18, pp. 2696-2701, 2007.
135. Panda, P., Ali, S., Lo, E., Chung, B. G., Hatton, T. A., Khademhosseini, A., and Doyle, P. S., "Stop-flow lithography to generate cell-laden microgel particles," *Lab Chip*, vol. 8, pp. 1056-1061, 2008.
136. Berthier, J., Le Vot, S., and Rivera, F., "Microfluidic system and corresponding method for transferring elements between liquid phases and use of said system for extracting said elements," *U.S. Patent Application*, vol. 13, no. 378,875, Jun 2010.
137. Ma, S., Natoli, M., Liu, X., Neubauer, M. P., Watt, F. M., Fery, A., and Huck, W. T. S., "Monodisperse collagen-gelatin beads as potential platforms for 3D cell culturing," *Journal of Materials Chemistry B*, vol. 1, no. 38, pp. 5128-5136, 2013.
138. Edd, J. F., Di Carlo, D., Humphry, K. J., Koster, S., Irimia, D., Weitz, D. A., and Toner, M., "Controlled encapsulation of single-cells into monodisperse picolitre drops," *Lab On A Chip*, vol. 8, no. 8, pp. 1262-1264, 2008.
139. Workman, V. L., Dunnett, S. B., Kille, P., and Palmer, D. D., "Microfluidic chip-based synthesis of alginate microspheres for encapsulation of immortalized human cells," *Biomicrofluidics*, vol. 1, no. 1, pp. 014105, 2007.
140. Lynn, D. M., and Langer, R., "Degradable poly (β -amino esters): synthesis, characterization, and self-assembly with plasmid DNA," *Journal of the American Chemical Society*, vol. 122, no. 44, pp. 10761-10768, 2000.

141. Hutmacher, D. W., "Scaffold design and fabrication technologies for engineering tissues—state of the art and future perspectives," *Journal of Biomaterials Science, Polymer Edition*, vol. 12, no. 1, pp. 107-124, 2001.
142. Wang, T., Lacik, I., Brissova, M., Anilkumar, A. V., Prokop, A., Hunkeler, D., Green, R., Shahrokhi, K., and Powers, A. C., "An encapsulation system for the immune-isolation of pancreatic islet," *Nat. Biotechnol.*, vol. 15, pp. 358-362, 1997.
143. Orive, G., Gascón, A. R., Hernández, R. M., Igartua, M., and Pedraz, J. L., "Cell microencapsulation technology for biomedical purposes: novel insights and challenges," *Trends In Pharmacological Sciences*, vol. 24, no. 5, pp. 207-210, 2003.
144. Chang, T. M. S., "Semi-permeable microcapsules," *Science*, vol. 146, pp. 524-526, 1964.
145. Vogelstein, B., and Kinzler, K. W., "Digital Pcr," *Proceedings of the National Academy of Sciences*, vol. 96, no. 16, pp. 9236-9241, 1999.
146. Baker, M., "Clever PCR: more genotyping, smaller volumes," *Nature Methods*, vol. 7, no. 5, pp. 351-356, 2010.
147. Du, W., Li, L., Nichols, K. P., and Ismagilov, R. F., "SlipChip," *Lab On A Chip*, vol. 9, no. 16, pp. 2286-2292, 2009.
148. Li, L., Du, W., and Ismagilov, R., "User-loaded SlipChip for equipment-free multiplexed nanoliter-scale experiments," *Journal of the American Chemical Society*, vol. 132, no. 1, pp. 106-111, 2010.
149. Zhao, Y., Pereira, F., deMello, A. J., Morgan, H., and Niu, X., "Droplet-based in situ compartmentalization of chemically separated components after isoelectric focusing in a Slipchip," *Lab On A Chip*, vol. 14, no. 3, pp. 555-561, 2014.
150. Edgar, J. S., Milne, G., Zhao, Y. Q., Pabbati, C. P., Lim, D. S. W., and Chiu, D. T., "Compartmentalization of chemically separated components into droplets," *Angewandte Chemie International Edition*, vol. 48, no. 15, pp. 2719-2722, 2009.
151. Huebner, A., Bratton, D., Whyte, G., Yang, M., DeMello, A. J., Abell, C., and Hollfelder, F., "Static microdroplet arrays: a microfluidic device for droplet trapping, incubation and release for enzymatic and cell-based assays," *Lab Chip*, vol. 9, no. 5, pp. 692-698, 2009.

152. Shim, J., Cristobal, G., Link, D. R., Thorsen, T., Jia, Y., Piattelli, K., and Fraden, S., "Control and measurement of the phase behavior of aqueous solutions using microfluidics," *Journal of the American Chemical Society*, vol. 129, no. 28, pp. 8825-8835, 2007.
153. Shim, J., Olguin, L. F., Whyte, G., Scott, D., Babbie, A., Abell, C., Huck, W. T. S., and Hollfelder, F., "Simultaneous determination of gene expression and enzymatic activity in individual bacterial cells in microdroplet compartments," *Journal of the American Chemical Society*, vol. 131, no. 42, pp. 15251-15256, 2009.
154. Schmitz, C. H. J., Rowat, A. C., Köster, S., and Weitz, D. A., "Dropspots: a picoliter array in a microfluidic device," *Lab On A Chip*, vol. 9, no. 1, pp. 44-49, 2009.
155. Hatch, A. C., Fisher, J. S., Pentoney, S. L., Yang, D. L., and Lee, A. P., "Tunable 3D droplet self-assembly for ultra-high-density digital micro-reactor arrays," *Lab On A Chip*, vol. 11, no. 15, pp. 2509-2517, 2011.
156. Hatch, A. C., Fisher, J. S., Tovar, A. R., Hsieh, A. T., Lin, R., Pentoney, S. L., Yang, D. L., and Lee, A. P., "1-Million droplet array with wide-field fluorescence imaging for digital PCR," *Lab On A Chip*, vol. 11, no. 22, pp. 3838-3845, 2011.
157. Cohen, D. E., Schneider, T., Wang, M., and Chiu, D. T., "Self-digitization of sample volumes," *Analytical Chemistry*, vol. 82, no. 13, pp. 5707-5717, 2010.
158. Gansen, A., Herrick, A. M., Dimov, I. K., Lee, L. P., and Chiu, D. T., "Digital LAMP in a sample self-digitization (SD) chip," *Lab On A Chip*, vol. 12, no. 12, pp. 2247-2254, 2012.
159. Jeffries, G. D. M., Edgar, J. S., Zhao, Y., Shelby, J. P., Fong, C., and Chiu, D. T., "Using polarization-shaped optical vortex traps for single-cell nanosurgery," *Nano Letters*, vol. 7, no. 2, pp. 415-420, 2007.
160. Zeigler, M. B., and Chiu, D. T., "Laser selection significantly affects cell viability following single - cell nanosurgery," *Photochemistry and Photobiology*, vol. 85, no. 5, pp. 1218-1224, 2009.
161. Courtois, F., Olguin, L. F., Whyte, G., Bratton, D., Huck, W. T. S., Abell, C., and Hollfelder, F., "An Integrated Device for Monitoring Time -

Dependent in vitro Expression From Single Genes in Picolitre Droplets,” *ChemBioChem*, vol. 9, no. 3, pp. 439-446, 2008.

162. Brouzes, E., Medkova, M., Savenelli, N., Marran, D., Twardowski, M., Hutchison, J. B., Rothberg, J. M., Link, D. R., Perrimon, N., and Samuels, M. L., “Droplet microfluidic technology for single-cell high-throughput screening,” *Proceedings of the National Academy of Sciences*, vol. 106, no. 34, pp. 14195-14200, 2009.
163. Gulati, S., Rouilly, V., Niu, X., Chappell, J., Kitney, R. I., Edel, J. B., Freemont, P. S., and DeMello, A. J., “Opportunities for microfluidic technologies in synthetic biology,” *Journal of The Royal Society Interface*, vol. 6, no. 4, pp. 493-506, 2009.

CHAPTER II

A Novel Microfluidic Flow-Focusing Junction for the Generation of Multiple Emulsions Droplets and Microcapsules

2.1 Basic principles of multiple emulsions

A simple emulsion contains two immiscible fluids, whereby one fluid (the dispersed phase) is immersed into the other (the continuous phase). Solvent emulsification, the mixing process, is the breakdown of large dispersed phase globules into small droplets *via* shaking, stirring, dispersing, homogenizing, or exposure to ultrasound [1]. As shown in Figure 2.1, there are two simple emulsions formed by water and oil: one is the water-in-oil emulsion (W/O), wherein the oil is the dispersed phase and the water is the continuous phase; and the oil-in-water emulsion as the opposite form [2]. The boundary between the water phase and oil phase is the interface, and interfacial tension tends to reduce the interface area in order to minimize the potential energy. Since emulsification is unspontaneous, a simple emulsion can be unstable [3]. The collapse of its geometric structure is induced by many factors such as external forces, the change in hydrophilic-lipophilic balance parameters (HLB), and the migration of droplets through the medium. Six types of emulsion breakdown have been identified: which are creaming, sedimentation, flocculation, phase inversion, coalescence, and Ostwald ripening [4, 5]. To extend the life of an emulsion, surfactants are added to the fluids to reduce the interfacial tension, and stabilize the droplet suspension by increasing the system's kinetic stability.

Multiple emulsions, also known as ‘emulsion of emulsion’, are complicated fluid systems, in which more than three phases exist simultaneously. Multiple emulsion systems are highly metastable due to the presence of several simple emulsions with thermodynamically unstable interfaces. One common method of stabilizing multiple emulsions is to add a group of surfactants with diverse hydrophilic-lipophilic balance (HLB) values, which are the parameters to degree the hydrophobicity of the surfactants. ($HLB=20*M_h/M$, which M_h is the molecular mass of the hydrophilic portion of the molecule and M is the whole molecular mass of whole molecule) For instance, Span 80 (HLB=4) and Tween 20 (HLB=16) are widely used surfactants in the W/O/W (or O/W/O) double emulsion system to stabilize the W/O and O/W interface, respectively. The concentration ratio of the surfactants is important in stabilizing the multiple emulsions. In addition, amphiphilic polymeric stabilizers can also be used to improve the stability of double emulsions [6,7], and to impede molecule diffusion through fluid interfaces by forming thick films [8, 9].

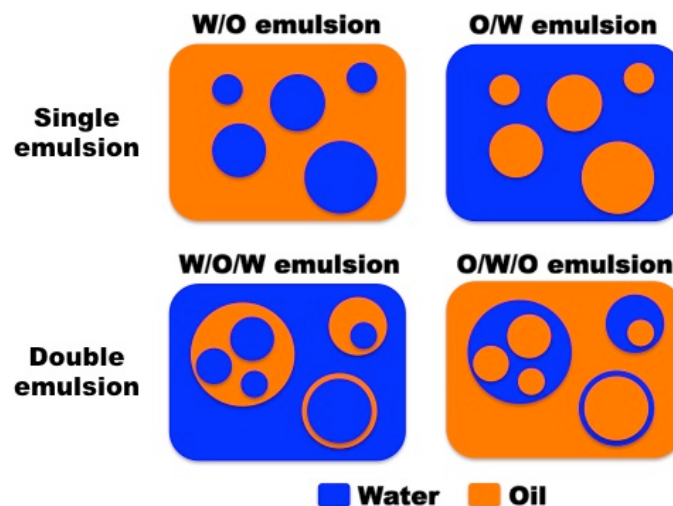


Figure 2.1 Schematic drawings of single emulsions and double emulsions.

Multiple emulsions have a wide range of applications in various fields as a means of encapsulation and controlled release of functional ingredients, for instance, in chemistry [10], pharmaceuticals [11-13], cosmetics [14-16], and food [17].

Droplets of multiple emulsions are also used as the template for the fabrication of new materials such as vesicles [18], nanoparticles [19] and microbeads [20-22]. In general, multiple emulsions can be formed by conventional bulk methods in stepwise mechanisms with the use of rotor-stator or high-pressure valve homogenizers [23]. For instance, to form w/o/w double emulsions, the first step is to prepare a primary w/o emulsion. Once the single emulsion is stable, another water phase is carefully added without rupturing the oil membranes. However, the double emulsion droplets that are produced using bulk methods are highly polydispersed due to the large size distribution of the oil droplets. In addition, the encapsulation efficiency is low as the second emulsification is a difficult procedure [24].

Since the properties and quality of multiple emulsions depend upon the size and the distribution of the droplets, alternative fabrication methods have been devised to generate uniform multiple emulsions [25, 26]. The membrane technique was developed to produce multiple emulsions by forcing a primary emulsion through microporous membranes in a continuous carrier phase flow [27-29]. Due to the geometric confinement, less shear force is required to conduct the second emulsification, compared with bulk methods. This reduces the rupturing of the droplets, and uniform double emulsions are thus obtained.

2.2 Droplet microfluidics for solvent emulsification

Droplet microfluidics is used to generate consistent multiple emulsions. The formation process can be completed either by a one-step or a multiple-step method, depending on the droplet forming devices. As shown in Figure 2.2A, for the two-step mechanism, the first and second emulsifications are carried out successively to shape the double emulsions *via* serially connected T-shaped junctions [30]. In other layouts, as shown in Figure 2.2 B&C, the double emulsion is formed in a one-step or two-step

using microcapillary devices with parallel flow streams [31]. Despite the diversity of the fabrication mechanisms, a high monodispersity of the attained multiple emulsion droplets can be achieved, as each dispersed phase droplet is formed individually in the same situation. In addition, the morphology and production rate of multiple emulsions are controlled by the incorporation of channel geometry and inflow parameters.

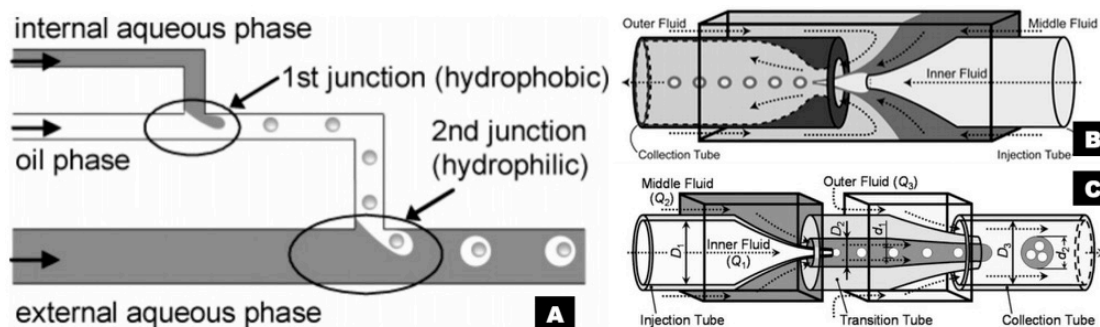


Figure 2.2 Schematic drawings of double emulsion formations via diverse layouts of microfluidic channels. A. Double emulsion droplets are formed in two-step method via serially connected double T-shaped junctions [30]. **B.** Double emulsion droplets are formed in one-step method via counter flow capillary devices. **C.** Double emulsion droplet are formed in two-step method via serially connect capillary devices [31].

Several types of droplet forming junctions can be used in droplet microfluidics.

The flow focusing device (MFFD), first proposed by Anna, exhibits excellent abilities in terms of controlling droplet size and increasing the productivity [32-34]. Depending on the channel dimension, the diameter of droplets/bubbles can be tuned from hundreds of nanometers to several millimeters [35, 36] and the yield rate can reach 670k per second [37]. This advantage makes the MFFD a powerful emulsification tool, [38, 39] which is now utilized in many major chemical and biological studies of droplet technologies [40-42].

In a comprehensive multiphase microfluidic system, an ideal MFFD is expected to achieve highly replicated droplet formation with a wide range of droplet diameters at required frequencies [43]. However, in reality, the dynamic droplet breakup is constrained by many factors such as microchannel material [44, 45], input flow rate [46], fluid viscosity [47], and interfacial tension [48]. The control of droplet

breakup is always necessary and two types of methods have been documented. The first method is an active one, which interferes with the droplet breakup process by introducing additional energy from mechanical [49, 50], thermal [51, 52], or electrical [53-55] sources. These approaches have been enabled by rapid development of microelectromechanical systems and novel manufacturing technologies in recent years [56, 57]. The second method is passive and uses a fixed configuration microchannel to influence droplet dispersion by (i) guiding the fluid delivery (ii) shaping the flow pattern, and (iii) focusing or dissipating the hydrodynamic forces. Previous studies indicate that the architectures of flow focusing junctions [58] and their dimensional parameters [59] determine the attained droplet size and yield frequency. In addition, several flow focusing junctions can be formed within an integrated droplet maker to generate multiple emulsions with certain morphologies [60-62].

In the study reported here, a geometric variant is proposed and demonstrated. This flow focusing junction, also known as the bat-wing junction, combines several individual design features (Figure 2.3a). In this junction, fluid delivery is guided by spatial constraints, and the droplet formation has been tested using laboratory experiments and 3D computational fluid dynamics simulations. It was found that the location of the dispersed phase breakup point and the attained droplet size are regulated by the continuous phase input parameters. This junction was further tested for solvent emulsification, in a stepwise mechanism using other additional droplet-forming junctions. Consistent water/polymer/oil double emulsions are produced using a passive satellite droplet removal approach. Monodispersed, core-shell shaped, polymeric capsules, with controllable morphologies, are obtained using a rapid on-chip photopolymerization.

2.3 The experiment

2.3.1 Chemicals and materials

Trimethylolpropane triacrylate (TMPTA, 246808), photoinitiator 2-hydroxy-2-methylpropiophenone (405655), glycerol (G5516), mineral oil (M8410), oil red O (O9755), thymol blue (32728), and potassium carbonate (P1472) were purchased from the Sigma-Aldrich Corporation. The optical polymer, norland optical adhesive 61 (NOA 61), was purchased from Tech Optics Ltd.

2.3.2 Microfluidic chip manufacture

The 2D configurations of the microfluidic circuit was devised using SolidWorks CAD software, and the files were saved as “.dxf” format files. These files were exported to the computer-aided manufacturing software (CircuitCAM) to contour the milling routing and to optimize the tool-path for the CNC machine (LPKF, C30), for which files were compiled as “.job” format files. The “.job” files were opened using BoardMaster control software, which in turn was used to process the plotting data and directly control the milling process. The circular polymer disks were attached to the board of the milling machine, and the tools were assigned manually to the milling head. Before milling the circuit configuration, the whole area of the polymer disk was milled twice to produce a plain top surface, in order to obtain uniform channel depth. Thereafter, the microfluidic channels were milled layer by layer on the disk using the depth control. In order to avoid breaking the tool, each milled depth did not exceed 10% of the milled tool diameter. For PTFE disks, the rotating speed of the milling tools was set to 30,000 rpm, and the linear movement velocity of the pen head was set up to 8mm per second to achieve a surface roughness of $\sim 2\mu\text{m}$ as measured with a VEECO NT3300 white-light interferometer. To

manufacture a microfluidic circuit with a variety of channel depths, the milling process was begun with the deepest channel and finished with the shallowest one, so that clean structures were obtained. The last layer was milled twice without changing the depth in order to attain a smooth bottom surface. All channels were purposefully milled 100 microns deeper than those specified in the design. Surface polishing was then carried out manually with the SiC grinding papers (BUEHLER, Grit P320, P800, P1200 to P2500) in order to produce a smooth, plain top surface, and to remove the redundant polymer layer. (Channel depths were measured with a Nikon QUADRA-CHEK 200 microscope accessory.) This process is necessary for preventing fluid leakage from the microfluidic circuits, as any scratch deeper than 6 microns will split the flow. Any PTFE residue remaining in the channel was removed carefully with a toothbrush. Finally, the chip was cleaned with acetone three times and dried overnight, in a vacuum oven at 50 degrees Celsius.

2.3.3 Microfluidic device setup

A 10mm-thick ground glass disc coated with a 100 μm -thick perfluoroalkoxy (Goodfellows, UK) film was placed over the PTFE disc so as to provide both (i) a continuous duct geometry with a water contact angle of $\sim 108^\circ$, and (ii) a robust viewing window when mechanically compressed within a stainless steel integration and fluidic interface manifold. FEP tubing was used for the fluid delivery, whereby the tubes were inserted into the holes from the back of the microfluidic chip. The connection part was sealed with rubber O-rings and M6 flangeless nuts (SUPELCO 55064). The other end was connected with the PEEK female to female Luers (SUPELCO 55076), and connected using SGE 10 ml gas-tight glass syringes. All the inlet tubing had a length of 30cm with a 0.8mm inner diameter and a 1.5 mm outer diameter. The dimension of the outlet FEP tubing, was determined by the size of the

outputted droplets. Two kinds of tube were used in this project, which are (1) a 3.2mm outer diameter and 1.50mm inner diameter tube; and, (2) a 1.58mm outer diameter and 0.8mm inner diameter tube. A hollow metal cylinder was used to level up the whole apparatus. Syringe displacement pumps (KD Scientific model 789200L) were used to deliver fluids into the microfluidic chip. The system was cleaned by pumping acetone, and dried with continuous airflow before the experiment.

2.3.4 Experiment and measurement

In this experiment water/polymer/oil (W/P/O) was used as the template of double emulsion droplets, and was formed by a two-step emulsification method on the PTFE microfluidic chip without any surface treatment. The morphology of the double emulsion was controlled by adjusting the input flow rates without adding any surfactant (due to the high surface energy of hydrophobic PTFE walls). The precursor was cured using a UV light source (5W 365nm-wavelength UV LED) whilst the droplets were flowing through the PTFE outlet tubing. The attained solid microcapsules were collected in a beaker, which was prefilled with the continuous phase. Real-time video clips of the droplet formation regime were generated using a high-speed camera (Mega-speed) mounted on a Nikon AZ100 microscope. Dimensional images of solid capsules were taken using a Nikon MM-800 measuring microscope, and analyzed using Nikon NIS-elements D 3.2 software.

2.3.5 Computational fluid dynamic simulation

Time-transient 3D computational fluid dynamics simulations were developed to study the droplet formation regimes of the bat-wing junction using COMSOL Multiphysics 4.4 software (COMSOL Inc., Burlington, MA). The models were defined as follows: The geometry of the bat-wing junction was extruded using a 3D model with a rectangular cross section (height = 600 microns). The dispersed phase

injects through the middle channel, and the continuous phase entered from the sides. The “Laminar Two-Phase Flow, Level Set (tpf)”, included in the COMSOL microfluidic module, was utilized for droplet breakup. The level set variables are described in a momentum transport equation, a continuity equation, and a level set equation. (These are not discussed in this thesis, but can be found in the related literatures.) [63]. For the setting of boundary conditions, laminar inflow conditions were applied to all three inlets. Pressure with no viscous stress condition was the outlet boundary condition. Wetted wall conditions were assumed for all duct surfaces with a 108° contact angle. The slip length was set as at half the value of the mesh size parameter. Other parameters are showed in Table 2.1. The mesh quality was selected as a “finer” resolution, which creates 522922 degrees of freedom in the geometry. To optimize the performance and accuracy of the simulations, the solver sequence was modified manually *via* the instructions obtained from the COMSOL. One simulation normally lasted 7~8 hours. The isosurface, volume arrow, velocity magnitude, and pressure distribution were plotted on geometric median surfaces to demonstrate the droplet breakup process. Numerical data was obtained for further analysis of the flow profile.

Table 1. Parameters of the droplet breakup models in COMSOL Multiphysics

<i>Parameters</i>	<i>Value</i>
<i>Times</i>	$5 [s]$
<i>Reinitialization parameter</i>	$\gamma = 0.15 [m/s]$
<i>Parameter controlling interface thickness</i>	$l_s = tpf.hmax/2 [m]$
<i>Temperature</i>	$T = 293.15 [K]$
<i>Contact Angle</i>	$\theta_\omega = 5 * \pi / 6 [rad]$
<i>Dispersed phase flow rate</i>	$2.00 [ml/hr]$

2.4 Result and discussion

2.4.1 Cross-shaped flow focusing junction

Conventional cross-shaped flow focusing junctions show the ability to form monodispersed single emulsion droplets in the dripping regime. In planar microfluidic devices, flow focusing junctions are sequentially connected and used to generate multiple emulsions droplets through a stepwise emulsification mechanism. However, compared to the one-step method to form such droplets, where only one dripping instability (dispersed phase break-up) exists during the droplet formation, the two-step method has two dripping instabilities, that can lead to output inconsistencies. In my previous work before this PhD, I found that it is difficult to produce monodispersed water/TMPTA/mineral oil double emulsion droplets on PTFE microfluidic chips, using two sequentially connected cross-shaped flow focusing junctions. The input flow rates of the three phases are limited in a narrow range in order to operate each junction in its dripping regime for the monodispersed droplet formation. As the location of the droplet breakup point is fixed in the cross-shaped flow-focusing junction in the dripping regime, the double emulsion droplets are always difficult to obtain with defined volume ratios between the inner phase and the middle phase. Also, previous literature points out that the two-step method has less control on the double emulsion morphologies than the one-step method, in terms of forming a thin layer of middle phase around the encapsulated droplet. These issues gave rise to the idea of devising a new type flow-focusing fluidic junction, which had the means to regulate the droplet breakup location, and finely tune the size of the dispersed phase. By changing the continuous phase input flow rates, to form consistent double

emulsion droplets, this was subsequently shown to be achievable by the bat-wing junction, especially for droplets with highly compartmentalized internal structures using the two-step method.

2.4.2 Description of bat-wing junction geometry

The complication of the MFFD geometry increases the influence of spatial constraints on the droplet formation [64]. The bat-wing junction was designed to comprise two cross-shape intersections, aligned end-to-end, and sharing the side inlets with bifurcations as shown in Figure 2.3a. The two intersections were linked by an expansion zone and end with an expansion outlet. These width-expanding structures are utilized to focus and dissipate the flows, and create local maximum velocity magnitude points where the highest shear force was incurred [65]. The upstream and downstream bifurcations couple the pressures of the two intersections and form a uniform pressure gradient in the expanding zone (Figure 2.3b). The widths of the bifurcations are narrower than the middle channel so as to be easily obstructed by the middle flow, thus form stable, sequential and discrete droplets [66]. The staggered geometry serves as a fluid shunt and directs the fluid delivery either upwards or downwards according to the local dynamic pressure distribution.

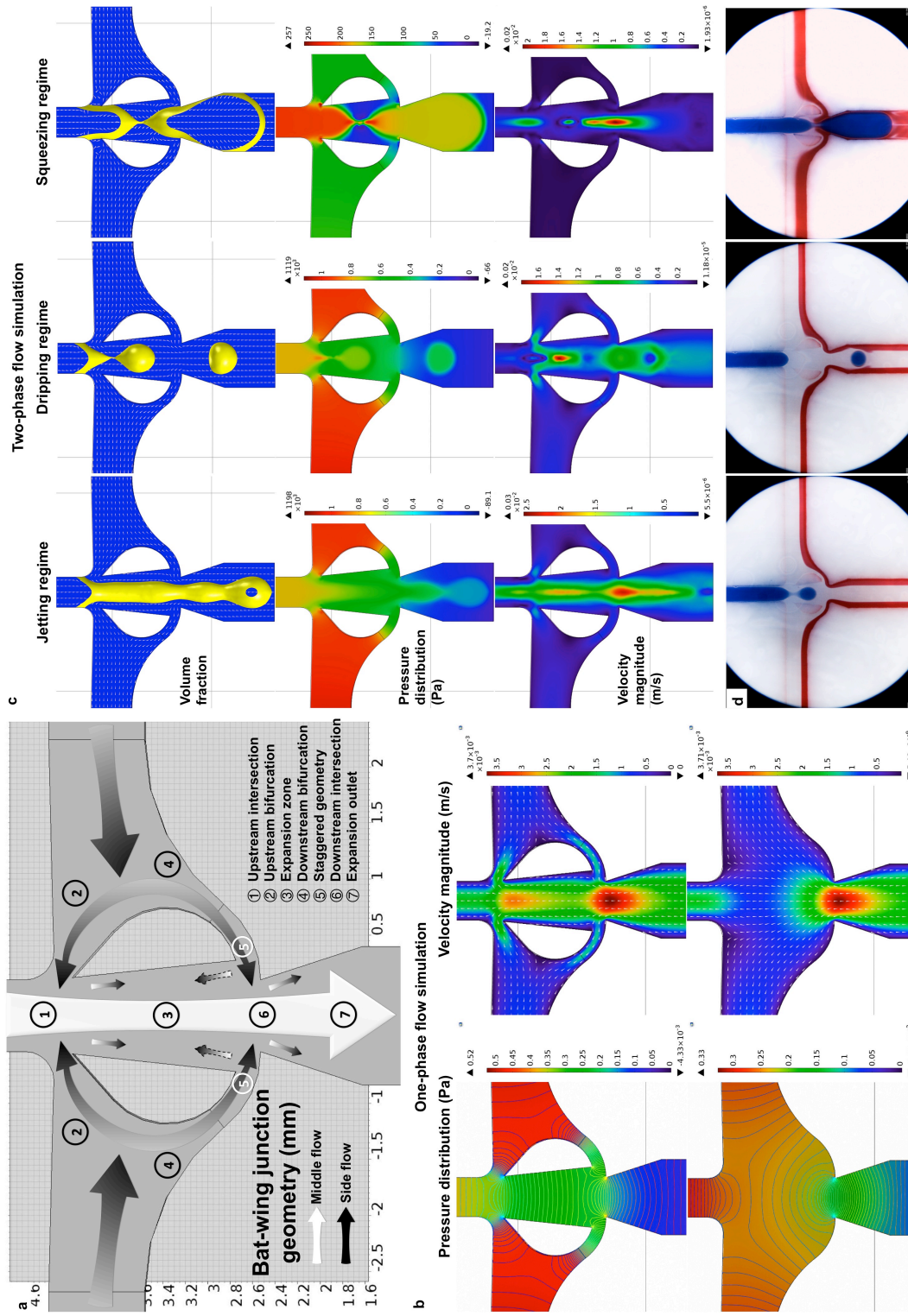


Figure 2.3 Bat-wing junction geometry and droplet formation regimes. **a**, Schematic drawing of the bat-wing junction geometry. The sizes of all the bat-wing junctions shown in this paper are as the one in this image. **b**, One-phase flow simulations with and without bifurcations when single phase fluid, flows from both the top and side inlets. The top inflow rate is 1 ml/hour and the right and left inflows are both 1.6 ml/hour. **c**, Two-phase simulations of water-in-oil droplet formation in jetting, dripping and squeezing regimes. The W/P input flow rates were 5/8, 2/8 and 2/0.96 ml/hour, respectively. In row a(i), the yellow films illustrate the boundary between water phase and oil phase. The blue vacancies in yellow illustrate the water phase touching the top channel wall. **d**, Experimental images of droplet formation in laminar oil phase (clear and red) in dripping regime (left and middle) and squeezing (right) regime with the blue/clear/red phases flow rate 2/32/8 and 2/0.28/0.28 ml/hour, respectively. All the emulsions are formed on the PTFE microfluidic chip.

2.4.3 Study of droplet formation in the bat-wing junction

Like other flow focusing junctions, different regimes [67, 68] of droplet formation are identified in the bat-wing junction (Figure 2.3c). Partly dyed, laminar continuous phase flow (formed using an additional upstream Y-junction) illustrates the dynamic flow pattern during the droplet breakup process. In the dripping regime, the droplet is pinched off at the upstream intersection. The downstream bifurcations provide extra pathways for continuous phase, in order to avoid droplet coalescence in

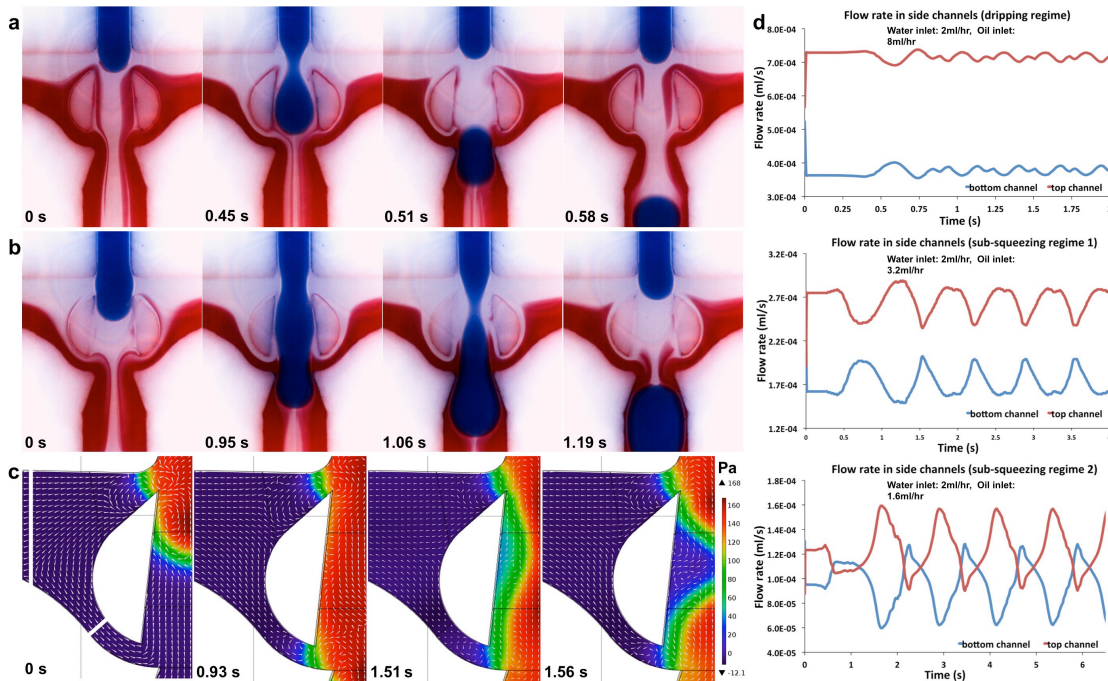


Figure 2.4 Continuous phase flow oscillation at bi-furcate geometry. a, Time sequence images of droplet formation in sub squeezing regime 1. Water (blue) phase blocks the upstream bifurcations and the oil phase (clear and red) flows to the downstream bifurcations. The blue/clear/red phases flow rate are 2/8/8 ml/hr. **b,** Time sequence images of droplet formation in sub squeezing regime 2. Dispersed phase blocks all the bifurcations and continuous phase flows into the expansion zone from two directions. The blue/clear/red phases flow rates are 2/2.4/2.4 ml/hr. **c,** Time sequence images of two-phase droplet breakup simulation in sub squeezing regime 2. The arrows show the local flow direction. Eddy flow appears where the blockage happening (the expansion zone and the bifurcations) and the size change by time. Colour gradient shows the pressure distribution. The top inlet is 1ml/hour and the side inlets are both 0.5ml/hour. **d,** Average continuous flow rates in the bifurcations in different droplet formation regimes. Numerical data was obtained from the CFD simulations result. The average flow rate at downstream bifurcation is measured at the cross section at the short white line shown in Figure 2.4c. The average continuous phase flow rate through the upstream bifurcation to the joint area was obtained by the total input (long white line) minus average bottom flow rate.

the width-expanding channel. The continuous phase was split at the bi-furcate structure and forms a double-layer sheath flow in the outlet channel (Figure 2.3d left and middle). Compared with other works, [69, 70] the MFFD provides a geometry-induced “shielding flow” to protect the droplet formation from contacting the outer layer fluid, where additives can be added to trigger any subsequent droplet processing operations, such as interfacial polymerization or lipid assembly [71-74].

In the squeezing regime, fluid flow is dominated by the viscous effects, and interfacial stress performs an important role in the droplet breakup [75]. With the bat-wing junction, the dispersed phase perturbs the continuous flow in the bifurcations, when in the squeezing regime. Eddy flows appear in pairs with the local pressure growth at the positions of the blockage. The continuous phase squeezes against the immiscible interfaces and slowly flows into the expansion zone. The flow direction and rate of continuous phase in the bifurcations change periodically, and are regulated by the dynamic pressure distribution, which is confined by the geometry during the droplet formation (Figure 2.4). Two sub-regimes are identified by the movement of the dispersed phase in the expansion zone (Figure 2.4a and Figure 2.4b). In the first

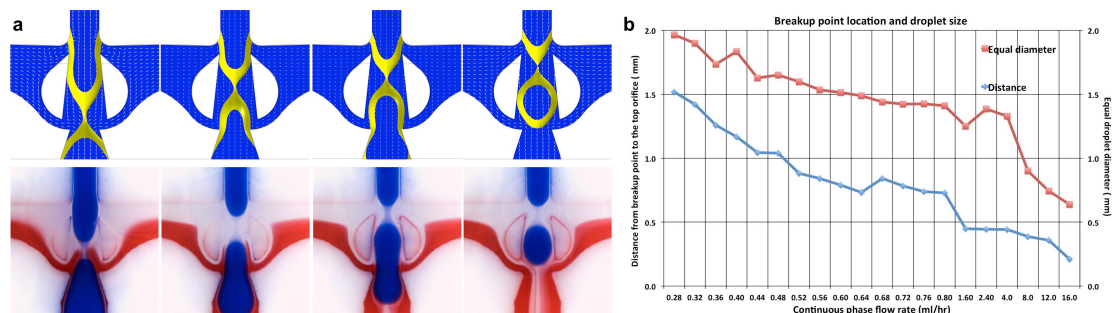


Figure 2.5 Control of droplet breakup location at bat-wing junction. **a**, coupled CFD simulations and laboratory experiments illustrate the different water droplet breakup location in oil at bat-wing junction. All dispersed phases input rate are 2ml/hr. The continuous phase flow rate, from left to right, are 0.28ml/hour, 0.52ml/hour, 0.64ml/hour and 1.60ml/hour, respectively. **b**, The relationship between the continuous phase flow rate with droplet breakup point and droplet size. When the continuous phase flow rate is increased, the droplet breakup location moves upward with droplet size reduction.

sub regime (single blockage), the dispersed phase only obstructs the upstream bifurcations. The droplet is formed at the upstream intersection, in the dripping regime. In the second sub regime (double blockages), the dispersed phase flows further downward and obstructs the downstream bifurcations. The accumulated continuous phase in the expanding zone (injected from both the bifurcations) squeezes the dispersed phase into an hourglass form, which is stabilized by the channel walls, and eventually caused to break off. It is found that the location point of droplet breakup, as well as the attained droplet size, is related to the continuous phase flow rate. As shown as Figure 2.5, when the continuous phase flow rate is increased, the droplet break-off point moves upwards to the upstream intersection and the droplet size is reduced. This is due to that under different input situations, the volumes of the continuous phase from the upstream bifurcations and from the downstream bifurcations into the expansion zone are different, which in turn induces different pressure gradients during the droplet formation. Hence, the meeting point of the opposite flows is adjustable by changing the continuous phase input rates so that the shear force is applied to the dispersed phase stream at various locations.

2.4.4 Study of double emulsion droplets formation in the bat-wing junction

In further experiments, core-shell shaped W/P/O double emulsions droplets were formed by a stepwise emulsification method in serially connected droplet forming junctions (Figure 2.6a). The W/P emulsion was prepared at the first droplet forming junction with the desired volume ratio and droplet assignment in carrier phase. The bat-wing junction was employed as the second droplet forming junction to shear off the emulsion at the required break-off point to repeatedly obtain certain length W/P segments. Also, no satellite polymer droplets were obtained in the final

product while the shear off point location is controlled in the expansion zone. (Satellite droplets are common by-products in droplet formation, due to Rayleigh breakup and considerable effort is required for their separation from the primary droplets in most scenarios [76].) This is due to that after droplet break-off, the eddy flows in the expansion zone always acts in a countercurrent manner to the direction of flow in the middle channel, causing the satellite droplets to retain a stationary position within the joint area, to be eventually merged with the next packet of incoming dispersed phase (Figure 2.6b). These attributes are necessary to generate consistent double emulsions and reduce the volume variation of the attained segments when using stepwise emulsification methods. Once formed, the double emulsion is stabilized in the MFFD due to the high surface energy of the hydrophobic PTFE substrate. After the segments assume a spherical form with minimal surface area to volume ratio in the outlet tubing, the polymeric phase is photo-cured by ultraviolet irradiation, thus forming the solid polymeric matrix, which incorporates the internal aqueous water compartments.

Firstly, we presented the production of single core polymeric capsules in a T-junction/bat-wing junction microfluidic device by a two-step method. Different W/P volume ratios were prepared at the T-junction and their correlated oil phase flow rates at the bat-wing junction are shown in Figure 2.6c. The production frequency of W/P segments reaches up to 20Hz by changing the inflow parameters while the W/P flow rate ratio was set at a constant value (Figure 2.6d). When the W/P/O input parameters are 0.4ml/hour, 0.2ml/hour and 1.2ml/hour, the average size of solid capsules was $\varnothing 892.5\mu\text{m} \pm 7.52\mu\text{m}$ with a $65.2\mu\text{m} \pm 4.42\mu\text{m}$ shell thickness. (Data was obtained from a random picked sample, which contains 50 solid capsules).

Secondly, asymmetric dual-core double emulsions were produced with a hybrid stepwise method. Water droplets were dispersed into the polymer phase as the first procedure of the two-step method and then the W/P emulsion was broken up at the bat-wing junction as one-step method, which according to previous work [77] is only available in jetting regime of a common geometry MFFD. This phenomenon also contributed to the control of droplet breakup point by the continuous phase flow rate. For instance when the W/P input rates are both 0.2ml/hour, single core segments are

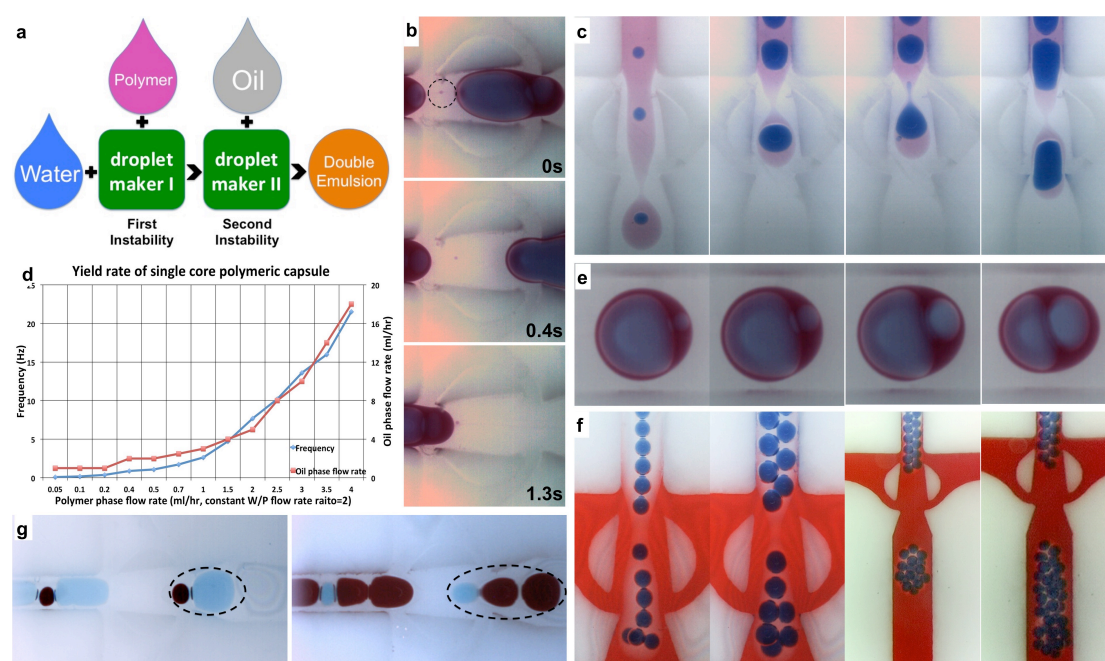


Figure 2.6 Multiple emulsions preparations at bat-wing junction. **a**, Schematic drawing of water/polymer/oil double emulsion formation in a stepwise mechanisms. **b**, Passive satellite droplet extinction. The time sequence images are showing the formation of satellite droplet, the stationary position of satellite droplet, and the coalescence of satellite droplet with incoming dispersed phase, respectively. **c**, Different volume ratios of W/P emulsion, from left to right, 0.03, 1, 1 and 2.33, respectively. The difference of the second and third images is the oil phase input flow rates, which are 1.8ml/hour and 2.2 ml/hour. The emulsion shear-off point is changed, and a secondary water droplet is produced and allocated in the following polymer segment. **d**, Single core water/TMPTA segment production frequency. Each point was measured from 30 sequenced produced segments recorded by high-speed camera. The average error is 0.78%. **e**, Size control of the asymmetric water cores. The water and the polymer phase flow rates are 0.25 ml/hour and 0.12 ml/hour for all the images and the oil phase flow rates are 1.24, 1.38, 1.65 and 1.80 ml/hour, respectively. **f**, Multicore double emulsion formation. From left to right, the core number is 7 (W/P volume ratio=0.5), 7 (W/P volume ratio=1.5), 15 and 30, respectively. **g**, Various size water droplets with different dyes encapsulated in the polymer segments.

generated at the oil phase flow rate from 1.2ml/hour to 2.1ml/hr. If the oil input flow rate is increased to 2.2ml/hour, the water droplet is broken into two droplets and assigned to the adjacent polymer segments respectively (Figure 2.6c). The division is highly repeatable and the volume ratio between the two water droplets is also regulated by the continuous phase flow rate (Figure 2.6e). When the W/P/O input parameters are 0.3ml/hour, 0.6ml/hour and 2.4ml/hour, the average size of attained segments is $\varnothing 935\mu\text{m} \pm 10\mu\text{m}$ with an original water droplets $\varnothing 748\mu\text{m} \pm 9.5\mu\text{m}$ before shear-off, and a secondary droplet $\varnothing 301\mu\text{m} \pm 23.1\mu\text{m}$ after dispersion (data were obtained from 50 segments, which were sequentially generated).

Multicore polymeric capsules were fabricated with various core numbers in a cross-junction/bat-wing junction microfluidic device. To load more cores in one polymer segment, optimal input parameters need to be identified to produce small water droplets with a compact assignment at high W/P input flow rate ratio. The volume of the capsule was determined at the bat-wing junction and the core number increased while the continuous phase flow rate was decreased. This provided the principle control feature. In the experiments, up to 30 cores were precisely loaded in one polymer segment (with only an occasional ~ 1 in 30 wrong assignment) at 0.1ml/hour, 0.2ml/hour and 0.6ml/hour input flow rate for water, polymer and oil phase, respectively (Figure 2.6f). Repeatable geometric organizations of cores, within a solid capsule, were evident and which depended upon their number (Figure 2.7a-q). In addition, multiple emulsions with various core sizes, reagents and assignments were produced in the MFFD. The W/P emulsion was prepared at the first droplet forming junction, using additional inlets channels. The bat-wing junction was used to shear off the dispersed phases precisely to attain discrete segments with constant size

(Figure 2.6g). Later work focused on the production of solid microcapsules (Figure 2.7r-t) with diversified morphologies from designed multiple emulsions.

2.4.5 Further discussion

The bat-wing junction demonstrated in this work exhibits the art of using fixed channel geometry to manipulate droplet breakup in planar microfluidics. By simply tuning the inflow parameters, the droplet shear-off location, the droplet morphology

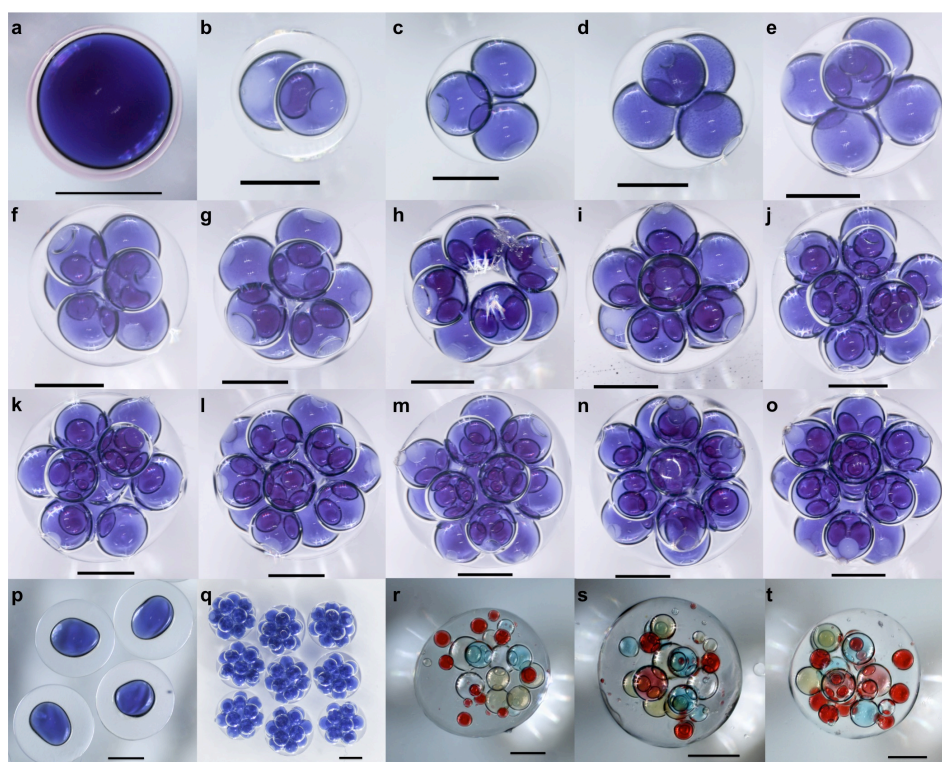


Figure 2.7 Solid polymeric capsules with various morphologies produced by our MFFD. All the scale bars indicate 500 microns. **a**, thin shell thickness, single core TMPTA capsule (water/polymer input ratio =3). **b-o**, Multicore NOA 61 capsules with controllable core number, produced by the same microfluidic system with the bat-wing junction. The water and polymer input rates are both 0.1ml/hr. The core numbers increase from 2 to 15 by changing oil phase flow rate gradually which are 4.5, 3, 2.4, 2, 1.8, 1.4, 1.3, 1.2, 1.1, 1.08, 1.02, 0.97, 0.48 and 0.31 (ml/hr), respectively. **r-t**, Polymeric capsules with multiple reagents water droplets inside.

and the production rate are finely regulated with a wide range of choices. In addition, the bat-wing junction has a built-in satellite droplet removal feature, which reduces the system instability and improves the production purity without any extra effort. In

multiphase emulsification process, the bat-wing junction tailors the incoming emulsion and forms monodispersed multiple emulsion droplets with desired volume. These characterizations increase the variety of productions from an individual microfluidic system and give more flexibility in experimental work.

Furthermore, the bat-wing junction geometry can be machined on microfluidic chips made from diverse substrates, and produce multiple emulsions from different templates in the same formation mechanism. For instance, on the PTFE microfluidic chips, water/ polymer/oil double emulsions have been well exploited to fabricate microcapsules with hardened polymeric shell, *via* the free radical polymerizations. The polymer phase can be replaced by the hydrogel solution, such as BSA or alginate solution, to produce soft microgels with tunable water content. On PMMA microfluidic chips, monodispersed water/oil/polymer double emulsion droplets can be generated and their morphologies can be controlled *via* the bat-wing junction. The related applications will be described in details in the later chapters.

2.5 Conclusion

In summary, it has been demonstrated that double emulsion droplets can be formed in a novel planar flow-focusing microfluidic junction with devised geometric constraints. The dynamic droplet breakup process inside this MFFD was investigated both in the experimental work and CFD simulations. The results indicate that by modifying the continuous phase flow rates, the droplet breakup point can be controlled as well as the droplet size. Furthermore, this MFFD has been utilized to generate consistent multiple emulsions and fabricate monodispersed micro-/millimeter size polymeric capsules with controllable morphologies (single core, dual asymmetric cores, multiple cores and multiple reagents) at controllable production

rate. The bat-wing junction is a facile, yet efficient tool for multiphase fluid emulsification in planar droplet microfluidics and shows the capability to be incorporated within microfluidic devices, to provide an on-demand, high throughput microfluidic system, for the precision fabrication of bespoke microdroplets and microcapsules. These might find many future applications such as in ICF target fabrication, stem cell encapsulation and protocell formation, which will be described later in this thesis.

References:

1. Kentish, S., Wooster, T. J., Ashokkumar, M., Balachandran, S., Mawson, R., and Simons, L., "The use of ultrasonics for nanoemulsion preparation," *Innovative Food Science & Emerging Technologies*, vol. 9, no. 2, pp. 170-175, 2008.
2. Khan, A. Y., Talegaonkar, S., Iqbal, Z., Farhan, J. A., and Roop, K. K., "Multiple emulsions: an overview," *Current Drug Delivery*, vol. 3, no. 4, pp. 429-443, 2006.
3. McClements, D. J., "Food emulsions: principles, practice, and techniques," *Boca Raton, Food hydrocolloids, CRC Press*, vol. 13, 419-424, 1999.
4. Tadros, T. F., *Emulsion Science and Technology: A general Introduction*, in *Emulsion Science and Technology*, T.F. Tadros, Editor. Wiley - VCH, pp. 1-56, 2009.
5. Binks, B. P., *Emulsions - Recent Advances In Understanding, In Modern Aspects Of Emulsion Science*, Binks, B. P. Editor. Royal Society of Chemistry, pp. 1-55, 1998.
6. Sela, Y., Magdassi, S., and Garti, N., "Polymeric surfactants based on polysiloxanes - graft-poly (oxyethylene) for stabilization of multiple emulsions," *Colloids and Surfaces A: Physicochemical and Engineering Aspects*, vol. 83, no. 2, pp. 143-150, 1994.
7. Michaut, F., Perrin, P., and Hébraud, P., "Interface composition of multiple emulsions: rheology as a probe," *Langmuir*, vol. 20, no. 20, pp. 8576-8581, 2004.
8. Michaut, F., Hebraud, P., and Perrin, P., "Amphiphilic polyelectrolyte for stabilization of multiple emulsions," *Polymer International*, vol. 52, no. 4, pp. 594-601, 2003.
9. Garti, N., and Lutz, R., *Recent Progress In Double Emulsions*, in *Emulsion: Structure Stability and Interactions*, Petsev, D. N. Editor, Elsevier, pp. 557-605, 2004.
10. Oh, C., Chung, S. C., Shin, S., Kim, Y. C., Im, S. S., and Oh, S. G., "Distribution of macropores in silica particles prepared by using multiple emulsions," *Journal of Colloid and Interface Science*, vol. 254, no. 1, pp. 79-86, 2002.
11. Fukushima, S., Nishida, A. M., and Nakano, M., "Preparation of and drug release from W/O/W type double emulsions containing anticancer agents using an oily lymphographic agent as an oil phase," *Chemical and Pharmaceutical Bulletin*, vol. 35, no. 8, pp. 3375-3381, 1987.

12. Ferreira, L. A. M., Seiller, M., Grossiord, J. L., Marty, J. P., and Wepierre, J., "Vehicle influence on *in vitro* release of metronidazole: role of w/o/w multiple emulsion," *International Journal of Pharmaceutics*, vol. 109, no. 3, pp. 251-259, 1994.
13. Khopade, A. J., and Jain, N. K., "Multiple emulsions containing rifampicin," *Die Pharmazie*, vol. 54, no. 12, pp. 915-919, 1999.
14. Vasudevan, T. V., and Naser, M. S., "Some aspects of stability of multiple emulsions in personal cleansing systems," *Journal of Colloid and Interface Science*, vol. 256, no. 1, pp. 208-215, 2002.
15. Yoshida, K., Sekine, T., Matsuzaki, F., Yanaki, T., and Yamaguchi, M., "Stability of vitamin A in oil-in-water-in-oil-type multiple emulsions," *Journal of the American Oil Chemists' Society*, vol. 76, no. 2, pp. 195-200, 1999.
16. Yanaki, T., "Preparation of O/W/O type multiple emulsions and its application to cosmetics," *Studies in Surface Science and Catalysis*, vol. 132, pp. 1009-1014, 2001.
17. Lobato-Calleros, C., Rodriguez, E., Sandoval-Castilla, O., Vernon-Carter, E. J., and Alvarez-Ramirez, J., "Reduced-fat white fresh cheese-like products obtained from W 1/O/W 2 multiple emulsions: viscoelastic and high-resolution image analyses," *Food Research International*, vol. 39, no. 6, pp. 678-685, 2006.
18. Lorenceau, E., Utada, A. S., Link, D. R., Cristobal, G., Joanicot, M., and Weitz, D. A., "Generation of polymerosomes from double-emulsions," *Langmuir*, vol. 21, no. 20, pp. 9183-9186, 2005.
19. Garcia-Fuentes, M., Torres, D., and Alonso, M. J., "Design of lipid nanoparticles for the oral delivery of hydrophilic macromolecules," *Colloids and Surfaces B: Biointerfaces*, vol. 27, no. 2, pp. 159-168, 2003.
20. Vladislavljević, G. T., and Williams, R. A., "Recent developments in manufacturing emulsions and particulate products using membranes," *Advances in Colloid and Interface Science*, vol. 113, no. 1, pp. 1-20, 2005.
21. Herrmann, J., and Bodmeier, R., "Somatostatin containing biodegradable microspheres prepared by a modified solvent evaporation method based on W/O/W-multiple emulsions," *International Journal of Pharmaceutics*, vol. 126, no. 1, pp. 129-138, 1995.
22. Kawakatsu, T., Trägårdh, G., and Trägårdh, C., "Production of W/O/W emulsions and S/O/W pectin microcapsules by microchannel emulsification," *Colloids and*

- Surfaces A: Physicochemical and Engineering Aspects*, vol. 189, no. 1, pp. 257-264, 2001.
23. Matsumoto, S., Kita, Y., and Yonezawa, D., "An attempt at preparing water-in-oil-in-water multiple-phase emulsions," *Journal of Colloid and Interface Science*, vol. 57, no. 2, pp. 353-361, 1976.
 24. Garti, N., "Double emulsions - scope, limitations and new achievements," *Colloids and Surfaces A: Physicochemical and Engineering Aspects*, vol. 123, pp. 233-246, 1997.
 25. Higashi, S., Shimizu, M., Nakashima, T., Iwata, K., Uchiyama, F., tateno, S., Tamura, S., and Setoguchi, T., "Arterial - injection chemotherapy for hepatocellular carcinoma using monodispersed poppy - seed oil microdroplets containing fine aqueous vesicles of epirubicin. Initial medical application of a membrane - emulsification technique," *Cancer*, vol. 75, no. 6, pp. 1245-1254, 1995.
 26. Sugiura, S., Nakajima, M., Yamamoto, K., Iwamoto, S., Oda, T., Satake, M., and Seki, M., "Preparation characteristics of water-in-oil-in-water multiple emulsions using microchannel emulsification," *Journal of Colloid and Interface Science*, vol. 270, no. 1, pp. 221-228, 2004.
 27. Mine, Y., Shimizu, M., and Nakashima, T., "Preparation and stabilization of simple and multiple emulsions using a microporous glass membrane," *Colloids and Surfaces B: Biointerfaces*, vol. 6, no. 4, pp. 261-268, 1996.
 28. Van der Graaf, S., Schroen, C., and Boom, R. M., "Preparation of double emulsions by membrane emulsification - a review," *Journal of Membrane Science*, vol. 251, no. 1, pp. 7-15, 2005.
 29. Vladislavljević, G. T., and Schubert, H., "Influence of process parameters on droplet size distribution in SPG membrane emulsification and stability of prepared emulsion droplets," *Journal of Membrane Science*, vol. 225, no. 1, pp. 15-23, 2003.
 30. Okushima, S., Nisisako, T., Torii, T., and Higuchi, T., "Controlled production of monodisperse double emulsions by two-step droplet breakup in microfluidic devices," *Langmuir*, vol. 20, no. 23, pp. 9905-9908, 2004.
 31. Utada, A. S., Lorenceau, E., Link, D. R., Kaplan, P. D., Stone, H. A., and Weitz, D. A., "Monodisperse double emulsions generated from a microcapillary device," *Science*, vol. 308, no. 5721, pp. 537-541, 2005.

32. Anna, S. L., Bontoux, N., and Stone, H. A., "Formation of dispersions using "flow focusing" in microchannels," *Applied Physics Letters*, vol. 82, no. 3, pp. 364-366, 2003.
33. The, S. Y., Lin, R., Hung, L. H., and Lee, A. P., "Droplet microfluidics," *Lab On A Chip*, vol. 8, no. 2, pp. 198-220, 2008.
34. Gu, H., Duits, M. H. G., and Mugele, F., "Droplets formation and merging in two-phase flow microfluidics," *International Journal of Molecular Sciences*, vol. 12, no. 4, pp. 2572-2597, 2011.
35. Kim, H., Luo, D., Link, D., Weitz, D. A., Marquez, M., and Cheng, Z. D., "Controlled production of emulsion drops using an electric field in a flow-focusing microfluidic device," *Applied Physics Letters*, vol. 91, no. 13, pp. 133106, 2007.
36. Li, Y., Yamane, D. G., Li, S., Biswas, S., Reddy, R. K., Goettert, J. S., Nandakumar, K., Kumar, C. S. S. R., "Geometric optimization of liquid-liquid slug flow in a flow-focusing millifluidic device for synthesis of nanomaterials," *Chemical Engineering Journal*, vol. 217, pp. 447-459, 2013.
37. Dhanaliwala, A. H., Chen, J. L., Wang, S., and Hossack, j. A., "Liquid flooded flow-focusing microfluidic device for in situ generation of monodisperse microbubbles," *Microfluidics and Nanofluidics*, vol. 14, no. 3-4, pp. 457-467, 2013.
38. Hashimoto, M., Garstecki, P., and Whitesides, G. M., "Synthesis of composite emulsions and complex foams with the use of microfluidic flow - focusing devices," *Small*, vol. 3, no. 10, pp. 1792-1802, 2007.
39. Shah, R. K., Shum, H. C., Rowat, A. C., "CL Y., JW Kim, A. Fernandez-Nieves, CJ Martinez and DA Weitz," *Mater, Today*, vol. 11, pp. 18-27, 2008.
40. Xu, Q., Hashimoto, M., Dang, T. T., Hoare, T., Kohane, D. S., Whitesides, G. M., Langer, R., and Anderson, D. G., "Preparation of monodisperse biodegradable polymer microparticles using a microfluidic flow - focusing device for controlled drug delivery," *Small*, vol. 5, no. 13, pp. 1575-1581, 2009.
41. Aikawa, T., Konno, T., Takai, M., and Ishihara, K., "Spherical phospholipid polymer hydrogels for cell encapsulation prepared with a flow-focusing microfluidic channel device," *Langmuir*, vol. 28, no. 4, pp. 2145-2150, 2011.
42. Gañán-Calvo, A. M., Montanero, J. M., Martín-Banderas, L., and Flores-Mosquera, M., "Building functional materials for health care and pharmacy from

- microfluidic principles and flow focusing,” *Advanced Drug Delivery Reviews*, vol. 65, no. 11, pp. 1447-1469, 2013.
43. Yobas, L., Martens, S., Ong, W. L., and Ranganathan, N., “High-performance flow-focusing geometry for spontaneous generation of monodispersed droplets,” *Lab On A Chip*, vol. 6, no. 8, pp. 1073-1079, 2006.
 44. Roberts, C. C., Rao, R. R., Loewenberg, M., and Brooks, C. F., Galambos, P., Grillet, A. M., and Nemer, M. B., “Comparison of monodisperse droplet generation in flow-focusing devices with hydrophilic and hydrophobic surfaces,” *Lab On A Chip*, vol. 12, no. 8, pp. 1540-1547, 2012.
 45. Seo, M., Paquet, C., Nie, Z., Xu, S. Q., and Kumacheva, E., “Microfluidic consecutive flow-focusing droplet generators,” *Soft Matter*, vol. 3, no. 8, pp. 986-992, 2007.
 46. Lee, W., Walker, L. M., and Anna, S. L., “Role of geometry and fluid properties in droplet and thread formation processes in planar flow focusing,” *Physics of Fluids (1994-present)*, vol. 21, no. 3, pp. 032103, 2009.
 47. Nie, Z., Seo, M. S., Xu, S. Q., Lewis, P. C., Mok, M., Kumacheva, E., Whitesides, G. M., Garstecki, P., and Stone, H. A., “Emulsification in a microfluidic flow-focusing device: effect of the viscosities of the liquids,” *Microfluidics and Nanofluidics*, vol. 5, no. 5, pp. 585-594, 2008.
 48. Peng, L., Yang, M., Guo, S. S., Liu, W., and Zhao, X. Z., “The effect of interfacial tension on droplet formation in flow-focusing microfluidic device,” *Biomedical Microdevices*, vol. 13, no. 3, pp. 559-564, 2011.
 49. Hsiung, S. K., Chen, C. T., and Lee, G. B., “Micro-droplet formation utilizing microfluidic flow focusing and controllable moving-wall chopping techniques,” *Journal of Micromechanics and Microengineering*, vol. 16, no. 11, pp. 2403, 2006.
 50. Abate, A. R., Romanowsky, M. B., Agresti, J. J., and Weitz, D. A., “Valve-based flow focusing for drop formation,” *Applied Physics Letters*, vol. 94, no. 2, pp. 023503, 2009.
 51. Tan, S. H., Murshed, S. M. S., Nguyen, N. T., Wong, T. N., and Yobas, L., “Thermally controlled droplet formation in flow focusing geometry: formation regimes and effect of nanoparticle suspension,” *Journal of Physics D: Applied Physics*, vol. 41, no. 16, pp. 165501, 2008.

52. Stan, C. A., Tang, S. K. Y., and Whitesides, G. M., "Independent control of drop size and velocity in microfluidic flow-focusing generators using variable temperature and flow rate," *Analytical Chemistry*, vol. 81, no. 6, pp. 2399-2402, 2009.
53. Malloggi, F., Vanapalli, S. A., Gu, H., Ende, D. V. D., and Mugele, F., "Electrowetting-controlled droplet generation in a microfluidic flow-focusing device," *Journal of Physics: Condensed Matter*, vol. 19, no. 46, pp. 462101, 2007.
54. He, P., Kim, H., Luo, D., Marquez, M., and Cheng, Z. D., "Low-frequency ac electro-flow-focusing microfluidic emulsification," *Applied Physics Letters*, vol. 96, no. 17, pp. 174103, 2010.
55. Tan, S. H., Semin, B., and Baret, J. C., "Microfluidic flow-focusing in ac electric fields," *Lab On A Chip*, vol. 14, no. 6, pp. 1099-1106, 2014.
56. Khosla, A., and Hesketh, P. J., "Microfluidics, MEMS/NEMS, Sensors and Devices," *Journal of The Electrochemical Society*, vol. 161, no. 2, pp. Y1-Y1, 2014.
57. Ashraf, M. W., Tayyaba, S., and Afzulpurkar, N., "Micro electromechanical systems (MEMS) based microfluidic devices for biomedical applications," *International Journal of Molecular Sciences*, vol. 12, no. 6, pp. 3648-3704, 2011.
58. Ong, W. L., Hua, J., Zhang, B., Teo, T. Y., Zhuo, J., Nguyen, N. T., Ranganathan, N., Yobas, L., "Experimental and computational analysis of droplet formation in a high-performance flow-focusing geometry," *Sensors and Actuators A: Physical*, vol. 138, no. 1, pp. 203-212, 2007.
59. Gupta, A., Matharoo, H. S., Makkar, D., and Kumar, R., "Droplet formation via squeezing mechanism in a microfluidic flow-focusing device," *Computers & Fluids*, vol. 100, pp. 218-226, 2014.
60. Hashimoto, M., Shevkoplyas, S. S., Zasońska, B., Szymborski, T., Garstecki, P., and Whitesides, G. M., "Formation of bubbles and droplets in parallel, coupled flow - focusing geometries," *Small*, vol. 4, no. 10, pp. 1795-1805, 2008.
61. Liu, K., Ding, H., Chen, Y., and Zhao, X. Z., "Droplet-based synthetic method using microflow focusing and droplet fusion," *Microfluidics and Nanofluidics*, vol. 3, no. 2, pp. 239-243, 2007.
62. Mulligan, M. K., and Rothstein, J. P., "Scale-up and control of droplet production in coupled microfluidic flow-focusing geometries," *Microfluidics and Nanofluidics*, vol. 13, no. 1, pp. 65-73, 2012.

63. Van der Graaf, S., Nisisako, T., Schroen, C., Sman, R. G. M., and Boom, R. M., "Lattice Boltzmann simulations of droplet formation in a T-shaped microchannel," *Langmuir*, vol. 22, no. 9, pp. 4144-4152, 2006.
64. Tan, Y. C., Fisher, J. S., Lee, A. I., Cristini, V., and Lee, A. P., "Design of microfluidic channel geometries for the control of droplet volume, chemical concentration, and sorting," *Lab On A Chip*, vol. 4, no. 4, pp. 292-298, 2004.
65. Tan, Y. C., Cristini, V., and Lee, A. P., "Monodispersed microfluidic droplet generation by shear focusing microfluidic device," *Sensors and Actuators B: Chemical*, vol. 114, no. 1, pp. 350-356, 2006.
66. Abate, A. R., and Weitz, D. A., "High-order multiple emulsions formed in poly (dimethylsiloxane) microfluidics," *Small*, vol. 5, no. 18, pp. 2030-2032, 2009.
67. Sullivan, M. T., and Stone, H. A., "The role of feedback in microfluidic flow-focusing devices," *Philosophical Transactions of the Royal Society of London A: Mathematical, Physical and Engineering Sciences*, vol. 366, no. 1873, pp. 2131-2143, 2008.
68. Anna, S. L., and Mayer, H. C., "Microscale tipstreaming in a microfluidic flow focusing device," *Physics of Fluids (1994-present)*, vol. 18, no. 12, pp. 1215-1218, 2006.
69. Si, T., Feng, H. X., Luo, X. S., and Xu, R. X., "Formation of steady compound cone-jet modes and multilayered droplets in a tri-axial capillary flow focusing device," *Microfluidics and Nanofluidics*, vol. 18, no. 5-6, pp. 967-977, 2014.
70. Workman, V. L., Dunnett, S. B., Kille, P., and Palmer, D. D., "On-chip alginate microencapsulation of functional cells," *Macromolecular Rapid Communications*, vol. 29, no. 2, pp. 165-170, 2008.
71. Quevedo, E., Steinbacher, J., and McQuade, D. T., "Interfacial polymerization within a simplified microfluidic device: capturing capsules," *Journal of the American Chemical Society*, vol. 127, no. 30, pp. 10498-10499, 2005.
72. Song, H., Chen, D. L., and Ismagilov, R. F., "Reactions in droplets in microfluidic channels," *Angewandte Chemie International Edition*, vol. 45, no. 44, pp. 7336-7356, 2006.
73. Matosevic, S., and Paegel, B. M., "Stepwise synthesis of giant unilamellar vesicles on a microfluidic assembly line," *Journal of the American Chemical Society*, vol. 133, no. 9, pp. 2798-2800, 2011.

74. Valencia, P. M., Basto, P. A., Zhang, L. F., Rhee, M., Langer, R., Farokhzad, O. C., and Karnik, R., "Single-step assembly of homogenous lipid - polymeric and lipid - quantum dot nanoparticles enabled by microfluidic rapid mixing," *ACS Nano*, vol. 4, no. 3, pp. 1671-1679, 2010.
75. Garstecki, P., Gitlin, I., DiLuzio, W., Whitesides, G. M., Kumacheva, E., and Stone, H. A., "Formation of monodisperse bubbles in a microfluidic flow-focusing device," *Applied Physics Letters*, vol. 85, no. 13, pp. 2649-2651, 2004.
76. Tan, Y. C., and Lee, A. P., "Microfluidic separation of satellite droplets as the basis of a monodispersed micron and submicron emulsification system," *Lab On A Chip*, vol. 5, no. 10, pp. 1178-1183, 2005.
77. Abate, A. R., Thiele, J., and Weitz, D. A., "One-step formation of multiple emulsions in microfluidics," *Lab On A Chip*, vol. 11, no. 2, pp 253-258, 2011.

CHAPTER III.

Mass Production of Polymeric Microcapsules for Inertial Confinement Fusion Target Fabrication *via* Planar Droplet Microfluidics

3.1 A brief overview of controllable nuclear fusion

Nuclear fusion, the fundamental reaction of which is shown in Figure 3.1, is an alternative energy source that may help satisfy the increasing global demand for energy consumption. In comparison with traditional combustion energies, fusion energy has several significant advantages: it is relatively clean, potentially produces a vast energy output, whilst generating limited waste (including radioactive waste) [1-6]. However, this energy resource is still not exploited today due to the fact that a fusion reaction is extremely difficult to maintain and control beyond a fractional moment, compared with nuclear fission reactions. One of the challenges in developing controllable fusion is the need to confine the hot deuterium and tritium plasma, which in turn is essential for collision of the atomic nuclei to occur and to generate energy.

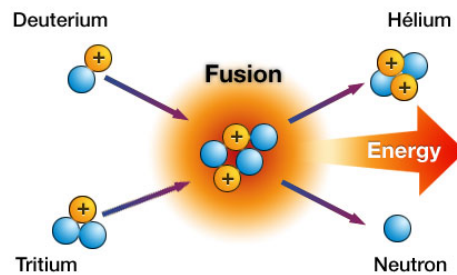


Figure 3.1 Schematic drawing of the nuclear fusion of a deuterium molecule and a tritium molecule. The fusion creates a helium molecule, a free neutron, and releases 17.59 MeV energy. The temperature of the Sun's core where the fusion reaction takes place is 15,000,000C, whereas on Earth the temperature in a fusion reactor needs to reach 150,000,000C [1].

3.1.1 Magnetic confinement fusion

Extensive research has been conducted into developing methods for controlling the fusion reaction. To date, the most reachable method is magnetic confinement fusion (MCF), whereby magnetic fields are used to confine and heat the deuterium and tritium plasma. Based on this concept, the Tokamak device was developed to stabilize the plasma in a torus-shaped furnace, wherein high magnetic fields, whose field lines moving in a helical fashion, are applied (Figure 3.2A). The advantage of this method is the total confinement of the fuel plasma, although energy density is low whilst the fuel is being heated. The world's first Tokamak device, called "T-1 Tokamak", was built at the Kurchatov Institute in Moscow in 1950 [7]. In another MCF milestone, the Joint European Torus (JET) (Figure 3.2B) was built in Culham in the UK, and was the first Tokamak device to achieve controllable fusion energy release (~70% input energy) [8]. The latest one, the International Thermonuclear Experimental Reactor (ITER), is under construction near the Cadarache facility in the south of France, and is expected to generate 500MW fusion power from 50MW input power as a prototype of a future MCF power plant [9].

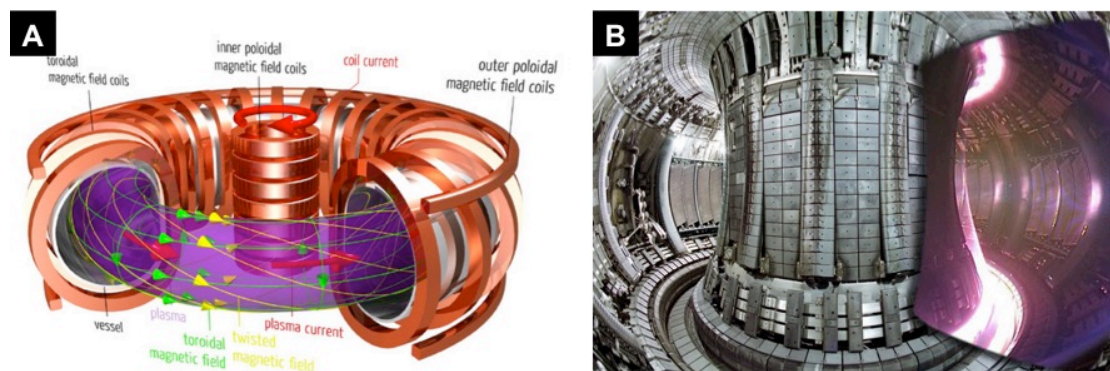


Figure 3.2 Magnetic confinement fusion. **A.** Schematic drawing of a Tokamak device and the principle of plasma confinement with magnetic fields. **B.** Photographs of JET's internal structure. The attached image on the right shows its working condition, and the bright zone indicates where the fuel plasma has a lower temperature.

3.1.2 Magnetized target fusion

Another approach, magnetized target fusion (MTF), uses a magnetic field to confine the plasma for controllable fusion energy [10]. The principle of MTF is to mechanically compress the magnetized fuel plasma by an imploding conductive shell, through heating the plasma to fusion conditions. LINUS, the first full MTF-based power plant was proposed at the Naval Research Laboratory in the US in the 1970s. However, back then it was impossible to build such a plant due to technical reasons. More recently, a Canadian company called General Fusion invented the spherical MTF reactors (Figure 3.3). During its operation, the reactor is filled with a molten lead-lithium vortex driven by an external pumping system. On each pulse of the reactor, magnetized plasma is injected into the centre of the plasma vortex. Around the reactor, an array of pistons impact and drive a pressure wave into the centre, which compresses the plasma towards the right conditions for fusion to occur.

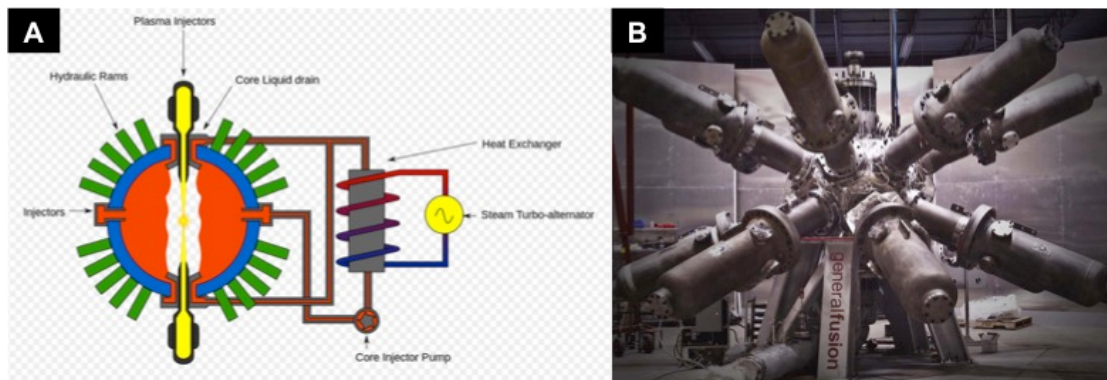


Figure 3.3 Magnetized target fusion. A. Schematic drawing of a magnetized target fusion reactor. B. Photograph of a MTF reactor developed by General Fusion. (Images source: <http://www.generalfusion.com/>)

3.1.3 Inertial confinement fusion

An alternative plasma confinement method for controllable fusion energy is called inertial confinement fusion (ICF) (Figure 3.4) [11, 12]. In a directive drive ICF, iced deuterium and tritium are sealed in a millimeter-sized fuel cell with an ablation

layer. The cell, the ICF target, is sent to the center of the reactor [13, 14]. Meanwhile, high power laser facilities deliver the energy required for the ignition. When the laser beams uniformly hit the ICF target, the ablation layer is heated up rapidly and forms a plasma envelope. The deuterium and tritium is compressed by the blow-off of the hot surface material. As a consequence, the fuel density reaches up to 47 times that of lead, and the temperature is heated up to 100 million degrees Celsius, which enables fusion to occur [15]. The thermonuclear burn spreads rapidly through the compressed fuel and releases energy, which is many times that of the input energy. The whole process is completed in a few nanoseconds so that the hot fuel plasma does not leave the original place – hence the term “inertial confinement”. Compared with the other two methods, inertial confinement fusion has the highest energy density, and involves full compression of the fuel.

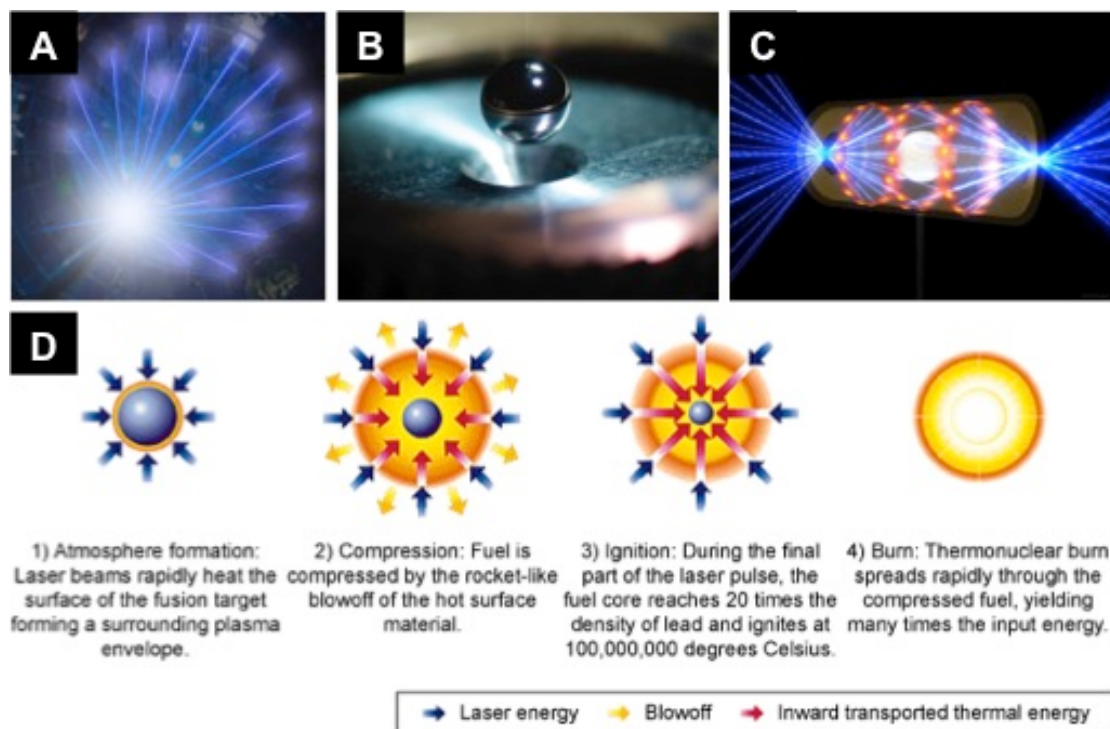


Figure 3.4 Inertial fusion reaction. **A.** Schematic drawing of the directive drive laser ICF that high power laser beams deliver energy to the center of the reactor where **B.** a fusion target is sent to. **C.** Schematic drawing of the indirect drive laser ICF that a fusion target is placed in a ‘hohlraum’ and high intensity X-rays are used to trigger the fusion reaction. **D.** Schematic drawing of ICF target ignition.

The physical properties of the ICF targets are highly critical [16-18] and completely determine the fusion process, as shown in Table 2. Among them, the high sphericity and concentricity of the ICF target reduces Rayleigh-Taylor instability, which in turn results in a low fuel plasma temperature, and ignition failure [14, 19]. Those conditions increase the difficulty of ICF target fabrication. Conventional bulk methods have a very low yield rate and a relatively long manufacture period. The cost reaches ~\$2000 per capsule due to high material and energy consumption, whereas the economical cost of the ICF target is \$0.6 per capsule. For a commercial ICF power plant, ICF targets need to be shot into the reactor at ~15Hz [20, 21]. Advanced manufacturing methods are required to produce the ICF targets that are more efficient, both for research projects and in future power plant applications.

Table 2. Specifications of ICF targets.

<i>Composition</i>	<i>Diameter</i>	<i>Wall thickness</i>	<i>Density</i>	<i>Sphericity</i>	<i>Concentricity</i>	<i>Porosity</i>	<i>Roughness</i>
<i>C, H, O or C, H</i>	<i>0.5-4.0</i> <i>mm</i>	<i>100 μm</i>	<i><250</i> <i>mg/cm⁻³</i>	<i>>99.9%</i>	<i>>99%</i>	<i><1 μm</i>	<i><50nm</i>

3.1.4 Current progress of ICF target fabrication

The fabrication of ICF targets has progressed by various developments over the last few decades. Generally, the procedures for fabricating ICF targets have included (1) shaping the hollow spherical outer shell, (2) coating, (3) fuel injection, and (4) sealing and surface smoothing. The materials of the target shells (Figure 3.5) can be categorized to three groups: metals, glass, and plastics; and diverse target shell manufacturing methods have been developed. The metals used to shape the microcapsules include lithium and beryllium, and their compounds. These light elements exhibit high plasma stability, hot plasma burning, and reduce the mixing of shell material with the fuel. However, the main drawback of light elements and their hydrides is their relatively low initial ion concentration, which inhibits progression

towards the necessary compression degree and DT density. In addition, large sized targets are hard to synthesize from the metal materials. Glass, as an alternative material for ICF target fabrication, offers excellent sphericity, surface finish, high strength and proper DT fuel gas permeability [22]. Various approaches have been developed to produce hollow spherical glass capsules such as the liquid droplet method [23], the sputtering deposition technique [24], the Hoppe method [25], and the dried gel method [26]. However, glass materials also have several drawbacks as the candidate material. For instance, it is difficult to embed other elements (e.g. Al, Mg, Ca.) in glass to increase the shell strength. The processing parameters for glass shell formation are hard to optimize (e.g. size of feeding particles, furnace gas pressure, and hot zone dimension). In addition, it is also hard to obtain large (>400 microns) spherical glass targets with a uniform shell thickness.

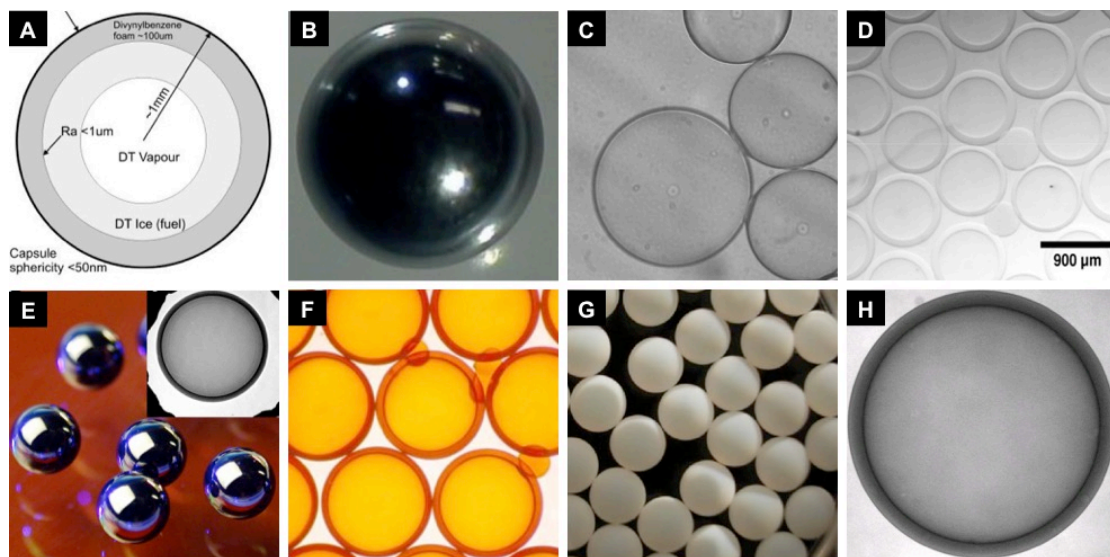


Figure 3.5 Inertial confinement fusion targets. A. Schematic drawing of ICF targets. B-H. Solid shells from diverse materials for ICF target fabrication. B. Beryllium [27]. C. Glass [23]. D. Silicone aerogel. [28] E. Diamond [29]. F. RF foam [30]. G. DVB foam [44]. H. TMPTA foam [33].

Nowadays, the most adaptable materials for ICF target fabrication are plastics. There exists a well range of polymers composed by low atomic number elements (low Z), with low density and atomic weight, which can be used to form discrete layers of

the ICF targets. The typical diameter of a polymeric shell is $\sim 870\mu\text{m}$, with a surface roughness of $\sim 60\text{nm rms}$. In addition, highly porous materials can be synthesized by adding porogens to the polymer precursors. The attained foam shells have several advantages that make them suitable for ICF target fabrication, including (1) extremely low density, and (2) high fuel absorbance and storage; furthermore and (3) they are not dependent on drill-based fuel injection [31, 32]. Finish over-coating is required to seal the open cells on the outer surface following fuel injection. Furthermore, the functional groups on the polymer molecule chains can be incorporated with other molecules, which allows the physical and chemical properties to be modified [33].

Many approaches have been developed to fabricate polymeric ICF targets, including drop-tower [34], micro-emulsion [30], mandrel dissolving [35], and interfacial polymerization techniques [36]. Among them, the micro-emulsion method is considered the most simple and feasible method for mass production. Double emulsion droplets are produced in sequential solvent emulsifications, and are utilized as the template for the polymeric microcapsules. The polymer precursors are consolidated into a shell *via* phase solidifications such as free radical polymerization or solvent evaporation. The encapsulated phase is dried out and the shells are finished with a CH permeation overcoat for fuel diffusion. The hollow microcapsules are then soaked in liquid deuterium and tritium, and a layer of full density, single crystal DT ice is formed by a slow cryogenic procedure (14h). After a low IR surface smoothing process, the fabrications of ready-to-use ICF targets are completed. The whole procedure normally takes several weeks and the yield rate is largely limited by the bulk emulsification method due to the large size distribution of the primary shell. Hence, droplet microfluidics, which can be used to produce monodispersed multiple emulsion droplets, have replaced the conventional method of ICF target fabrication.

3.1.5 Droplet microfluidic for ICF target formation

In last five years, increased efforts have been conducted in fabricating polymeric microcapsules *via* droplet microfluidics. Cécile Lattaud managed to produce low-density TMPTA foam shells by using capillary microfluidic devices (Figure 3.6) [37]. Discrete polymer segments encapsulating water droplets were produced from W/O/W double emulsions by a one-step emulsification method *via* a tripled orifice droplet generator. The double emulsion droplets were stabilized by adding surfactants into the inner and continuous phases. After formation, the core-shell shaped droplets flowed into a long wound tubing (patented by CEA), wherein which the movement of microcapsule was subject to the velocity gradient and gravity. [38] The TMPTA shell phase was then thermopolymerized, a process that lasted between several minutes and a few hours, depending on the temperature. The solid shells were collected and stored in a rotating flask, which was filled prior to the next procedure of drying the foam shell. Lattaud aimed to improve microcapsule concentricity and sphericity by tuning experimental parameters such as the density gaps between the inner phase and the organic phase [39], the alignment of the capillaries, the interfacial tension [40], the type of outlet tubing, and the temperature of thermopolymerization. As for the product characteristics, the attained foam shells had a 2.4% average non-concentricity and 99.86% sphericity with a 58% yield rate; the density gap was 0.078 g/cm^3 ($d_{\text{Water}} - d_{\text{Organic}} = 0.078 \text{ g/cm}^3$) and the thermopolymerization was undertaken at 60 Celsius degrees. In terms of microfluidics, this approach has several advantages in the production of monodispersed double emulsion droplets. The layout of the triple orifice droplet generator prevents wetting issues, and also prevents the encapsulated water droplets from moving out of the organic phase. The one-step emulsification method enables thin layer shell phase

formation, which is normally impossible through the two-step method [41]. Furthermore, the thermal polymerization process is highly reproducible, and both high concentricity and high sphericity of polymeric foam shells are obtainable. However, a few limitations have been reported by Cécile Lattaud:

- (1) A form of shell train was seen to be flowing in the tube where the polymerization occurred. This may have resulted from the size variation of the double emulsion droplets since different size droplets and particles travel at diverse linear velocities in the Poiseuille flow. Two factors can lead to the size variation in the droplets that are formed: imperfection of the microfluidic device, and the presence of satellite droplets. As is expected during viscosity break-up, satellite droplets are byproducts of the primary droplets. Failure to remove the satellite droplets from the main flow will induce unexpected coalescence, which leads to size variation.
- (2) Thermal polymerization limits the yield rate of the foam shells. The activity of the thermal initiator is highly dependent on the system temperature. The number of free radicals in the precursor is limited by the low solubility of the thermal initiator. The duration of thermal polymerization is relatively long (>20mins). The yield rate of the shell drops dramatically, as do concentricity and sphericity, whenever the temperature is raised to shorten the polymerization period [42].

Despite these limitations, Cécile Lattaud's work is a great example of the production of TMPTA microcapsules *via* droplet microfluidics ICF target fabrication, which supplies the target fabrication for the CEA Valduc LMJ Simulation program.

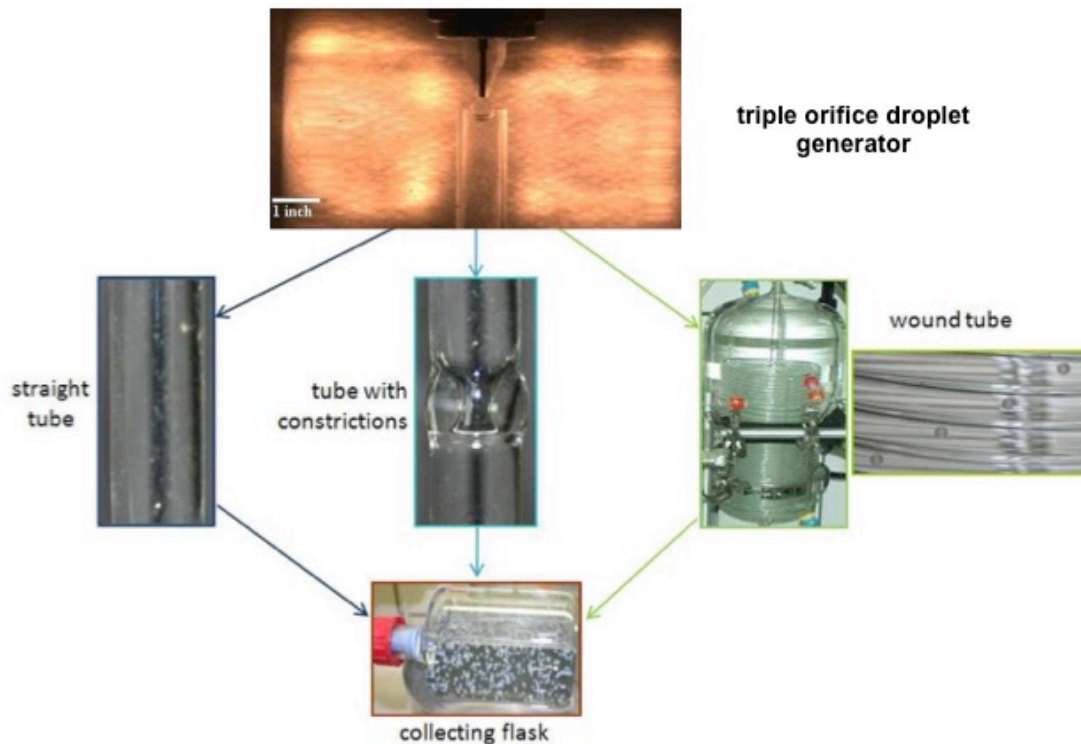


Figure 3.6 The procedure of TMPTA shell fabrication via capillary microfluidic devices. From top to bottom, the double emulsion droplets were formed using a triple orifice droplet generator, thermopolymerized in long tubing, and collected in a rotating flask.

Another study was conducted by Matthew Moynihan from the University of Rochester to produce oil/water/oil double emulsion droplets *via* planar microfluidic devices. In the first stage of their ICF target fabrication process, they generated droplets with on-chip droplet volume calibration [43]. The droplets were then sent to a fluid processor for double emulsion droplets centering through a dielectrophoretic method prior to shell phase solidification. The gelled microcapsules then underwent solvent exchange under pressurized flow. The last stage included heating and critical point drying of the foam shells for fuel injection [44]. This fabrication system is still being developed, although initial progress has been reported. Planar microfluidic devices with double T-junctions were used to form double emulsions through a two-step emulsification method (Figure 3.7A). Oil droplets were dispersed in the water phase to form the first emulsion, and were then sheared off by another oil phase so that the RF double emulsion droplets could be isolated. The channel wettability was

changed from being hydrophilic to being hydrophobic, with the employment of a glass-plastic bonded microfluidic chip (which was of a glass into plastic junction design, wherein the glass was sealed by hydroxide-catalyzed bonding). This microfluidic device was found to produce a 2.5mm diameter segment with a 0.77mm shell thickness at 1.9Hz. However, it has been reported that the size distribution of double emulsion droplets is wide, and only one out of three droplets can be used for the next step.

An alternative microfluidic method was developed by Weiqiang Wang (at the University of Rochester), whereby an electrowetting-on-dielectric (EWOD) process and dielectrophoresis were used to produce double emulsion droplets (Figure 3.7B). [45] In this method, water droplets and oil droplets were dispersed in air separately on an aluminum plate, and were driven to the same place by an AC electrical field (from an embedded waffle-like electrode array). When the water droplets and oil droplets made contact, spontaneous emulsification combined them within the open section to form either an O/W/A or a W/O/A double emulsion droplet in the presence of surfactants. The obtained droplets were collected in a container filled with inner phase solution by tilting the substrate.

This digital microfluidics method offers a flexible and scalable system to manipulate each phase individually during the formation of double emulsions. It also helps to reduce interactions between the adjacent droplets (in contrast with continuous droplet microfluidics), and avoid unexpected coalescence.

Furthermore, the researches at the University of Rochester developed an active method to center the double emulsion droplets in a density gradient suspension by applying a uniform AC-electric field ($>10^4 \text{VRMS} \cdot \text{m}^{-1}$) [46]. Three criteria were

identified to achieve this centering process: (1) the dielectric constant of the shell phase must higher than the dielectric constant of the suspending liquid; (2) the AC electric field frequency must overcome electrostatic shielding; and (3) the liquid densities must be matched within a margin of $\sim 0.1\%$ (Figure 3.7 C, D). The performance of this centering approach exhibits oblate distortion of $<2\%$ for the shell, and a prolate distortion of $<1\%$ for the inner droplet, with a $<5\%$ drops in center offset in a $\sim 60\text{s}$ time period. The centralized double emulsion droplets were then photopolymerized by the UV irradiation for about 25s.

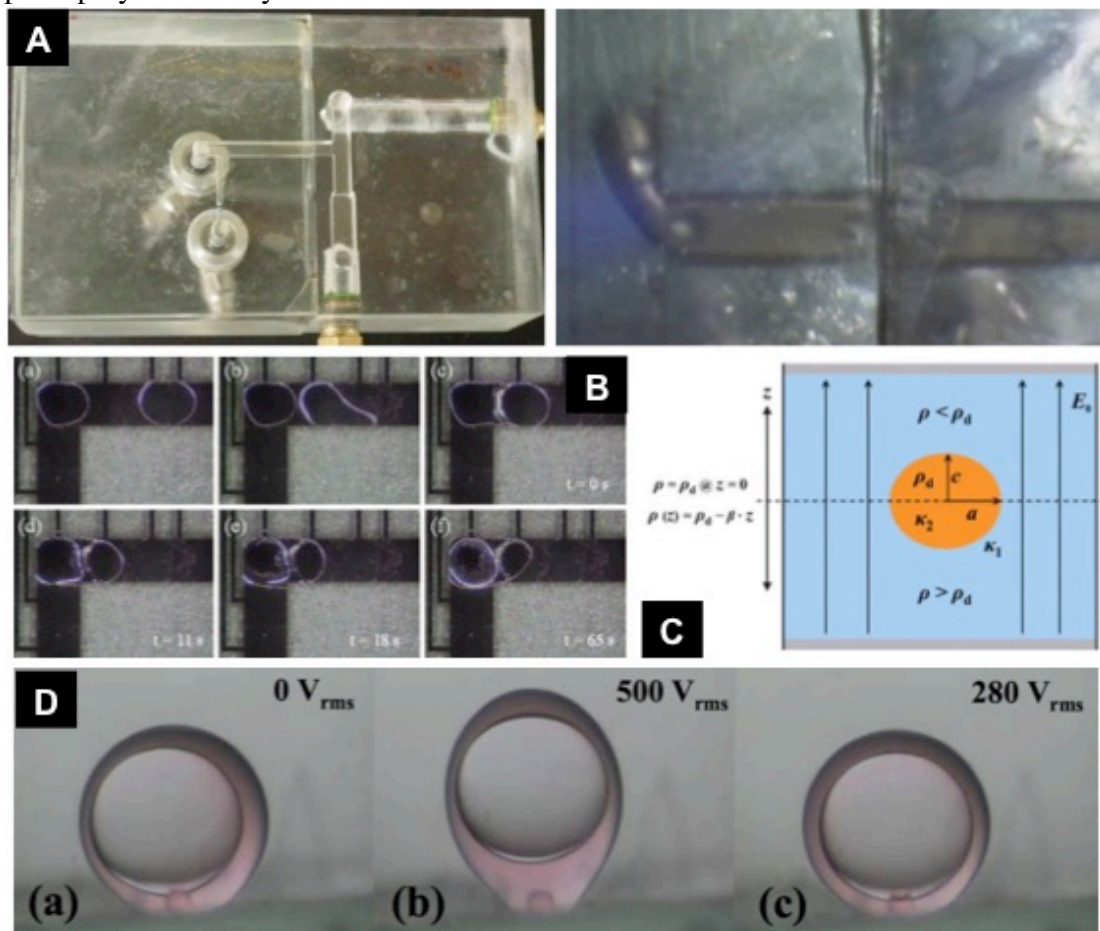


Figure 3.7 The reported work on RF foam shells for ICF target fabrication in University of Rochester, America. **A.** A planar microfluidic chip with double T-junctions for the oil/water/oil double emulsion droplets formation. **B.** Sequence images of EWOD process for the formation of oil/water/air double emulsion droplets. **C, D.** Centering of double emulsion droplets suspended in a density gradient by applying an AC electric field.

In terms of microfluidics, a double T-junctions layout on a millimeter scale exerts less control on double emulsion droplets formation. An obvious volume variation of attained droplets has been observed, which induces the coalescence. Hence, the production rate is far below that required in a single ICF reactor. Meanwhile, there is also an issue of droplet volume variation in the EWOD method. The minimum volume variation is 3% in a very specific operating condition, and this value increases dramatically to 40% when a large cutting electrode is used to produce large droplets. Although the concentricity and sphericity of double emulsion droplets can be improved to the point where they match the ICF target specifications by applying an AC electric field, the photopolymerization leads to deformation of the shape of the solid shells. Shape deformation might result from uneven polymer shrinkage during rapid consolidation, which induces destabilization of the centralized core-shell shape double emulsions droplet. The best sample shells they have fabricated possess a 7.85% non-concentricity, which is achieved by occasional UV light source adjustment.

There has been similar research into ICF target fabrication *via* droplet microfluidics technology. Bo Li and Sufen Chen utilized double T-junctions microfluidic devices to fabricate polyacrylonitrile (PAN) microcapsules. [47] An O/W/O density-matched double emulsion was applied as the template, and the shell phase was consolidated by using a rotary evaporator to drive off the dissolving PAN. The attained PAN microcapsules ranged diameter from 100 to 1000 microns, and the thickness ranged from 30 to 300 microns. Paguio and Takagi reported on the fabrication of divinylbenzene (DVB) foam shells *via* a triple orifice droplet generator. [48] Two thermal initiators, the 2, 2'-azobisisobutyronitrile and the azo-type initiator V-70, were used to improve the yield rate of the intact shell, and to improve the

shell's mechanical properties. The obtained microcapsules were 800 to 3500 μm in diameter, and the shell thickness was 7% to 10% of the diameter. Yi Cheng and Shao Ting produced hollow polymer capsules made of polystyrene (PS) (that has been dissolved in fluorobenzene) by using a dual-coaxial capillaries device [49]. This work focused on the control of W/O/W double emulsions generation with both the one-step and two-step method.

In this chapter, an approach for the mass fabrication of monodispersed TMPTA microcapsules using planar PTFE microfluidics devices is demonstrated. The W/P/O double emulsion droplets were generated using the two-step emulsification method, and solidified by photoinitiated free radical polymerization. Two aspects were considered: (1) miniaturize variations in the volume of double emulsion droplets, and avoid unexpected coalescence; and, (2) reduce polymerization kinetics-induced shell deformation, and improve the sphericity and concentricity of attained polymeric microcapsules. The next section is a brief introduction of photoinitiated free radical polymerization, and includes an overview of the factors that influence the shape of the shells.

3.2 Free radical polymerization

Free radical polymerization is a technology used for polymerizing globules containing an organic monomer and an organosoluble initiator. It is one type of chain growth polymerization, whereby initiating free radicals react with the monomer units to generate successive building blocks of growing polymer chains. More than 50% of commercial polymers and material composite are synthesized using this method including polyvinyl chloride (PVC), polyethylene (PE), polystyrene (PS), polytetrafluoroethylene (PTFE) and poly(methyl methacrylate) (PMMA).

3.2.1 Thermal-initiated free radical polymerization

The polymerization reaction can be triggered in the presence of thermal initiators in the monomer phase at moderate temperature (normally between 40 and 150 Celsius degrees). The thermal initiators are activated, and they supply free radicals in specific temperature intervals, according to the decomposition kinetics. Only part of the yield radicals contribute to the growth of polymeric chains and others are lost in side reactions. The thermal polymerization process can last from several minutes to a number of hours, and it requires accurate control of the system temperature, which dramatically affects the cost of fabrication.

3.2.2 Photoinitiated free radical polymerization

Photopolymerization is a chain-growth polymerization that is initiated by the absorption of ultraviolet or visible light. The light energy is absorbed by the reactant monomers, which release free radicals and crosslink with polymer molecules. The photopolymerization rate is decided by the concentration of the reactant monomers and the path length of light. Additives, fillers or other monomers in the polymer composite system, which absorb similar wavelength light, will influence polymerization efficiency.

3.2.2.1 Photoinitiators

Photoinitiators are chemical compounds used in photo-polymerization reactions, and can be found both in nature and within industry. Two types of photoinitiator homolysis processes have been found. In the type I process (Norrish type I reaction), the initiators decompose into two free radicals when exposed to UV light of a sensitizing wavelength. In the type II reaction, the initiators decompose *via* intermolecular hydrogen abstraction in the presence of a hydrogen donor molecule

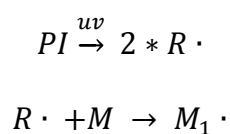
under the UV irradiation, for example a photosensitizer. For an efficient polymerization, the photoinitiator should satisfy three criteria [50]: (1) there should be high absorption within the emission spectrum; (2) the singlet and triplet excited states should have a short lifetime to avoid being quenched by the monomer and oxygen; and, (3) there must be a high yield of free radicals which are active with the monomer molecules.

3.2.2.2 Photoinitiated free radical polymerization process

Three kinetics steps have been identified in the free radical polymerization processes: initiation, propagation, and termination [51-53]. These three steps take place when polymerization begins, and when the monomers, the growing polymeric chain and the dead chain are coexisted in the solvent.

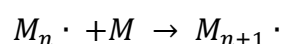
Initiation step

Two reactions happen during the initiation step. One is the decomposition of the initiators through photochemical reactions, which yields free radicals. The other is the reaction between the primary radicals and the monomer molecule to form chain-initiating radicals:



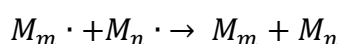
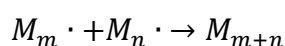
Propagation step

The chain-initiating radicals then successively react with other monomer molecules to form an initiating polymeric chain. The reactivity remains the same for the initiating polymeric chains that contain a diverse number of monomer units. The reaction progresses quickly and the high molecular weight chain is normally formed under one second.



Termination step

Once the radical units of an initiating polymeric chain are annihilated, the polymerization of the chain is terminated. Two types of bimolecular free radical reactions occur at the termination of polymerization. One is the combination of two initiating polymer chains to produce one dead polymeric chain of an additional length. The other one is the disproportionation of two initiating chains, which results in the formation of two dead polymeric chains. The hydrogen abstraction results in the formation of one chain with saturated extremity, and another chain with unsaturated extremity:



3.2.2.3 Crosslinking

The crosslinking of mono-functional monomers only forms linear networks, whereas multi-functional monomers such as di- or tri-vinyl monomers can build three-dimensional cross-linked networks. The monomer functionalities increase with increasing crosslinking density and polymerization rate, although a high conversion is difficult to achieve.

3.2.2.4 Free radical polymerization kinetics

The rate of photoinitiated polymerization is measured by the rate of monomer consumption. As the concentration of free radicals is very low ($\sim 10^{-8}$ M) in the solution, it is difficult to accurately measure them [51]. A steady state assumption is made that the radical production rate is equal to its consumption rate, and hence the

concentration of free radicals remains the same in the polymerization process. With this assumption, the rate of photopolymerization at any depth across a specimen can be calculated by the equation shown below, provided that the molar absorptivity, light intensity, and the distance from the surface to the depth are known:

$$R_p = k_p [M] \left(\frac{\phi I_0 (1 - e^{-2.3\epsilon[A]D})}{k_t} \right)^{1/2}$$

-whereby k_p is the rate constant of the propagation step, $[M]$ is the concentration of double bonds, ϕ is the photoinitiator efficiency, I_0 is the incident light intensity, ϵ is the molar absorptivity of the photoinitiator, $[A]$ is the concentration of absorbing species, D is the distance, and k_t is the constant rate of the termination step.

The above equation has been obtained from substitution of a few primary equations [51, 54]. Photo-differential scanning calorimetry (photo-DSC) and real time Fourier transform infrared spectroscopy (FTIR) can be used to measure the rate of bulk photoinitiated free radical polymerization.

3.2.2.5 Advantages and disadvantages of photoinitiated polymerization

Compared with the thermal polymerization, photoinitiated polymerization has several advantages: (1) most of photopolymerization can be conducted at an ambient temperature; (2) photopolymerization can be spatially directed by the placement of light sources; (3) the starting point of photopolymerization is controlled by the switching of the light source, which is programmable with electronic circuits; (4) photopolymerization is solvent-free, and the use of volatile organic compounds as solvent intermediates can be avoided (and thus 100% solid content can be obtained); and, (5) the rate of photopolymerization is much faster than thermal polymerization, which allows for greatly reduced energy consumption.

Two main disadvantages of photopolymerization are as follows: (1) the light intensity is attenuated in the thick polymer film, especially films with fillers or light-absorbing additives in the polymer composites. This low energy penetration leads to a significant decrease in both the reaction and conversion rates; (2) to solve the issue of disadvantage (1), the photopolymerization system needs to be modified, which will change the original properties of the materials, and increase cost.

3.2.2.5 Factors affecting photopolymerization

Gel effect

The gel effect (Figure 3.8A), also known as the Trommsdorff effect, is the auto-acceleration of the polymerization rate that has been observed in many free radical polymerizations when a certain conversion is reached [52]. This phenomenon is induced by an increase in system viscosity during the formation of large molecule chains in the bulk polymer solution during the polymerization process. The diffusion rate of chain-initiating radicals slows down, and so the termination rate decreases rapidly. As a consequence, the polymerization rate is suddenly raised which will lead to variations in the features of the polymers produced [55].

Oxygen inhibition

The presence of oxygen in the specimen leads to the inhibition of free radical polymerization by quenching of the excited initiator or by transfer reactions with

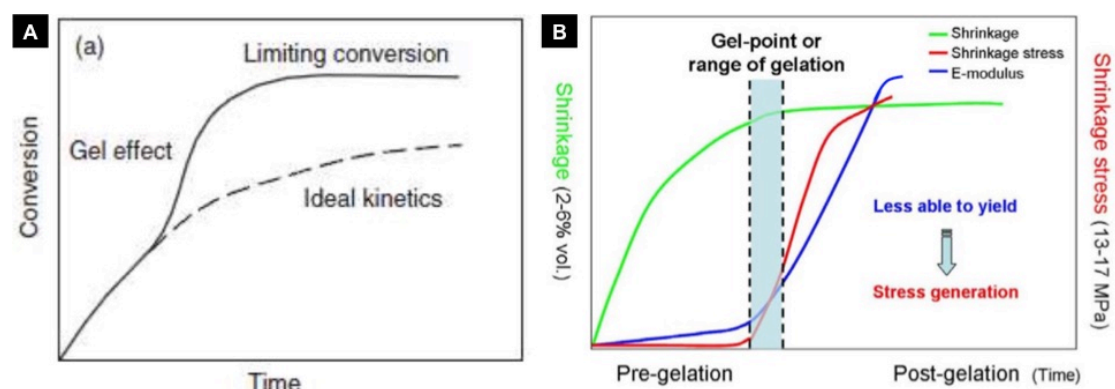


Figure 3.8 Factors influenced the performance of photopolymerization. **A.** Gel effect. **B.** Volume shrinkage and related internal stress during the photopolymerization.

initiator. The resulting peroxide radicals possess a low activity, and cannot trigger propagation. A procedure of degasification is always required to remove the dissolved oxygen from the solvent system, and the polymerization should be conducted in an inert atmosphere.

Polymer shrinkage

When polymerization occurs, monomer molecules move closer and crosslink with each other. The polymeric molecular network is formed through intense covalent bonds formation, which induces bulk contraction [56]. This volumetric shrinkage normally takes place prior to specimen solidification. High polymer shrinkage and its subsequent stress are widely found in multifunctional (meth) acrylate systems, and is the subject of much research, namely in dental composites (Figure 3.8B) [57]. The polymerization shrinkage has been measured to range from 0.2% to 2% linearly, and 1.5% to 6% volumetrically, and the stress can vary from 5MPa to 17MPa [58]. To overcome this drawback, several methods have been developed, including thiol-ene photopolymerization, and inorganic nanofillers incorporation [59-61].

3.3 Experiment

3.3.1 Material and chemicals

Trimethylolpropane triacrylate (TMPTA), inhibitor remover, glycerol, mineral oil, sudan red, oil red O, oil blue N, photoinitiator, acetone, IPA, chloroform, toluene, hydrogen chloride, triton X-100, vinyl trimethoxy silane, multi-walled carbon nanotubes (MWCNT), and multi-walled carbon nanotubes with carboxylic acid functional groups were all purchased from Sigma Aldrich.

3.3.2 Solvent preparation

The purchased TMPTA solution contained solubilized inhibitor to prevent degradation and polymerization. To remove the inhibitor, the TMPTA solution was filtered with a glass column filled with inhibitor remover, and collected in a dark brown glass container. The process was conducted in an amber chamber to prevent any UV irradiation from daylight. Following inhibitor removal, 5% v/v photoinitiator was added into the filtered TMPTA solution, and the mixture was homogenized *via* a 10-minute sonication. The density of the polymer composite was then measured at ambient temperature. The aqueous phase was prepared with glycerol, and deionized water (which was density-matched with the polymer phase). Mineral oil was used directly, and stored in a clean glass container. All the solvent transfers and preparations were performed in a fume cupboard. Prior to their use, the solvents were degasified in a vacuum oven at 25 degree Celsius for one hour.

3.3.3 Photopolymerization of double emulsion droplets

In this experiment, 5W 365nm wavelength UV LEDs were used to photopolymerize the TMPTA monomers. Initially, the double emulsion droplets were cured with a single UV LED placed on top of the microfluidic devices, and flowed in a square section channel. An additional FEP film, which had been pre-coated using a gold sputter machine to form a devised pattern on the surface was attached to the glass window as a mask to confine the UV illuminated area, and prevent unexpected polymerization. A PTFE O-ring shaped attachment was aligned with the circular chip to collect the cured samples from the side of the microfluidic device. In so doing, the clogging issue that occurs within right angle bottom outlets was avoided.

In the next stage, the double emulsion droplets were photopolymerized as they flowed in the PTFE tubing that was linked with the microfluidic chip outlet. The

tubing was held by utility clamps on a ring stand, and kept straight with the use of weights. The UV LEDs were also held in the same manner, and placed against the tubing at the desired point. The attained microcapsules were collected in groups of 50 in glass containers, which were prefilled with mineral oil. The sphericity and concentricity of the microcapsules were calculated using the equation below:

$$Sphericity = 1 - \frac{D_{max} - D_{min}}{D_{avg}}, \quad Concentricity = 1 - \frac{d}{D_{avg}}$$

-whereby D_{max} is the maximum diameter, D_{min} is the minimum diameter, d is the distance between the inner circle centre and the outer circle centre of the microcapsule, and D_{avg} is the average diameter.

3.3.4 MWCNT-TMPTA polymer nanocomposite preparation (MWCNT)

Carbon nanotube (CNT) material is one of the nanofillers utilized in the polymer composite systems. It exhibits extraordinary physical properties such as high stiffness, excellent thermal and electrical conductivity, and low density. However, due to the hydrophobic nature of CNTs, they tend to agglomerate in polymer solution. This phenomenon reduces the performance of CNT dramatically. The main challenge of applying CNT in polymer composites is finding a way to achieve a fine dispersion. In this study, MCNTs with carboxylic acid functional groups were finely dispersed in TMPTA solution in the following procedure:

Initially, the MCNTs were reacted with vinyl trimethoxy silane in an acid reflux procedure for 4 hours. The mixture was then poured into a Buchner funnel with filter papers (Whatman, mesh size = $1\mu\text{m} \times 10\text{nm}$) to filter out the solid particles. The attained MWCNTs were washed three times with toluene, acetone and methanol, (respectively), and left to air-dry. During the preparation of the TMPTA nanocomposite, the functionalized MWCNTs were physically mixed with TMPTA

solution using a homogenizer (Hielscher 1KW sonicator). When polymerizations commenced, the functionalized MCNTs should cross-link with the TMPTA monomers *via* a covalent reaction between double vinyl bonds. The dispersion of MWCNT in bulk TMPTA was measured with an HRTEM (JEM-2100 LaB6). The mechanical properties of cured MWCNT-TMPTA composite was tested using a TA-Q800 fiber mechanical testing machine at the Waterford Institute of Technology in Ireland.

3.4 Results and discussion

The synthesis of polymeric shells for the ICF targets fabrication included (1) consistent double emulsion droplets formation *via* droplet microfluidics, (2) rapid on-chip photopolymerization, and (3) MCNT-TMPTA nanocomposite fabrication. This combination of droplet microfluidics and photopolymerization in fabricated polymeric microcapsules has the advantages of high throughput and production uniformity, low reagent and energy consumption, and a shorter fabrication period. In this experiment, the formation rate of monodispersed double emulsion droplets reached up to 20Hz without coalescence. Both the concentricity and sphericity of attained solid shells were above 98% with controlled photopolymerization. The presence of functionalized MCNT improved the strength of solid TMPTA sample by 50%. Although further tests need to be completed for the development of ready-to-use ICF targets (such as the fabrication of high porosity materials and the development of online fuel injection microfluidic modules), this experiment offers a promising approach for mass production of ICF targets in future applications.

3.4.1 Double emulsion formation

A high rate of replicate droplet generations is essential for precise fabrication of microcapsules. During the formation of double emulsions, the size variation of droplets should be miniaturized as much as possible. This not only increases the system stability, but also reduces the efforts expended in droplet volume calibration and sorting. In addition, for on-chip ICF target fabrication, the spherical shape of the double emulsion droplets in the flow must be maintained until polymerization is completed. Hence, the diameter of double emulsion droplets should be controlled in the (0.5~1) channel dimension, so as to ensure that the movements of droplets are close to the centerline. In this study, monodispersed single-core water/TMPTA/oil double emulsion droplets of a controllable size were produced, as described in the previous chapter (Figure 3.9 A-D).

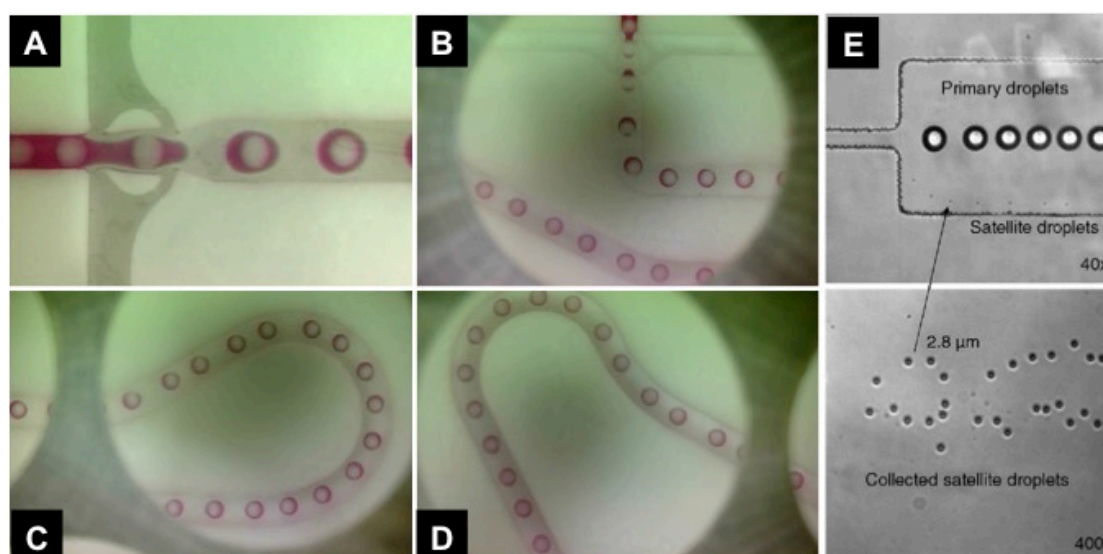


Figure 3.9 Formation of monodispersed water/TMPTA/mineral oil double emulsion droplets via a planar PTFE microfluidic chip. **A.** The double emulsion droplets were formed in a bat-wing junction without satellite droplets. The channel dimension is same as the ones demonstrated in Chapter 2. **B-D.** Double emulsion droplets flowed in the channel without coalescence. **E.** Primary droplets and satellite droplets. The large droplet tended to stay in the centerline while the small ones flowed near the wall [65].

Control of droplet coalescence

Droplet merging is one main issue that constrains the production rate of double emulsion droplets, and this has been widely reported in previous studies into ICF target fabrication *via* a microfluidic approach. The unexpected coalescence, either in a duct or a piece of tubing, leads to an irreversible change to the droplet morphology and increased polydispersity. During the polymerization, droplet coalescence leads to the formation of “train shells” of several microcapsules packed one on top of another, which clog the microfluidic system.

The coalescence of droplets in microfluidics is mainly induced by the size variation of the droplets. In pressure driven microfluidic flow, namely Poiseuille flow, the size of a droplet determines its route and swimming velocity. Compared with small droplets, large droplets tend to flow closer to the centerline, and travel faster due to the large area section and pressure difference (Figure 3.9E) [62, 63]. When a large droplet flows behind a small droplet (both the droplet diameters are smaller than the channel width), the distance between them decreases continuously as the large droplet catches up with the small droplet, before eventually absorbing the small droplet. If the two droplets merge together, the resulting droplet will have a higher linear velocity than both parent droplets, and will chase any other small droplets in front of it. This ‘Nibbles game’-like phenomena is terminated when all the spherical droplets in the system coalesce into large fluid segments, whose cross-sectional area is the same as the channel dimension.

To avoid droplet merging in a microfluidic channel, one can increase the distance between adjacent droplets and improve the droplets’ monodispersity. The distance can be increased easily by injecting an extra continuous phase into the double emulsion system. For this study, an additional mineral oil inlet was placed beyond the droplet-forming junctions. The mineral oil input from this inlet not only increases the

distance between the adjacent droplets, but also provides a method for controlling the linear velocity of double emulsion droplets in the continuous flow.

In microfluidics, the monodispersity of the double emulsion droplets is affected by many factors including the solvent property, the type of droplet generator, and the accuracy of chip fabrication. Satellite droplets are the byproducts of viscosity droplet breakup, which contribute to droplet size variation as they randomly merge with the primary droplets [64]. The removal of satellite droplets requires extra efforts such as the use of droplet sorting channels [65]. In this study, the satellite droplets were eliminated by regulating droplet merging using the bat-wing junction. When the double emulsion droplets were sheared off, the attained satellite droplets stayed in a stationary position and merged with the incoming dispersed phase, and did not escape from the droplet-forming junctions to the collection channels. This was due to the presence of eddy flows at the bat-wing junction during droplet formation, which required droplet breakup point control in the expansion zone by tuning the continuous phase input flow rate.

Control of droplet formation frequency

By tuning the W/P/O input parameters, it was possible to increase the shear rate of TMPTA double emulsion droplets up to 20Hz in this experiment (Figure 2.6 d). With the additional mineral oil to increase the distance, no coalescence occurred in the polymerization process. The maximum flow rate of the additional oil inlet was 80 ml/hour. Beyond this value, the double emulsion droplets were ripped up by the violent flow.

3.4.2 Photoinitiated polymerization of double emulsion droplets

As described above, in contrast with thermal-initiated polymerization, photoinitiated polymerization has the advantages of easy manipulation, fast reaction

rate, and low energy consumption. In this study, the main concerns when using photopolymerization to produce polymeric shells *via* droplet microfluidics included (1) droplet shape deformation in dynamic flow [66, 67] and (2) volume shrinkage and related stress during polymerization. These issues have been reported to influence the quality of the sample.

3.4.2.1 Photopolymerization in the microfluidic channel

In the first attempt, the TMPTA phase was cured when the double emulsion droplets flowed in the square section channel on the microfluidic chip. It was observed that the linear velocity of droplets decreased when the droplets flowed into the UV-illuminated area once the phase conversion has started. Once the microcapsules no longer exposed to the UV irradiation, they no longer coalesced with one other, and even flowed in a wolf pack fashion. The solid samples attained from this experiment had several defects (Figure 3.10) that can be categorized to two groups:

Shell disruption

Two types of shell disruptions were found in the solid samples. One type of disruption appeared as a circular window on the shell surface, which had been induced by the offsetting of the water core during TMPTA solidification. The water core inside the double emulsion droplets leaked out from the polymer envelope, and the solid shell was warped into a bucket shape (Figure 3.10 A-C). The other shell disruption appeared as an axe-cleavage-like defect on the shell surface (Figure 3.10 D, E). These two defects of the microcapsules were induced by volumetric shrinkage and internal stress of the polymer during the photopolymerization process, which were also observed in the bulk system.

Shape deformation

The resulting solid particles appeared to be irregularly shaped rather than spherical or elliptical (Figure 3.10 G). The water core was offset from the center of the microcapsule (Figure 3.10 F). The polymer phase accumulated at one side of the microcapsule, and did not form a shell of uniform thickness. These characteristics of the microcapsules resulted from the parabolic shaped velocity profile of the Poiseuille

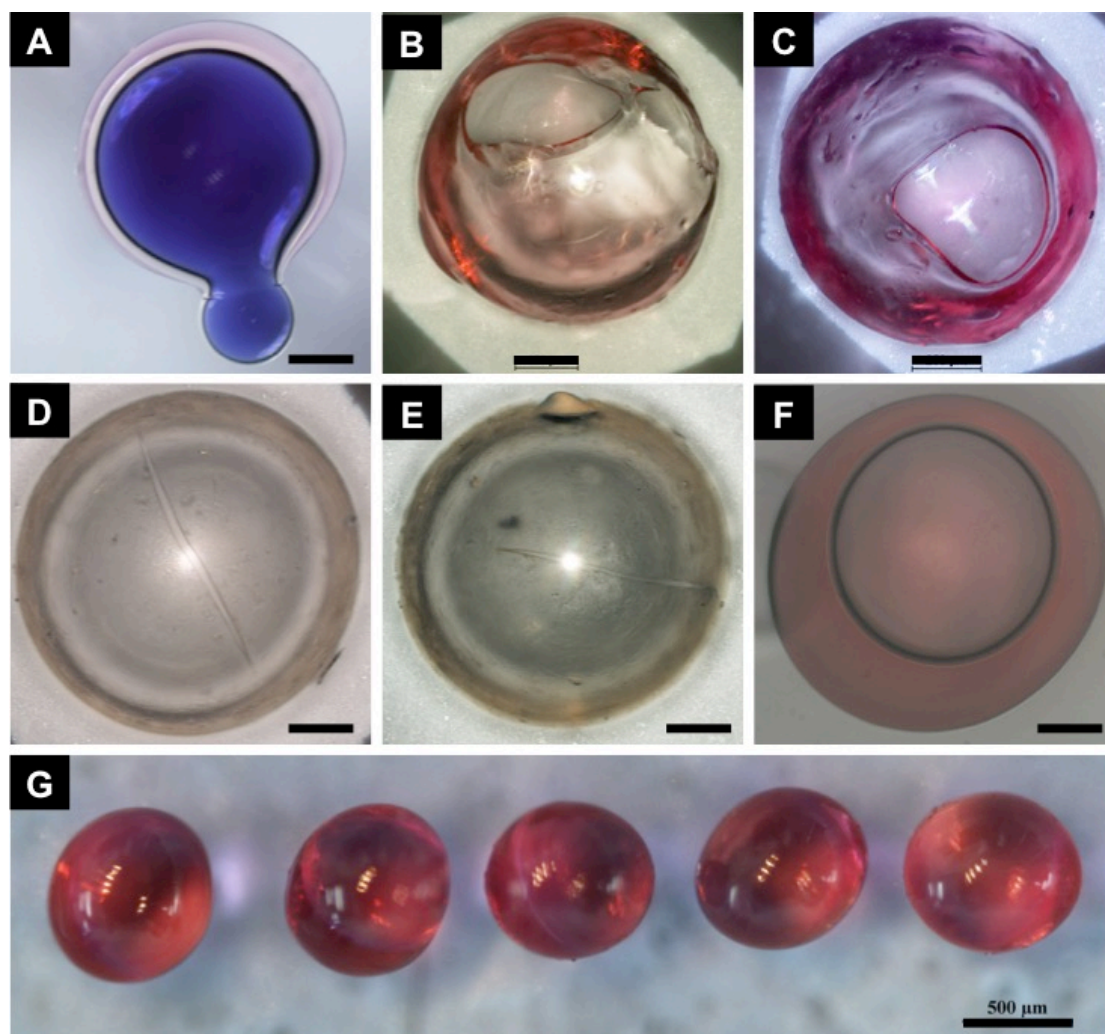


Figure 3.10 Defects of solid TMPTA microcapsules. A-C. Photographs of solid TMPTA microcapsules with open windows on the surface. A. Water core leaks out from the open window. D, E. Photographs of solid TMPTA microcapsules with an axial cleavage-like defect on the surface. F. Core offset of the solid TMPTA microcapsule. G. Photographs of non-spherical intact TMPTA microcapsules. All the scale bars are 250 microns except the one in G.

flow that deformed the spherical shape of the double emulsion droplets into a bullet shape in the square section channel.

In summary, problems were observed with the method of photopolymerizing TMPTA double emulsion droplets with only external UV irradiation striking the top of the droplets when they flow in a square section channel. Many factors affect the shape of double emulsion droplets in pressure-driven microfluidic flow, including channel geometry, the inner and outer droplet diameter ratio, the viscosity ratio of involved phases, and the capillary number of the system [68]. Although the sphericity and concentricity of droplets can be improved by tuning the input parameters to specific values, shape deformation still persists due to the density mismatch of water and oil, which causes the droplets to sink to the bottom of the flow by gravity. In addition, UV irradiation is difficult to regulate, and so the drawbacks of photopolymerization cannot be avoided. Both the yield rate and the monodispersity of intact capsules can be very low. An alternative experiment setup was therefore proposed in an effort to improve photopolymerization performance.

3.4.2.2 Photopolymerization in straight circular section tubing

The double emulsion droplets were photopolymerized when flowing in circular section tubing (Figure 3.11). This method provides several flexibilities in relation to (1) the flowing direction of double emulsion droplets, (2) the number and arrangement of the UV LEDs, and (3) the exposure time of TMPTA segments to UV irradiation.

Flow direction

The photopolymerization of double emulsion droplets in straight circular section tubing with a single UV LED was tested. The double emulsion droplets were sent to the UV irradiation area from different directions by changing the tubing position (horizontal, vertical upward and vertical downward). When the droplets flowed in the vertical direction, they moved along the centerline of the tubing without

touching the wall, in contrast with the droplets moving in the horizontal direction. This solved the density mismatch issues of the water/TMPTA/oil double emulsions. Furthermore, the additional mineral oil through the bottom inlet was injected into the main flow at different flow rates (from 10ml/hour to 80ml/hour) for each flow direction. The results indicate that when the double emulsion droplets flowed vertically upward at a moderate continuous phase flow rate (from 30ml/hour to 50ml/hour), the attained microcapsules assumed a spherical shape with relatively good monodispersity (Figure 3.11 C, D, E). The sphericity of the TMPTA microcapsules can reach up to 99%, which is close to the ICF target specification

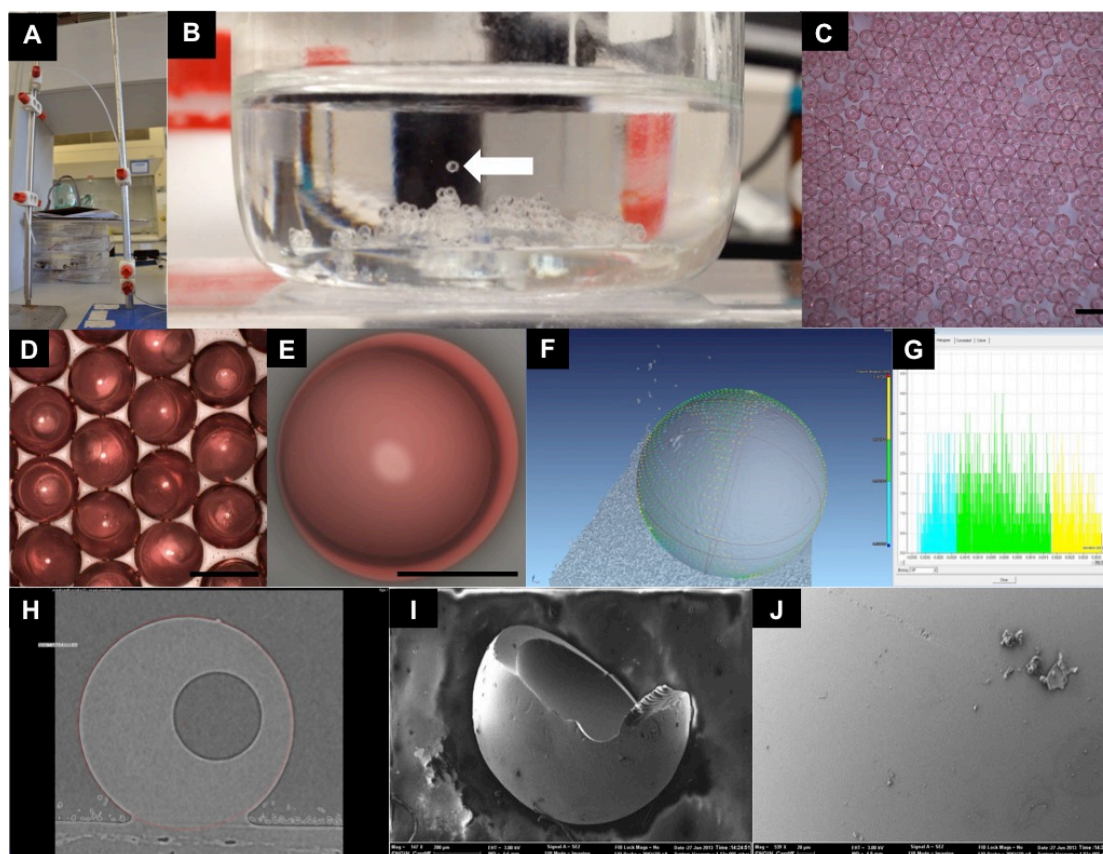


Figure 3.11 Photopolymerization of water/TMPTA/mineral oil double emulsion droplets in straight tubing with single UV LED. **A.** Photograph of the experimental setup. **B.** Solid TMPTA microcapsules were collected in a glass beaker filled with mineral oil. **C, D.** Monodispersed TMPTA microcapsules. Scale bars are 1 mm. **E.** Photograph of water core offsetting in spherical TMPTA microcapsules. Scale bar is 500 microns. **F-H.** X-ray tomography scans of a TMPTA microcapsule. **F, G.** Fitpoint deviation measurement of sample target showing deviation ($\pm 7\mu\text{m}$) around mean diameter of 1.44mm, equating to $\sim 99\%$ sphericity. **H.** X-ray tomography scan of water core offset. **I, J.** SEM images of a sample TMPTA microcapsule. **I.** Cracked TMPTA microcapsule. **J.** Surface of the shell.

(Figure 3.11 F, G). The yield rate of intact microcapsules from this group reached 100%, whereas the yields for the other groups are failed, even with the same input parameters. However, the offsetting of water core still occurred (Figure 3.11 H) [69]. This disadvantage limits the formation of thin-shell microcapsules with uniform shell thickness. If the W/P input ratio is increased, double emulsion droplets with a relatively large water core are formed, and the cured microcapsules undergo the “circular window” shell disruption as a consequence.

Arrangement of UV LEDs and the UV curing chambers

To attain a uniform, thin shell thickness, the double emulsion droplets were photopolymerized with uniform UV irradiation, which is achieved by the geometrical arrangement of LEDs, when they flowed in the straight tubing in the vertical upward direction. This was achieved by the arrangement of several UV LEDs around the tubing (Figure 3.12 A-C). UV curing chambers were manufactured to hold the LEDs at fixed positions. Control experiments were conducted to investigate the influences of different UV irradiation methods on the shape of the microcapsules. The results indicate that with evenly distributed UV irradiation, the concentricity of the solid TMPTA shells can be improved (Figure 3.12 D-L). Spherical shell deformation was found in the microcapsules cured with three UV LEDs placed in an equilateral triangle layout. This deformation can be reduced to some extent by polymerizing the droplets with four UV LEDs placed in a square layout (Figure 3.13). The water core did not leak out from the TMPTA phase during photopolymerization, and so the formation of bucket-shaped microparticles (which can arise in the previously mentioned methods) was prevented, even if the average shell thickness for intact TMPTA microcapsules was reduced to 60 microns (Figure 3.13 E and F). Figure 3.14 shows the concentricity and sphericity of 50 solid TMPTA microcapsules, which

were randomly picked from a group of samples that had been polymerized with four UV LEDs.

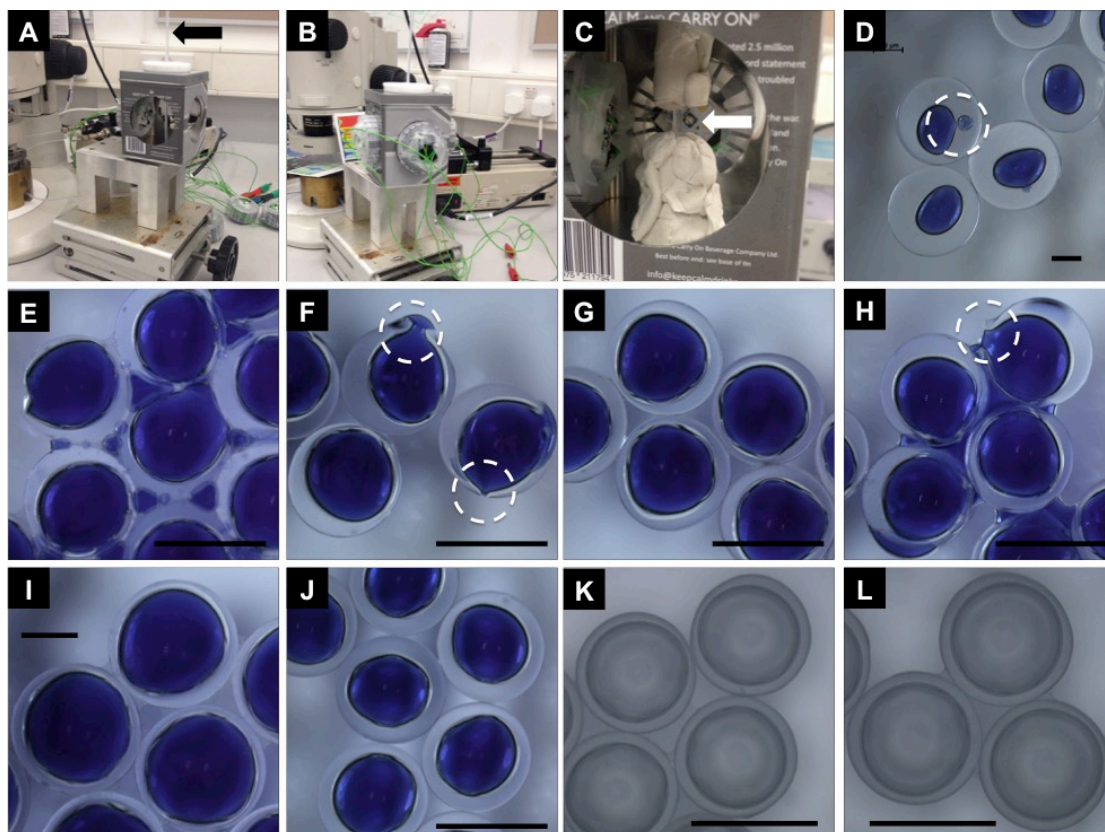


Figure 3.12 Photopolymerization of water/TMPTA/mineral oil double emulsion droplets in straight tubing with multiple UV LEDs. A-C. Photographs of the experimental setup. In A, the black arrow shows the straight outlet tubing in which the solid microcapsules flowed upwards. The chamber can hold up to four UV LEDs. In C, white plasticine was used to confine the UV irradiation area. D-L. Photographs of cured TMPTA microparticles with different number and arrangement of UV LEDs. All the other experiment setups were same. **D, E.** Photopolymerization via one UV LED. D. Small water core. The white circle indicated that the stress of polymerization broke up the water core. E. Large water core. The water leaked out from the microcapsule as the open window on the surface. **F, G.** Photopolymerization with two UV LEDs. F. The two LEDs were placed in the opposite position. White circles indicated the leakage of water core. G. The two LEDs were placed in the neighbor position with right angle. **H.** Photopolymerization with three UV LEDs. **I-L.** Photopolymerization with four UV LEDs. The results indicated that evenly UV irradiation improved the quality of microcapsules. Scale bar: D, 150 micron. E-L, 1mm.

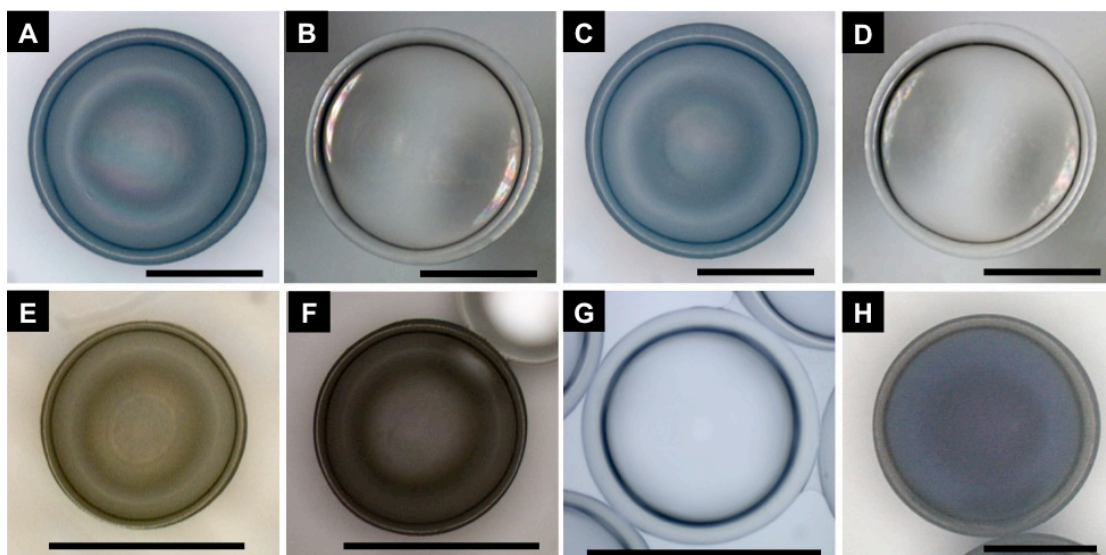


Figure 3.13 Photographs of solid TMPTA microcapsules produced by photopolymerization with four UV LEDs placed in the devised UV LED chamber. A-D are from the same experiment when the flow rates combination was 0.6/0.4/2.0/50.0 ml/hour for water phase/TMPTA phase/mineral oil phase/additional mineral oil phase. The scale bars are 500 microns. B and D are dark field images. Others are bright field images. E, F. The flow rates combination for this experiment was 0.5/0.2/0.8/50.0 ml/hour. The average shell thickness of microcapsules is 60 microns. The scale bars are 1mm. G. The flow rates combination for this experiment was 0.6/0.6/3.0/50.0 ml/hour. The concentricity of the capsule is 99.63%. The scale bar is 1mm. H. Different from other samples photopolymerized by continuous UV irradiation, this microcapsule was photopolymerized by 30ms UV irradiation in related experiment. The scale bar is 500 microns.

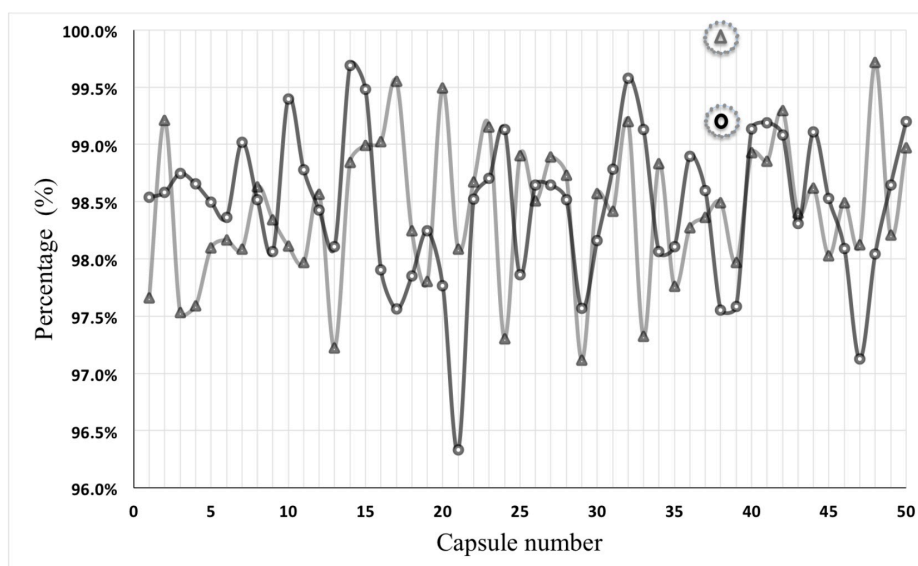


Figure 3.14 Sphericity (circles) and concentricity (triangles) of individual target shells. Capsule number does not imply the sequence production of shells. Dotted circles denotes minimum specification levels (%s) for use in an IFE reactor. Average sphericity is 98.43% with a 0.68% standard deviation. Best is 99.69%. Average concentricity is 98.44% with a 0.62% standard deviation. Best is 99.72 %. This group of samples has an average diameter $892.52\mu\text{m}$ with a $7.52\mu\text{m}$ standard deviation, and average shell thickness is $65.23\mu\text{m}$ with a $4.42\mu\text{m}$ standard deviation. The yield rate of intact capsule is 100%.

In addition, the relationship between UV exposure duration and the shell characteristics was investigated using a microprocessor (manufactured by Mr. Jack Lindley-Start) that could detect the double emulsion droplets in the flow using transducers. Whenever a droplet was detected, the UV LEDs were switched on for a short duration by the microprocessor. Four groups of experiment were conducted, and the concentricity and sphericity of attained microcapsules are shown in Table 3. From the results, it is evident that when the exposure time was changed from 0.01s to 0.03s, both the sphericity and concentricity of the shells improved. The conversion rate of polymerization was tested with Fourier transform infrared spectroscopy (FTIR) (Figure 3.15). These results indicate the possibility of photopolymerizing water/TMPTA/oil double emulsion droplets by pulsing the UV light for 30ms. This approach could lead to further reductions in energy consumption, as well as further optimization of the photopolymerization process for polymeric microcapsules fabrication.

Table 3. Calculated concentricity and sphericity values of microcapsules cured with diverse UV exposure time.

<i>Exposure time (second)</i>	<i>Concentricity</i>	<i>Sphericity</i>
<i>0.01</i>	<i>91.14%</i>	<i>58.69%</i>
<i>0.015</i>	<i>96.28%</i>	<i>83.53%</i>
<i>0.02</i>	<i>98.14%</i>	<i>89.18%</i>
<i>0.03</i>	<i>99.31%</i>	<i>98.83%</i>

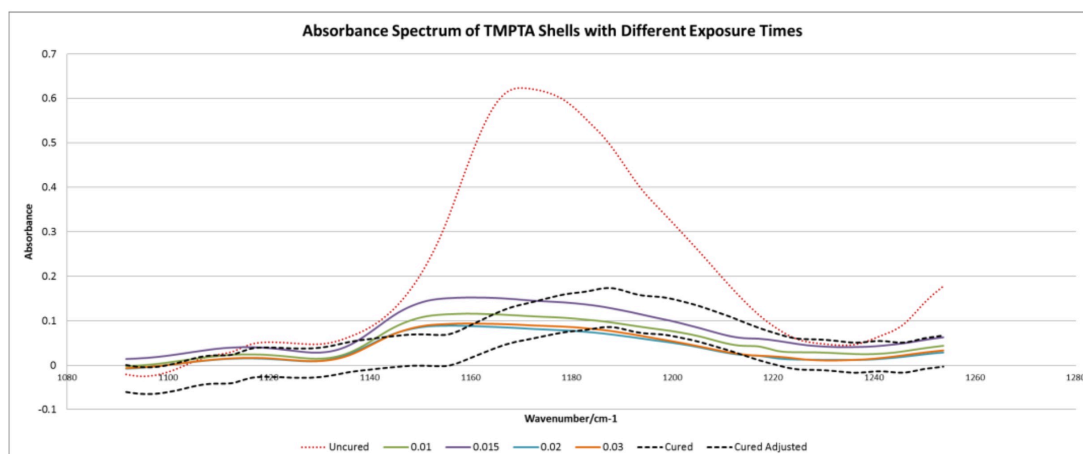


Figure 3.15 FTIR absorbance spectra for the microcapsules with different UV irradiation times. Partially cured samples appear in the area between the uncured sample (dotted red) and the cured sample (dotted black). Note that all the samples appear within the banding of the accuracy of the system (upper and lower dotted black), implying that they are all fully cured. The offset in tops of the peaks could be caused by the scans being random on different days and the calibration of the spectrometer changing.

3.4.3 MCNT-TMPTA nanocomposite

In inertial confinement fusion, cryogenic (18K) targets shells were to be fired into the reactor core at $\sim 1000\text{m/s}$, over 5m in a background temperature of $\sim 1000\text{K}$. In order to improve the Young's Modulus of the polymerized TMPTA, quantities (0.1% to 1.0%) of multi-walled carbon nanotubes were ultrasonically homogenized with the uncured monomer, and then polymerized. However, such additions appeared to render a resulting hybrid material with a Young's modulus that was $\sim 50\%$ lower than that of the raw TMPTA (Table 4). However, when carboxylate MCNTs were salinized (as previous method described back in sub-section 3.4.4) and then ultrasonically blended with the uncured TMPTA, the Young's Modulus of the resultant hybrid material was 32% higher (Table 4). The MWCNTs were found to be finely distributed within the photopolymerized TMPTA (Figure 3.16 A and B). However, this dispersion was heavily dependent upon the time interval between homogenization and photopolymerization. The energy dispersive X-Ray analysis of

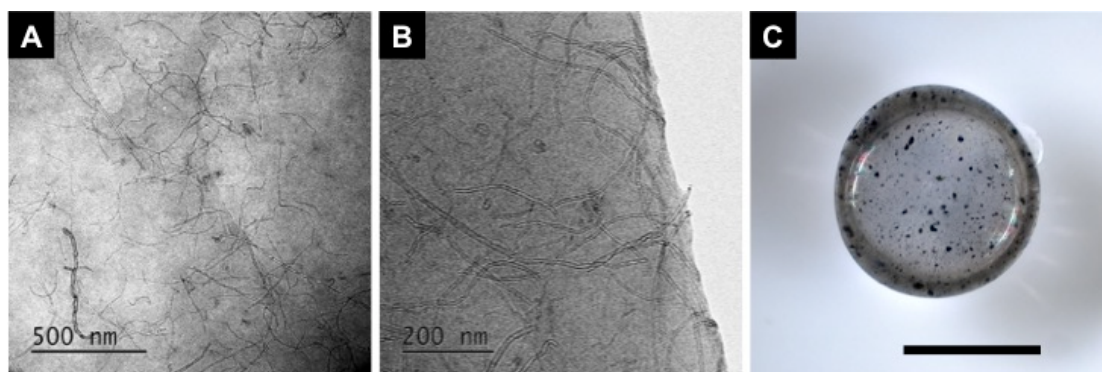


Figure 3.16 Photopolymerization of functionalized MCNT-TMPTA. **A.** The TEM images of functionalized MCNT dispersion in solid TMPTA. **B** indicates the edge of the TMPTA sample. **C.** Solid functionalized MCNT-TMPTA microcapsules. The black dots on the surface are MCNT aggregation. The scale bar is 1mm.

the MCNT-TMPTA is shown in Figure 3.17, whereby the Si-C bonds in the salinized MCNT are shown in the same high-density areas as those detected for carbon and silicon (Figure 3.17 B-D). The functionalized MCNT-TMPTA was used to fabricate microcapsules (Figure 3.16 C), and clumps of MCNT were found in the polymer shell. The origin of this aggregation needs to be further investigated in an effort to

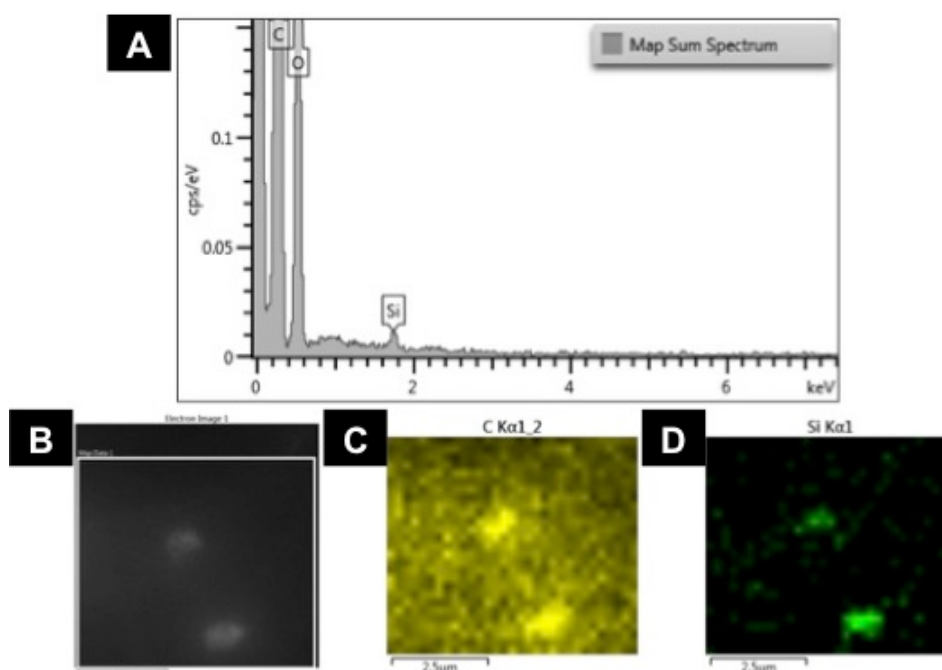


Figure 3.17 Energy-dispersive X-ray spectroscopy of cured functionalized MCNT-TMPTA sample. **A.** EDX spectrum of the cured sample. **B.** Electron image of a high-density area. **C.** Carbon detection image of the same area as B. **D.** Si detection image of the same area as B.

determine whether they exist in the solution, or are induced by photopolymerization kinetics.

Table 4. The Young's Modulus of photopolymerized polymer with ultrasonically mixed multi-walled Carbon nanotubes, with and without functional groups.

TMPTA	TMPTA+0.1% MWCNTs	TMPTA+0.1%functionalized MWCNTs
1260MPa	627MPa	1663MPa

3.5 Conclusion

In this chapter, an approach for the production of solid TMPTA microcapsules on a planar microfluidic device for ICF target fabrication was demonstrated. The experimentation was divided into two sets: (1) formation of monodispersed water/TMPTA/oil double emulsion droplets; and, (2) on-chip rapid photoinitiated polymerization, with modifications of the microcapsule characteristics.

The double emulsion was generated on PTFE microfluidic chips by the two-step method, and the monodispersity of attained droplets were improved by the removal of satellite droplets through the utilization of the bat-wing junction. In addition, an additional continuous phase inlet was employed to increase the distance between the adjacent droplets. These features helped to prevent the coalescing of double emulsion droplets during flow in the microfluidic channels, and enabled the generation of double emulsion droplets at a controllable rate up to 20Hz, which may be potential useful in a single ICF reactor in the future.

The impact of photopolymerization kinetics on the shape of the TMPTA microcapsules was also studied. It was found that when the water/TMPTA/oil double emulsion droplets flowed upwards in the centerline of a circular capillary and were cured by evenly distributed UV irradiations (minimum exposure time 30 ms), the resulting shells possessed both good average sphericity and concentricity (~98.5%,

best sphericity=99.69% and best concentricity=99.72%). The process was found to be highly reproducible with a 100% intact capsule yield rate, and it was possible to produce monodispersed microcapsules with controllable (from 60 μm to 100 μm), uniform shell thicknesses. By contrast, if photopolymerization is either undertaken in a square section channel or triggered by uneven UV irradiation, it is difficult to obtain intact solid capsules due to the polymerization shrinkage and stress.

Furthermore, a photo-curable TMPTA-MCNT nanocomposite with fine MCNT dispersion was synthesized. The Young's module of the thin fibers formed from the functionalized TMPTA solution was higher than those formed from neat TMPTA (up to 50%). This composite could be used to generate the double emulsions and produce intact solid microcapsules using the same process.

In view of the finding from this study, it is recommended that future studies should be focused on (1) the formation of foam TMPTA-MCNT shells, (2) the development of flexible microfluidic devices *via* 3D printing technology for ICF target fabrication, and (3) the on-chip inner phase solvent exchange and fuel injection of solid microcapsules in a cryogenic environment.

References:

1. Hoffert, M. I., Caldeira, K., Benford, G., Criswell, D. R., Green, C., Herzog, H., Jain, A. K., Kheshgi, H. S., Lackner, K. S., Lewis, J. S., Lightfoot, H. D., Manheimer, W., Mankins, J. C., Mauel, M. E., Perkins, L. J., Schlesinger, M. E., Volk, T., and Wigley, T. M. L., "Advanced technology paths to global climate stability: energy for a greenhouse planet," *Science*, vol. 298, no. 5595, pp. 981-987, 2002.
2. JET Team, "Fusion energy production from a deuterium-tritium plasma in the JET tokamak," *Nuclear Fusion*, vol. 32, no. 2, p. 187, 1992.
3. Nuckolls, J., and Wood, L., "Laser compression of matter to super-high densities: Thermonuclear (ctr)," *Nature*, vol. 239, p. 139, 1972.
4. Nuckolls, J. H., "The feasibility of inertial-confinement fusion," *Physics Today*, vol. 35, no. 9, pp. 24-31, 2008.
5. Key, M. H., "Fast track to fusion energy," *Nature*, vol. 412, no. 6849, pp. 775-776, 2001.
6. Moses, E. I., "The national ignition facility (NIF): a path to fusion energy," *Energy Conversion and Management*, vol. 49, no. 7, pp. 1795-1802, 2008.
7. Bondarenko, B. D., "Role played by OA Lavrent'ev in the formulation of the problem and the initiation of research into controlled nuclear fusion in the USSR," *Physics-Uspexhi*, vol. 44, no. 8, pp. 844-851, 2001.
8. Rebut, P. H., Bickerton, R. J., and Keen, B. E., "The Joint European Torus: installation, first results and prospects," *Nuclear Fusion*, vol. 25, no. 9, p. 1011, 1985.
9. EFDA, *European Fusion Development Agreement 2006 - The ITER Project*, accessed September 05, 2015, http://web.archive.org/web/20060820080541/http://www.efda.org/the_iter_project/organisation.htm.
10. Degnan, J. H., Alme, M. L., Austin, B. S., Beason, J. D., Coffey, S.K., Gale, D. G., Graham, J. D., Havranek, J. J., Hussey, T. W. Kiuttu, G. F., Kreh, B. B., Lehr, F. M., Lewis, R. A., Lileikis, D. E., Morgan, D., Outten, C. A., Peterkin, R. E., "Compression of plasma to megabar range using imploding liner," *Physical Review Letters*, vol. 82, no. 13, p. 2681, 1999.
11. Moses, E. I., Miller, G. H., and Wuest, C. R., "The national ignition facility: enabling fusion ignition for the 21st century," *Nuclear Fusion*, vol. 44, no. 2, pp. 228-238, 2004.
12. Miller, G. H., Moses, E. I., and Wuest, C. R., "The national ignition facility," *Optical Engineering*, vol. 43, no. 12, pp. 2841-2853, 2004.
13. Lindl, J., "Development of the indirect-drive approach to inertial confinement fusion and the target physics basis for ignition and gain," *Physics of Plasmas* (1994-present), vol. 2, no. 11, pp. 3933-4024, 1995.
14. Lindl, J. D., Amendt, P., Berger, R. L., Glendinning, S. G., Glenzer, S. H., Haan, S. W., Kauffman, R. L., Landen, O. L., and Suter, L. J., "The physics basis for ignition using indirect-drive targets on the National Ignition Facility," *Physics of Plasmas* (1994-present), vol. 11, no. 2, pp. 339-491, 2004.
15. Hager, J., "Rayleigh-taylor experiments in materials and conditions relevant to ignition in inertial confinement fusion," Unpublished, January 2012.
16. Frederick, C. A., Paguio, R. R., Nikroo, A., Hund, J. H., Acennas, O., and Thi, M., "Controlling the pore size and gelation time of resorcinol formaldehyde

- foam for fabrication of direct drive targets for ICF experiments,” *Fusion Science and Technology*, vol. 49, no. 4, pp. 657-662, 2006.
17. Paguio, R. R., Takagi, M., Thi, M., Hund, J. F., Nikroo, A., Paguio, S., Luo, R., Greenwood, A. L., Acenas, O., and Chowdhury, S., “Improving the wall uniformity of resorcinol formaldehyde foam shells by modifying emulsion components,” *Fusion Science and Technology*, vol. 51, no. 4, pp. 682-687, 2007.
 18. Schultz, K. R., *Inertial Fusion Target Development*, In: *Fusion Engineering*, 16th IEEE/NPSS Symposium (Vol. 1, pp. 116-123), 1995, IEEE.
 19. Youngs, D. L., “Numerical simulation of turbulent mixing by Rayleigh-Taylor instability,” *Physica D: Nonlinear Phenomena*, vol. 12, no. 1, pp. 32-44, 1984.
 20. Goodin, D. T., Alexander, N. B., Besenbruch, G. E., Bozek, A. S., Brown, L. C., Carlson, L. C., Flint, G. W., Goodman, P., Kilkenny, J. D., Maksareekul, W., McQuillan, B. W., Nikroo, A., Paguio, R. R., Petzoldt, R. W., Raffray, R., Schroen, D. G., Sheliak, J. D., Spalding, J., Streit, J. E., Tillack, M. S., and Vermillion, B. A., “Developing a commercial production process for 500 000 targets per day: a key challenge for inertial fusion energy,” *Physics of Plasmas* (1994-present), vol. 13, no. 5, pp. 056305, 2006.
 21. Friedman, L. S., “Fusion energy with lasers, direct drive targets, and dry wall chambers,” *Nuclear Fusion*, vol. 43, no. 12, p. 1693, 2003.
 22. Campbell, J. H., Grens, J. Z., and Poco, J. F., *Preparation and Properties of Hollow Glass Microspheres*, UCRL-53516, Livermore: Lawrence Livermore National Laboratory, 1983, p. 8.
 23. Qiu, L. H., Fu, Y. B., Tang, Y. J., Wei, Y., Zheng, Y. M., Shi, T., and Yao, S. J., “Hollow glass microsphere production for laser direct-driven fusion targets on Shen Guang II,” *Science in China Series A: Mathematics*, vol. 45, no. 3, pp. 371-377, 2002.
 24. Nikroo, A., and Steinman, D. A., “Thin sputtered glass as a permeation barrier for plasma polymer shells,” *Fusion Technology-Illinois*, vol. 35, no. 2, pp. 212-215, 1999.
 25. Hoppe, M. L., “Large glass shells from GDP shells,” *Fusion Science and Technology*, vol. 38, no. 1, pp. 42-45, 2000.
 26. Qi, X. B., Tang, Y. J., Li, B., Chen, S. F., Shi, T., Zhang, Z. W., Lin, B., and Chu, Q. M., “Fabrication of hollow glass microspheres used for ICF targets by dried-gel method,” *Qiangjiguang Yu Lizishu (High Power Laser and Particle Beams)*, vol. 18, no. 1, pp. 55-60, 2006.
 27. Cook, B., Letts, S., Nikroo, A., Nobile, A., McElfresh, M. I. K. E., Cooley, J., and Alexander, D., Preliminary evaluation of techniques to fabricate beryllium polyimide and Gedopod CH/CD ablator materials,” *Lawrence Livermore National Laboratory Report UCRL_TR-208476*, 2004.
 28. Hund, J. F., Paguio, R. R., Frederick, C. A., Nikroo, A., and Thi, M., Silica, “Metal oxide, and doped aerogel development for target applications,” *Fusion Science and Technology*, vol. 49, no. 4, pp. 669-675, 2006.
 29. Biener, J., Ho, D. D., Wild, C., Woerner, E., Biener, M. M., Eldasher, B. S., and Hamza, A. V., “Diamond spheres for inertial confinement fusion,” *Nuclear Fusion*, vol. 49, no. 11, pp. 1120-1121.
 30. Paguio, R. R., Frederick, C. A., and Hund, J. F. “Development of a production process for fabricating low and high density resorcinol formaldehyde foam shells for direct drive experiments,” *GA-A25242*, 2005.

31. Chen, C., Norimatsu, T., Takagi, M., Katayama, H., Yamanaka, T., and Nakai, S., "Development of foam shells for cryogenic laser fusion target," *Journal of Vacuum Science & Technology A*, vol. 9, no. 2, pp. 340-344, 1991.
32. Cook, R., *Production of hollow microspheres for inertial confinement fusion experiments*, In: Materials Research Society Symposia Proceedings 372, 1995, pp. 101-112.
33. Moreau, L., Levassort, C., Blondel, B., Nonancourt, C. D., Croix, C., Thibonnet, J., and Balland-Longeau, A., "Recent advances in development of materials for laser target," *Laser and Particle Beams*, vol. 27, no. 4, pp. 537-544, 2009.
34. Takagi, M., Norimatsu, T., Yamanaka, T., Nakai, S., "Development of deuterated polystyrene shells for laser fusion by means of a density-matched emulsion method," *Journal of Vacuum Science & Technology A*, vol. 9, no. 4, pp. 2145-2148, 1991.
35. Letts, S. A., Fearon, E. M., Buckley, S. R., Saculla, M. D., Allison, L.M., Cook, R.C., *Preparation of hollow shell ICF targets using a depolymerizing mandrel*, In: Materials Research Society Symposia Proceedings 372, 1995, pp. 125-130.
36. Takagi, M., Ishihara, M., Norimatsu, T., Yamanaka, T., Izawa, Y., and Nakai, S., "Development of foam shell with plastic ablator for cryogenic laser fusion target," *Journal of Vacuum Science & Technology A*, vol. 11, no. 5, pp. 2837-2845, 1993.
37. Lattaud, C., "Synthesis of low density foam shells for inertial confinement fusion experiments," PhD Dissertation, Université de Bourgogne, 2011.
38. Guillot, L., Vedrenne, P., and Etheve, J., "Procédé et dispositif de fabrication de billes ou de ballons en mousse polymère," 2004.
39. Paguio, R. R., "Fabrication of modified density and tin doped RF foam shells and beads for direct drive experiments," *Polymeric Materials: Science & Engineering*, vol. 95, pp. 872-874, 2006.
40. Takagi, M., Cook, R., Stephens R, Gibson, J., and Paguio, S., "Decreasing out-of-round in poly (α -methylstyrene) mandrels by increasing interfacial tension," *Fusion Science and Technology*, vol. 38, no. 1, pp. 46-49, 2000.
41. Abate, A. R., Thiele, J., and Weitz, D. A., "One-step formation of multiple emulsions in microfluidics," *Lab On A Chip*, vol. 11, no. 2, pp. 253-258, 2011.
42. Chen, C., Cook, R. C., Haendler, B. L., Hair, L. M., Kong, F. M., and Letts, S. A., "Low-density hydrocarbon Foams for laser fusion targets," *Progress Report - 1986*, pp. 1-23, 1987.
43. Randall, G., "Continuous dielectrophoresis centering of compound droplets," American Physical Society, March 2012 Meeting.
44. Stephen, O. L., "Fabrication of low-density foam shells from resorcinol-formaldehyde aerogel," *Journal of Applied Polymer Science*, vol. 65, no. 11, pp. 2111-2122, 1997.
45. Wang, W. Q., "On-chip double emulsion droplet assembly using electrowetting - on - dielectric and dielectrophoresis," PhD Dissertation, University of Rochester, 2012.
46. Bei, Z. M., "Dielectrophoresis-based double-emulsion droplet centering for concentric laser target foam shells," PhD Dissertation, University of Rochester, 2010.

47. Gao, J. Y., Ge, L. Q., Li, B., Shi, Z., Chen, S. F., Zhao, X. W., and Gu, Z. Z., "Fabrication of polyacrylonitrile microcapsules for ICF targets," *Fusion Science and Technology*, vol. 61, no. 4, pp. 275-281, 2012.
48. Paguio, R. R., Nikroo, A., Takagi, M., and Acenas, O., "Fabrication and overcoating of divinylbenzene foam shells using dual initiators," *Journal of Applied Polymer Science*, vol. 101, no. 4, pp. 2523-2529, 2006.
49. Shao, T., Feng, X., Jin, Y., and Cheng Y., "Controlled production of double emulsions in dual-coaxial capillaries device for millimeter-scale hollow polymer spheres," *Chemical Engineering Science*, vol. 104, pp. 55-63, 2013.
50. Decker, C., "Polymerisation sous rayonnement UV," *Techniques de l'ingénieur*, pp. 1-14.
51. Odian, G., *Radical Chain Polymerization*, In *Principles of Polymerization*, 4th edition, Wiley-Interscience, Hoboken, NJ, pp. 198-349.
52. Chern, C. S., *Introduction*, In *Principles and Applications of Emulsion Polymerization*, John Wiley & Sons, 2008, pp. 1-22.
53. Herk, A.V., *Introduction to Radical (co)Polymerisation*, In *Chemistry and Technology of Emulsion Polymerisation*, A.V. Herk, Editor, Blackwell Publishing, 2005, pp. 25-45.
54. North, A.M., "Reactivity, mechanism, and structure in polymer chemistry," *Wiley-Interscience*, 1974.
55. Mark, A., *Polymer Science Dictionary*, New York: Elsevier Applied Science, 1989, p. 28.
56. Venhoven, B. A. M., De Gee, A. J., and Davidson, C. L., "Polymerization contraction and conversion of light-curing BisGMA-based methacrylate resins," *Biomaterials*, vol. 14, no. 11, pp. 871-875, 1993.
57. Park, J., Chang, J., Ferracane, J., and Lee, I. B., "How should composite be layered to reduce shrinkage stress: incremental or bulk filling?" *Dental Materials*, vol. 24, no. 11, pp. 1501-1505, 2008.
58. Kleverlaan, C. J., and Feilzer, A. J., "Polymerization shrinkage and contraction stress of dental resin composites," *Dental Materials*, vol. 21, no. 12, pp. 1150-1157, 2005.
59. Hoyle, C. E., Lee, T. Y., and Roper, T., "Thiol-enes: chemistry of the past with promise for the future," *Journal of Polymer Science Part A: Polymer Chemistry*, vol. 42, no. 21, pp. 5301-5338, 2004.
60. Carioscia, J. A., Lu, H., Stanbury, J. W., and Bowman, C. N., "Thiol-ene oligomers as dental restorative materials," *Dental Materials*, vol. 21, no. 12, pp. 1137-1143, 2005.
61. Senyurt, A. F., Wei, H., Hoyle, C. E., Piland, S. G., and Gould, T. E., "Ternary thiol-ene/acrylate photopolymers: effect of acrylate structure on mechanical properties," *Macromolecules*, vol. 40, no. 14, pp. 4901-4909, 2007.
62. Makino, M., Sugihara-seki, M., "Segregation of large and small droplets suspended in poiseuille flow," *Theoretical and Applied Mechanics Japan*, vol. 62, no. 0, pp. 69-78, 2014.
63. The, S. Y., Lin, R., Hung, L. H., and Lee, A. P., "Droplet microfluidics," *Lab On A Chip*, vol. 8, no. 2, pp. 198-220, 2008.
64. Stone, H. A., "Dynamics of drop deformation and breakup in viscous fluids," *Annual Review of Fluid Mechanics*, vol. 26, no. 1, pp. 65-102, 1994.
65. Tan, Y. C., and Lee, A. P., "Microfluidic separation of satellite droplets as the basis of a monodispersed micron and submicron emulsification system," *Lab On A Chip*, vol. 5, no. 10, pp. 1178-1183, 2005.

66. Kuriakose, S., and Dimitrakopoulos, P., “Deformation of an elastic capsule in a rectangular microfluidic channel,” *Soft Matter*, vol. 9, no. 16, pp. 4284-4296, 2013.
67. Boruah, N., and Dimitrakopoulos, P., “Motion and deformation of a droplet in a microfluidic cross-junction,” *Journal of Colloid and Interface Science*, vol. 453, pp. 216-225, 2015.
68. Chen, Y., Liu, X., and Zhao, Y., “Deformation dynamics of double emulsion droplet under shear,” *Applied Physics Letters*, vol. 106, no. 14, pp. 141601, 2015.
69. Ma, S., Sherwood, J. M., Huck, W. T. S., and Balabani, S., *Flow Pattern in Inner Cores of Double Emulsion Droplets*, Brunel University London, 2014.

CHAPTER IV.

Mouse Neuron Stem Cell Encapsulation in Alginate Microspheres *via* Droplet Microfluidics

4.1 Spinal cord injury

Spinal cord injury (SCI), involves the loss of motor coordination and of sensory or autonomic functions, with no natural regeneration after injury [1]. According to previously published data, the main cause of traumatic spinal cord injury is motor vehicle accidents; other prominent causes include physical violence, falls, and recreational activities [2]. The pathophysiology of SCI is complicated, but generally comprises two stages. The first stage, known as primary injury, is marked by damage to the central and peripheral nervous systems by traction and compression forces. The displacement of bone fragments and ligaments lead to the severing of blood vessels, disruption of axons, and damage to neural-cell membranes. As a consequence, systemic hypotension and ischaemia occurs, and toxic chemicals are released from disrupted neural membranes, from where there also occurs a migration of electrolytes. Those induce the death of neighboring cells and initiate secondary injury [3, 4]. The secondary injury lasts for days or weeks. One toxic chemical, glutamate, has a significantly negative impact on healthy neurons and oligodendrocytes [5, 6]. The existence of glutamate results in a highly disruptive process known as excitotoxicity. The affected cells receive calcium ions and cause a series of destructive events, including production of free radicals. The regional hypoperfusion extends from the grey matter to the white matter, and the unsevered axons become demyelinated [7]. Hence, the action potential along the axon is disturbed, and the conduction of impulses is blocked. The majority of trauma spinal-cord injuries results in lesions, both on the upper and lowers motor neurons. Due to the segmental demyelination, most of the axons cease to function, and only a few remain intact in the outer white matter. During this period, extensive cell death occurs in the cord.

Diagnosis of SCIs should include the assessment of a patient's mental status, cranial nerves, motor, sensory, and autonomic systems, coordination, and gait. Computed tomography or magnetic resonance imaging is used to image SCIs. Compared with radiography, computed tomography has the advantages of producing a better visual display of damaged soft-tissue and bone structures. Myelography is also used to detect abnormalities in the spinal canal [8, 9].

It is imperative to limit secondary injury as much as possible when treating spinal cord injuries. The primary approach is to remove the damaged bone, disk and ligament fragments, which will help to decompress the swollen cord. Animal tests have shown that an early surgical (6 to 8 hours) decompression leads to better SCI recovery [10, 11]. The utilization of the steroid methylprednisolone within 8 hours after injury was reported to reduce disability as it decreases swelling, inflammation, and free radical accumulation [12]. By contrast, surgical interventions conducted between 24 and 72 hours after an SCI injury are less successful, since most tissue damage has become irreversible during that time period [13-17]. In addition, chemical compounds that limit the impact of excess glutamate on cells can improve a patient's recovery from SCI.

Advanced therapeutic approaches to reduce paralysis have been developed for patients with spinal cord injuries. Functional electrical stimulation is useful for treating SCI when lower motor neurons and peripheral nerves are still intact. It restores sensation in the hands, which greatly benefits individuals who have become tetraplegic [18]. Computer-controlled, transcutaneous, reciprocal-pattern, electrical activation of leg muscles can be used for physical training and cardiovascular conditioning [19, 20]. Other options include tendon transfer, phrenic nerve

stimulation, adaptive equipment, and environmental control devices. These can maximize a patient's remaining functions and improve their quality of life.

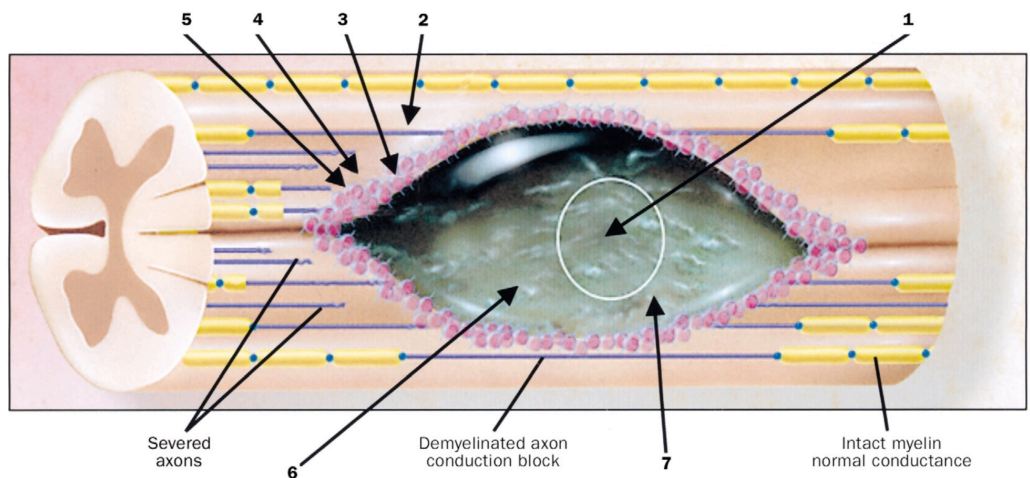


Figure 4.1 Schematic showing the sequence of interventions in the treatment of spinal-cord injury. Description of numbers in text [21].

Restorative treatments for SCI patients should be implemented in a stepwise manner, including limitation of cell death immediately after injury, promotion of cell regeneration, and replacement of lost cells. Each stage should concentrate on different targets and provide incremental benefits. As shown in Figure 4.1, the restoration of functions following SCI include (1) preventing the progression of secondary injury; (2) compensating demyelination; (3) removal the inhibition of regeneration; (4) promotion of axonal regeneration; (5) directing axons to their proper targets; (6) creation of bridges; and, (7) replacement of lost cells. Cell regeneration and replacement leads to the restoration of functions, and will be the pivotal goal of future SCI treatments. The cell regeneration requires the connection of existing neurons with newly formed neurons in an appropriate circuit. Additionally, proper electrical transmission is required, in which oligodendrocytes must myelinate large-calibre axons, where astrocytes must provide support [22]. Implanted central neuron system (CNS) stem cells can be differentiated to form new neurons and glial cells, which can replace those which were lost as a result of SCI. However, researchers are still trying

to devise a method for generating a sufficient supply of replacement cells *in vivo*. One possible avenue could be stem cell therapy.

4.2 Stem cell therapy

Embryonic stem cells (derived from the inner mass of blastocysts) and embryonic germ cells (derived from post-implantation embryos) are two forms of mammalian pluripotent stem cells that can differentiate into a range of tissue cells [23-26]. These cells retain their potential to differentiate along various tissue lineages after growth in culture, and this offers the prospect of developing novel cell transplantation therapies [27] (Figure 4.2).

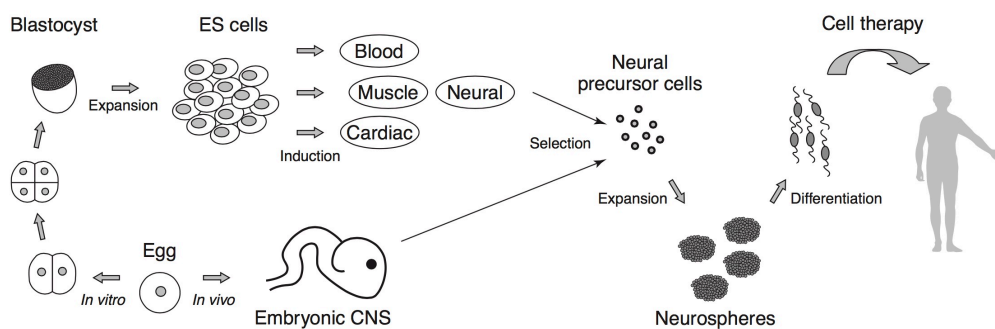


Figure 4.2 Stem-cell therapy for central neuron system disorders [53].

Neural stem cells (NSCs) have the potential to differentiate into three major kinds of CNS cells: neurons, astrocytes, and oligodendrocytes [28-32]. Recently, human neural stem cells have been successfully cloned [32] and multiplied *in vitro* [33, 34], and have been transplanted into foetal rodents' brains [35]. This indicates the potential of stem cell therapy to treat human neurological diseases induced by the loss of neurons and glial cells in the CNS, such as Parkinson's disease, Huntington's disease, amyotrophic lateral sclerosis, Alzheimer's disease, multiple sclerosis, stroke, and spinal cord injury (SCI).

In SCI treatment, axonal regeneration can be boosted using a range of cell types, including genetically modified fibroblasts, olfactory ensheathing cells, and

Schwann cells [36-40]. There has been extensive research into mimicking human SCI, and it has been found that the pathology of white matter is closely linked with the restoration of functions [41-43]. Several researchers have reported the improvement of injured spinal core functionality following the transplantation of various stem cells types, including ESCs, bone marrow MSCs, neural stem cells, and glia restricted precursor cells [40, 44-52].

However, there still remain several unresolved problems, such as the need for suitable cellular grafts and transplant mechanisms for a successful clinical application of stem cell therapy in SCI patients. One major issue is the massive death of stem cells following transplantation into damaged spinal cord tissue. This undesirable phenomenon arises due to the physical environment in the injured spinal cord tissue, which promotes apoptotic cell death. (Apoptosis is a highly regulated form of cell death involving both extrinsic and intrinsic cell death pathways) [54]. The overexpression of anti-apoptotic molecules (such as Bcl-xL) to NSCs *via* gene transfer can extend the survival of grafted stem cells *in vivo* [55]. In addition, the immortalized NSCs have the advantage of being more amenable to genetic manipulation, and their *in vivo* differentiation into neurons, astrocytes, and oligodendrocytes has been recorded, whereby they form synapses with other cells [29, 31, 56-58].

Nevertheless, the use for stem cell therapy in the treatment of human neurological diseases is restricted by the following problems: (1) earlier studies have shown that the long-term survival and phenotypic stability of newly differentiated neurons or glial cells from NSCs are unachievable [59]; (2) unpredictable interactions among grafted cells or with existing neurons have been observed [60]; and, (3) a

small number of NSCs might expand and form a tumor in the graft site following transplantation [61].

4.3 Cell encapsulation using microfluidics

The survival of transplanted stem cells *in vivo* is influenced by the pathological tissue environment, and by inflammatory and immune reactions [62]. After external stem cells are injected into the injured tissues, the host's immune system sends T-cells into the same region. T-cells release cytokine when they detect foreign substances in the body [63]. The increase of cytokine in the bloodstream triggers macrophages, which in turn will attack and destroy the transplanted stem cells. Only 5 to 10% of implanted stem cells survive this initial immune response. A diminished stem cell population results in a poor performance of stem cell therapy in the treatment of SCI.

Therefore, a cell transplantation strategy that prevents the body from destroying the implanted cells is required for the integration of neurons, and function restoration following SCI. One applicable method is the synthesis and transplantation of artificial tissues (containing stem cells) into the host's body. The tissues should be made from biocompatible and biodegradable materials such as hydrogel or polymer solution. The phase consolidation and the encapsulation processes must not place undue stress on the cells. The inner structure of resulting tissues should allow stem cell proliferation and differentiation. The degradation of the artificial tissue should be controlled at the right time scale for the new neuron network formation. In addition, the production of the degradation should be biocompatible and be metabolisable by the circulatory system [64].

As described in Chapter I, several studies have been reported using droplet microfluidics to encapsulate living cells in monodispersed microgels. Workman and

coworkers synthesized alginate microspheres for encapsulation of immortalized human cells using flow focusing devices [65]. Wieduwild and coworkers produced homogeneous and tunable hydrogel beads from peptide-polyethylene glycol conjugates and oligosaccharides encapsulating eGFP-secreting insect cells using T-shaped droplet forming junctions [66]. Yu and coworkers generate alginate beads encapsulating breast tumor cells. A continuous perfusion system was used to trap the gelled microgels in microsieve structures in which encapsulated cells performance proliferation *in vitro* [67].

The objective of this study was to develop a planar PTFE microfluidic device for the mass production of monodispersed microspheres for neural stem cell encapsulation. The microspheres were composed of sodium alginate, which is biocompatible and degradable, and has been shown to support the long-term stem cell viability *in vitro* by exhibiting appropriate proliferation without unexpected differentiation. The work presented here, is part of a greater research project on stem cell therapy for the treatment of spinal cord injury.

4.4 Experiment

4.4.1 Culture protocol for mouse neural stem cells

The culture medium recipe for mouse neural stem cells (shown as Table 5) was devised by Dr. Bangfu Zhu in the dentistry school at Cardiff University. The culture medium was stored in a refrigerator, and warmed up in a 37 degrees (centigrade) water bath for 5 minutes prior to use.

Table 5. Culture medium for mouse neural stem cell

<i>Ingredients</i>	<i>Volume (in every 50 ml)</i>
<i>DMEM/F12 (1:1) (Invitrogen, 31330-038)</i>	<i>48.5 ml</i>
<i>MEM NEAA (100X) (Invitrogen, 11140)</i>	<i>500 μl</i>
<i>FGF-basic Recombinant Human (Invitrogen, PHG0026)</i>	<i>20 ng/ml</i>
<i>EGF Recombinant Human (Invitrogen, PHG0311)</i>	<i>20 ng/ml</i>
<i>N2-Supplement (100X) (Invitrogen, 02048)</i>	<i>500 μl</i>
<i>PenStrep (100X) (Invitrogen, 15140)</i>	<i>500 μl</i>

4.4.2 Passage procedure

The neural stem cells (neurospheres, Figure 4.3A) were transferred into a 15ml tube and centrifuged at 1500 rpm for 5 minutes. The supernatant was removed from the tube, and 0.5 ml of Accutase (Sigma, A6964-100ML) was added to dissociate the spheres into single cells (Figure 4.3B) for 2 minutes (in a 37-degree (centigrade) water bath). 10 ml PBS was then added to dilute and stop the action of Accutase. The cells were re-centrifuged at 1200 rpm for 3 minutes, and the supernatant was then removed from the tube. The cells were re-suspended in 1 ml of

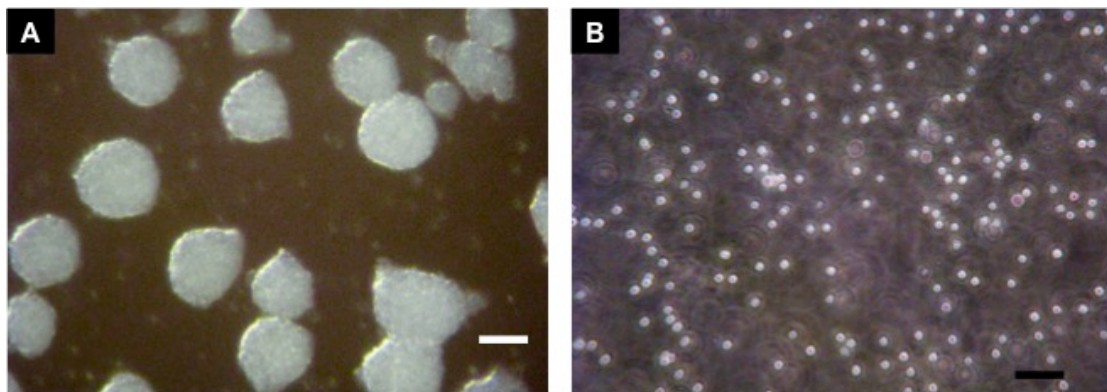


Figure 4.3 Mouse neuron stem cells *in vitro*. **A.** Neurospheres (Passage 13). Scale bar is 200 microns **B.** Single neuron stem cells, dissociated from P13 neurospheres. (Passage 14). Scale bar is 100 microns.

fresh medium by pipetting a few strokes, and then passed through a 40 μ m cell strainer to obtain single cells. The attained cells in suspension were seeded into a flask at a concentration of between 2×10^4 /ml and 5×10^4 /ml, and stored in an atmosphere of [5%CO₂/ 95% Air] at 37 degrees centigrade inside an incubator. A 100% medium change was performed every 3 days, and a cell passage was conducted every 5 or 6 days for the cells.

4.4.3 Microfluidic experiment

4.4.3.1 Solvent preparation

Inner phase: The inner phase is the culture medium with living cells that reached 90% confluence before being trypsinized. .

Middle phase: The middle phase was 3% alginate solution. 0.4g alginate powder was added into 20mL water and stirred at 50 degrees centigrade for 2 hours. Then, 0.15g CaCO₃ powder was added and the solution was stirred for another 2 hours. When the alginate solvent cooled down to room temperature, it was mixed with type I collagen and stored in ice to prevent gelation.

Continuous phase: Two types of oil phase were used in the experiment. One oil phase was pure mineral oil, which was used to shear off the discrete aqueous droplets. The other oil phase contained acetic acid, which reacted with CaCO₃, which in turn released Ca²⁺ ions to consolidate the sodium alginate molecules. Both the pure mineral oil and the mineral oil with acetic acid were filter-sterilized and degasified before being charged into the syringes.

4.4.3.2 Device assembly

The PTFE microfluidic chip, the PTFE film and the FEP tubing were washed with chloroform in a sonication bath for 2 minutes. All the stainless steel housing and

microfluidics parts were cleaned with ethanol and assembled in a fume cupboard. To avoid contamination, chloroform was continuously delivered to the assembled microfluidic system for 10 minutes, which was washed with ethanol for 10 minutes and then washed with PBS for 10 minutes in sequence.

4.4.4 Measurement

Optical images of mouse neural stem cells and the alginate microparticles were taken using a Nikon camera mounted on a light microscope (Nikon Eclipse TS100). The fluorescent images were taken using DeltaVision fluorescence microscope. The growth of the cell population was measured with MTT assays using Microplate autoreader, Bio-Tek, EL 311.

4.5 Result and discussion

4.5.1 Droplet formation

In this experiment, the monodispersed hydrogel microspheres were formed in a two-step mechanism. The innermost phase, the culture medium with living cells, was delivered to the middle of a cross-shaped junction on the planar PTFE microfluidic chip. Two streams of alginate precursor were introduced from the sides, dynamically focusing the inner phase and forming a sheath flow (Figure 4.4A). By

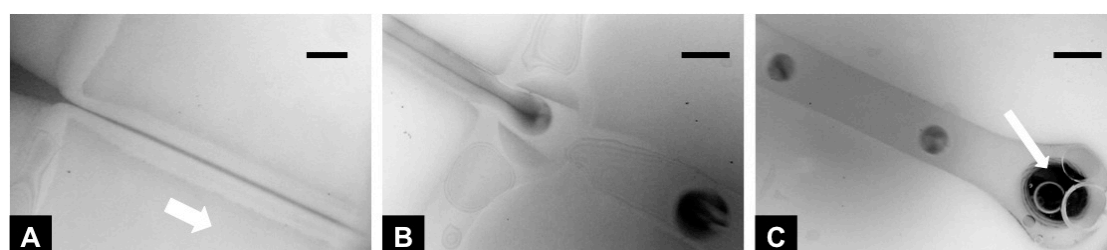


Figure 4.4 Alginate microspheres formation. **A.** Sheath flow was formed at the first flow focusing junction on our planar PTFE microfluidic chip. The dark line was culture medium and the light ones were 3% alginate solution. The white arrow indicates the flow direction. The scale bar is 600 microns. **B.** The alginate droplet was sheared off at the batwing junction. The scale bar is 1.2 mm. **C.** The alginate microspheres flowed through outlet of the chip. The scale bar is 1.2 mm.

tuning the input flow rate, the volume ratio of those two phases can be regulated, and the cell density and concentration of nutrients on-chip can be adjusted. This also controls the amount of the alginate in the mixture, which determines the structure and pores size of the resulting microgels. These properties, in turn, influence the internal mechanical stress on the microspheres, and affect the reliability of the encapsulated cells.

The sheath flow (which was composed of culture medium and alginate) was segmented by a continuous pure mineral oil phase at the second flow-focusing junction (Figure 4.3B). The droplet size and shear-off frequency were controlled by the inflow parameters. Uniform alginate segments were formed *via* the dripping regime with a constant distance between the adjacent droplets. (The formation of droplets in jetting regimes has a large size distribution, and end up coalescing due to their various linear velocities under Poiseuille flow.) In addition, the width of the channel beyond the droplet-forming junctions should not exceed 150% of the droplet diameter; this helps to maintain the flow of alginate droplets in the centerline of the continuous phase stream.

4.5.2 On-chip gelation of the alginate microgels

As previously described, the alginate molecule chains were cross-linked together in the presence of Ca^{2+} , to form a hydrogel matrix for the encapsulated cells. Two methods have been developed for the gelation of the alginate microspheres in microfluidics. One is direct coalescence of an alginate droplet and another water droplet saturated with calcium chloride within a spindle-shaped groove engraved in the channel. As soon as the two droplets merge together, the alginate chains sequester the Ca^{2+} ions and became consolidated. This requires precise control of the synchronized formation and migration of the various droplets. The other applicable

method is the addition of nanocrystalline calcium carbonate salt to the alginate phase. The insoluble CaCO_3 salt is immobilized in the alginate phase, and it releases calcium ions into the local vicinity when it reacts with H^+ . The reaction between H^+ and CaCO_3 is rapid and will result in fast gelation, which might induce an unexpected gelation of the alginate and occlude the microfluidic channel. Hence, this method requires a rigorous control of the H^+ ions (both its rate of addition to the main stream, and its concentration) in the solvent. This can be achieved by adding mineral oil (pre-mixed with acetic acid) into the channel following alginate segmentation. The approaches in which the extra inlet may deliver mineral oil (containing acetic acid) are shown in Figure 4.5. This shows a bottom inlet in the straight channel beyond the droplet-forming junction. The step structure is used to smoothen the orthogonal flows, which mitigates the growth of local pressure zones so that droplet disruption can be avoided. This microfluidic circuit layout has been used to produce alginate microsphere-encapsulated mouse neuron stem cells. The process is consistent and reproducible, and the fabrication of gelled alginate beads continues until the precursor solutions run out (after approximately one hour) The attained microgels have good monodispersity (as described back in Chapter II), and their diameters are tunable, from a few hundred microns up to 1.5 millimeters (minimum diameter is 400 microns). Another approach for alginate segments gelation involves using a lateral channel (Figure 4.5D-F) to deliver acetic acid-bearing mineral oil. A different droplet-forming junction is employed to produce monodispersed alginate droplets with a minimum diameter of 70 microns, which might be useful for producing some cell encapsulation. The microspheres can travel either *via* the top channel or the bottom channel, and they approach the acid oil phase at a set combination of flow rates. This microfluidic chip was also utilized to produce spherical PEGDA microparticles, non-

spherical PEGDA microparticles, and PEGDA microcapsules with photoinitiated polymerization (Figure 4.6C). There will be further investigation into living cell

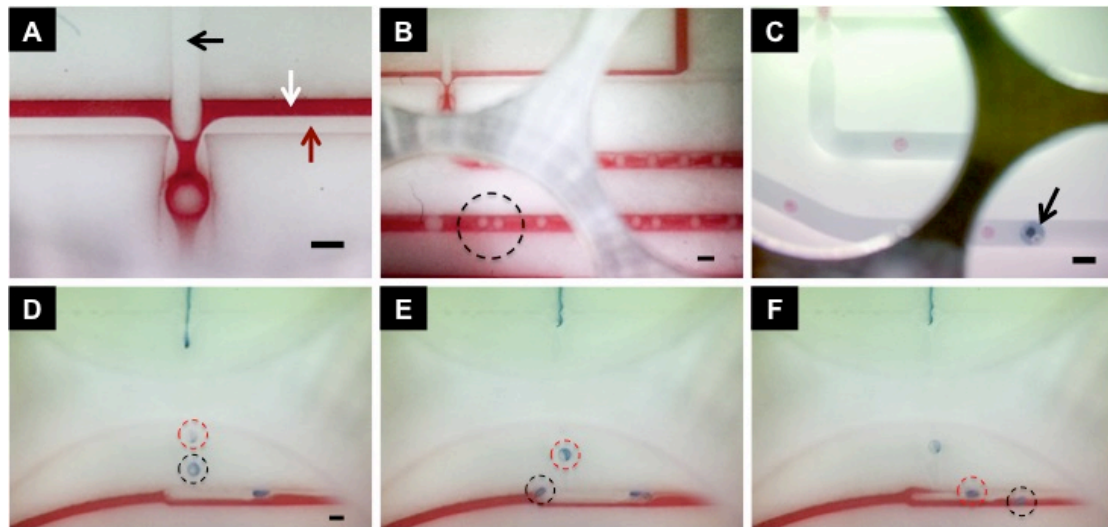


Figure 4.5 Three approaches for alginate microspheres gelation on chip. **A, B.** Shielding flow for the alginate gelation. Experiment reproduced from reference 65. **A.** Black arrow indicates the alginate solution. White arrow indicates neat mineral oil flow. Red arrow indicates the mineral oil with acetic acid. Scale bar is 800 microns. **B.** Alginate coalescence occurred in the channel. Scale bar is 800 microns. **C.** Acetic-bearing mineral oil was injected for alginate microspheres gelation from a bottom inlet. The black arrow indicates the bottom inlet. Scale bar is 1 mm. **D-F.** Acetic-bearing mineral oil (red) was injected from lateral channel. The black circles and the red circles indicate the adjacent alginate droplets. Scale bar is 300 microns.

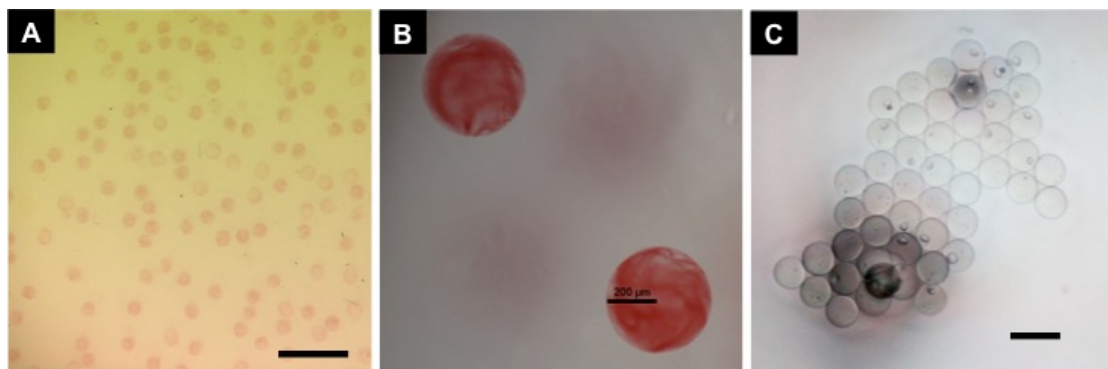


Figure 4.6 Gelled hydrogel microparticles. **A, B.** Monodispersed alginate microgels produced using the manner of Figure 5C. **A.** Scale bar is 2mm. **C.** Monodispersed PEGDA microparticles produced using the manner of Figure 5D with photopolymerization. Scale bar is 100 microns.

encapsulation using this microfluidic circuit.

4.5.3 Live and dead cell assays

The attained microgels (Figure 4.7A, B) from the experiment had an average cell density around 1 million cells/mL alginate, and were collected as separated groups in several petri dishes with several arrayed wells. Each well was prefilled with the culture medium. When the flow was collected, the alginate microgels sank to the bottom of the wells, and the oil phase rose to the top of the culture medium. The oil phase was removed manually. Then, the microgels were washed with a few strokes of culture medium using pipettes. Fluorescent images were created to detect the cell distribution in the microgels by using GFP-expressing dental pulp stem cells (Figure 4.7D). Proliferation and viability of the encapsulated mouse neuron stem cells were tested by utilising MTT assays (Figure 4.7E). The results indicated that the cells had survived the encapsulation process, and that the cell population had increased. Long-term cell viability *in vitro* (>20 days) was evaluated by other colleagues within the School of Dentistry at Cardiff University, using the same approach. Further tests such as cell transplantation and differentiation *in vivo* will be carried out in future studies.

4.6 Conclusion

In this study, we demonstrated the fabrication of monodispersed alginate microgels (average diameter around 350 microns) using planar microfluidic devices. Culture medium/alginate sheath flow was formed to control the cell density in discrete droplets by changing the input flow rate ratio rather than pre-mixing the culture medium with alginate solution. The gelation of nanocrystalline CaCO₃-bearing alginate phase was conducted on chip after droplets formation by the delivery of additional mineral oil containing acetic acid *via* two different circuit layouts. The mouse neuron stem cells encapsulated in alginate microgels showed long term viability with evidence of proliferation and without unexpected differentiation, which

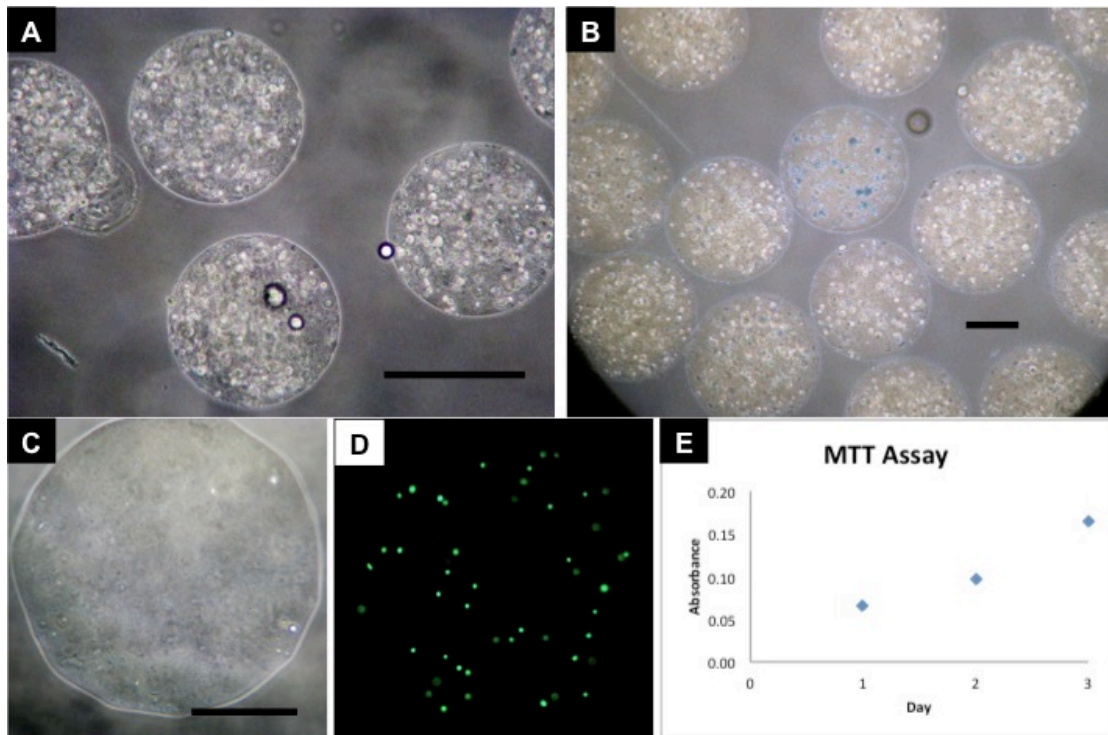


Figure 4.7 Cells encapsulation in alginate microspheres. Images were produced by Miss Lorena Hidalgo. **A, B.** Photographs of mouse neuron stem cells encapsulated in alginate microspheres. A. Scale bar is 400 microns. B. Scale bar is 250 microns. **C, D.** Fluorescence image of GFP expressing dental pulp stem cells. Scale bar is 300 microns. **E.** First 3-day viability and proliferation of the encapsulated cells in alginate microspheres were measured with MTT assay. This is evidence that the cells can stand the encapsulation process and survive inside the microgels *in vitro*.

indicates that our method is applicable for cell encapsulation *in vitro*. This will support the next stage research of stem cell therapy in the treatment of spinal cord injury. In addition, monodispersed PEGDA microspheres were formed in the same mechanism and gelled with UV polymerization, with the minimum diameter of the samples being reduced to 70 microns. As PEG was reported to have protective effect on the repair of damaged neuron membranes in rat's spinal cord, the biocompatible and biodegradable PEGDA might be an alternative material that can be employed for the neural stem cell encapsulation [68].

References:

1. Chin, S., and Lawrence, M. D., "Spinal cord injuries," *Medscape*, 2014.
2. The National SCI Statistical Center. *Facts and Figures at A Glance*. Birmingham: University of Alabama, 1999.
3. Mcintosh, T. K., Juhler, M., Wieloch, T., "Novel pharmacologic strategies in the treatment of experimental traumatic brain injury: 1998," *Journal of Neurotrauma*, vol. 15, no. 10, pp. 731-769, 1998.
4. Lee, J. M., Zipfel, G. J., and Choi, D. W., "The changing landscape of ischaemic brain injury mechanisms," *Nature*, vol. 399, pp. 7-14, 1999.
5. Matute, C., Sánchez-Gómez, M. V., Martínez-Millán, L., and Miledi, R., "Glutamate receptor-mediated toxicity in optic nerve oligodendrocytes," *Proceedings of the National Academy of Sciences*, vol. 94, no. 16, pp. 8830-8835, 1997.
6. McDonald, J. W., Althomsons, S. P., Hyrc, K. L., Choi, D. W., and Goldberg, M. P., "Oligodendrocytes from forebrain are highly vulnerable to AMPA/kainate receptor-mediated excitotoxicity," *Nature Medicine*, vol. 4, no. 3, pp. 291-297, 1998.
7. Tator, C. H., and Koyanagi, I., "Vascular mechanisms in the pathophysiology of human spinal cord injury," *Journal of Neurosurgery*, vol. 86, no. 3, pp. 483-492, 1997.
8. Waters, R. L., Sie, I., Adkins, R. H., and Yakura, J. S., "Injury pattern effect on motor recovery after traumatic spinal cord injury," *Archives of Physical Medicine and Rehabilitation*, vol. 76, no. 5, pp. 440-443, 1995.
9. Marino, R. J., Ditunno, J. F., Donovan, W. H., and Maynard, F., "Neurologic recovery after traumatic spinal cord injury: data from the Model Spinal Cord Injury Systems," *Archives of Physical Medicine and Rehabilitation*, vol. 80, no. 11, pp. 1391-1396, 1999.
10. Vaccaro, A. R., and Singh, K., "Pharmacologic treatment and surgical timing for spinal cord injury," *Current Opinion in Orthopaedics*, vol. 10, no. 2, pp. 112-116, 1999.
11. Dimar, J. R., Glassman, S. D., Raque, G. H., Zhang, Y. P., and Shield, C. B., "The influence of spinal canal narrowing and timing of decompression on neurologic recovery after spinal cord contusion in a rat model," *Spine*, vol. 24, no. 16, p. 1623, 1999.
12. Bracken, M. B., Shepard, M. J., Collins, W. F., Holford, T. R., Young, W., Baskin, D. S., Eisenberg, H. M., Flamm, E., Leo-Summers, L., Maroon, J., Marshall, L. F., Perot, P. L., Piepmeier, J., Sonntag, V. K. H., Wagner, F. C., Wilberger, J. E., and Winn, H. R., "A randomized, controlled trial of methylprednisolone or naloxone in the treatment of acute spinal-cord injury: results of the Second National Acute Spinal Cord Injury Study," *New England Journal of Medicine*, vol. 322, no. 20, pp. 1405-1411, 1990.
13. Heiden, J. S., Weiss, M. H., Rosenberg, A. W., Apuzzo, M. L. J., and Kurze, T., "Management of cervical spinal cord trauma in Southern California," *Journal of Neurosurgery*, vol. 43, no. 6, pp. 732-736, 1975.
14. Marshall, L. F., Knowlton, S., Garfin, S. R., Klauber, M. R., Eisenberg, H. M., Kopaniky, D., Miner, M. E., Tabbador, K., and Clifton, G. L., "Deterioration following spinal cord injury: a multicenter study," *Journal of Neurosurgery*, vol. 66, no. 3, 400-404, 1987.

15. Vaccaro, A. R., Daugherty, R. J., Sheehan, T. P., Dante, S. J., Cotler, J. M., Balderston, R. A., Herbison, G. J., and Northrup, B. E., "Neurologic outcome of early versus late surgery for cervical spinal cord injury," *Spine*, vol. 22, no. 22, pp. 2609-2613, 1997.
16. Chen, T. Y., Dickman, C. A., Eleraky, M., and Sonntag, V. K. H., "The role of decompression for acute incomplete cervical spinal cord injury in cervical spondylosis," *Spine*, vol. 23, no. 22, pp. 2398-2403, 1998.
17. Mirza, S. K., Krengel, W. F., Chapman, J. R., Anderson, P. A., Bailey, J. C., Grady, M. S., and Yuan, H. A., "Early versus delayed surgery for acute cervical spinal cord injury," *Clinical Orthopaedics and Related Research*, vol. 359, pp. 104-114, 1999.
18. Keith, M. W., Kilgore, K. L., Peckham, P. H., Wuolle, K. S., Creasey, G., and Lemay, M., "Tendon transfers and functional electrical stimulation for restoration of hand function in spinal cord injury," *The Journal of Hand Surgery*, vol. 21, no. 1, pp. 89-99, 1996.
19. Scremin, A. M. E., Kurta, L., Gentili, A., Wiseman, B., Perell, K., Kunkel, C., and Scremin, O. U., "Increasing muscle mass in spinal cord injured persons with a functional electrical stimulation exercise program," *Archives of Physical Medicine and Rehabilitation*, vol. 80, no. 12, pp. 1531-1536, 1999.
20. Nash, M. S., Montalvo, B. M., and Applegate, B., "Lower extremity blood flow and responses to occlusion ischemia differ in exercise-trained and sedentary tetraplegic persons," *Archives of Physical Medicine and Rehabilitation*, vol. 77, no. 12, pp. 1260-1265, 1996.
21. Schwab, M. E., and Bartholdi, D., "Degeneration and regeneration of axons in the lesioned spinal cord," *Physiological Reviews*, vol. 76, no. 2, pp. 319-370, 1996.
22. Thomson, J. A., Itskovitz-Eldor, J., Shapiro, S. S., Waknitz, M. A., Swiergiel, J. J., Marshall, V. S., and Jones, J. M., "Embryonic stem cell lines derived from human blastocysts," *Science*, vol. 282, no. 5391, pp. 1145-1147, 1998.
23. Shambloott, M. J., Axelman, J., Wang, S., Bugg, E. M., Littlefield, J. W., Donovan, P. J., Blumenthal, P. D., Huggins, G. R., and Gearhart, J. D., "Derivation of pluripotent stem cells from cultured human primordial germ cells," *Proceedings of the National Academy of Sciences*, vol. 95, no. 23, pp. 13726-13731, 1998.
24. Donovan, P. J., and Gearhart, J., "The end of the beginning for pluripotent stem cells," *Nature*, vol. 414, no. 6859, pp. 92-97, 2001.
25. Marshak, D. R., Gardner, R. L., and Gottlieb, D., *Stem Cell Biology*, Cold Spring Harbor, NY: Cold Spring Harbor Laboratory Press, 2001.
26. Smith, A., "Cell therapy: in search of pluripotency," *Current Biology*, vol. 8, no. 22, pp. 802-804, 1998.
27. McKay, R., "Stem cells in the central nervous system," *Science*, vol. 276, no. 5309, pp. 66-71, 1997.
28. Gage, F. H., "Mammalian neural stem cells," *Science*, vol. 287, no. 5457, pp. 1433-1438, 2000.
29. Gottlieb, D. I., "Large-scale sources of neural stem cells," *Annual Review of Neuroscience*, vol. 25, no. 1, pp. 381-407, 2002.
30. Kim, S. U., "Human neural stem cells genetically modified for brain repair in neurological disorders," *Neuropathology*, vol. 24, no. 3, pp. 159-171, 2004.
31. Flax, J. D., Aurora, S., Yang, C., Simonin, C., Wills, A. M., Billingham, L. L., Jendoubi, M., Sidman, R. L., Wolfe, J. H., Kim, S. U., and Snyder, E. Y.,

- “Engraftable human neural stem cells respond to development cues, replace neurons, and express foreign genes,” *Nature Biotechnology*, vol. 16, no. 11, pp. 1033-1039, 1998.
32. Svendsen, C. N., ter Borg, M. G., Armstrong, R. J., Rosser, A. E., Chandran, S., Ostenfeld, T., Caldwell, M. A., “A new method for the rapid and long-term growth of human neural precursor cells,” *J Neurosci Methods*, vol. 85, pp.141-52, 1998
 33. Carpenter, M. K., Winkler, C., Fricker, R., Emerich, D. F., Wong, S. C., Greco, C., Chen, E. Y., Chu, Y., Kordower, J. H., Messing, A., Björklund, A., Hammang, J. P., “Generation and transplantation of EGF-responsive neural stem cells derived from GFAP-hNGF transgenic mice”, *Exp. Neurol.*, vol. 148, pp. 187-204, 1997.
 34. Brüstle, O., Choudhary, K., Karram, K., Huttner, A., Murray, K., Dubois, M., and McKay, R. D. G., “Chimeric brains generated by intraventricular transplantation of fetal human brain cells into embryonic rats,” *Nature Biotechnology*, vol. 16, no. 11, pp. 1040-1044, 1998.
 35. Tuszynski, M. H., Peterson, D. A., Ray, J., Baird, A., Nakahara, Y., and Gages, F. H., “Fibroblasts genetically modified to produce nerve growth factor induce robust neuritic ingrowth after grafting to the spinal cord,” *Experimental Neurology*, vol. 126, no. 1, pp. 1-14, 1994.
 36. Xu, X. M., Guénard, V., Kleitman, N., Aebischer, P., and Bunge, M. B., “A combination of BDNF and NT-3 promotes supraspinal axonal regeneration into Schwann cell grafts in adult rat thoracic spinal cord,” *Experimental Neurology*, vol. 134, no. 2, pp. 261-272, 1995.
 37. Li, Y., Field, P. M., and Raisman, G., “Repair of adult rat corticospinal tract by transplants of olfactory ensheathing cells,” *Science*, vol. 277, no. 5334, pp. 2000-2002, 1997.
 38. Liu, Y., Kim, D., Himes, B. T., Chow, S. Y., Schallert, T., Murray, M., Tessler, A., and Fischer, I., “Transplants of fibroblasts genetically modified to express BDNF promote regeneration of adult rat rubrospinal axons and recovery of forelimb function,” *The Journal of Neuroscience*, vol. 19, no. 11, pp. 4370-4387, 1999.
 39. Teng, Y. D., Lavik, E. B., Qu, X., Park, K. I., Ourednik, J., Zurakowski, D., Langer, R., and Snyder, E. Y., “Functional recovery following traumatic spinal cord injury mediated by a unique polymer scaffold seeded with neural stem cells,” *Proceedings of the National Academy of Sciences*, vol. 99, no. 5, pp. 3024-3029, 2002.
 40. Noble, L. J., and Wrathall, J. R., “Correlative analyses of lesion development and functional status after graded spinal cord contusive injuries in the rat,” *Experimental Neurology*, vol. 103, no. 1, pp. 34-40, 1989.
 41. Fehlings, M. G., and Tator, C. H., “The relationships among the severity of spinal cord injury, residual neurological function, axon counts, and counts of retrogradely labeled neurons after experimental spinal cord injury,” *Experimental Neurology*, vol. 132, no. 2, pp. 220-228, 1995.
 42. Basso, D. M., Beattie, M. S., and Bresnahan, J. C., “Graded histological and locomotor outcomes after spinal cord contusion using the NYU weight-drop device versus transection,” *Experimental Neurology*, vol. 139, no. 2, pp. 244-256, 1996.
 43. McDonald, J. W., Liu, X. Z., Qu, Y., Liu, S., Mickey, S. K., Turetsky, D., Gottlieb, D. I., and Choi, D. W., “Transplanted embryonic stem cells survive,

- differentiate and promote recovery in injured rat spinal cord,” *Nature Medicine*, vol. 5, no. 12, pp. 1410-1412, 1999.
44. Hofstetter, C. P., Schwarz, E. J., Hess, D., Widenfalk, J., Manira, A. E. I., Prockop, D. J., and Olson, L., “Marrow stromal cells form guiding strands in the injured spinal cord and promote recovery,” *Proceedings of the National Academy of Sciences*, vol. 99, no. 4, pp. 2199-2204, 2002.
 45. Ogawa, Y., Sawamoto, K., Miyata, T., Miyao, S., Watanabe, M., Nakamura, M., Bregman, B. S., Koike, M., Uchiyama, Y., Toyama, Y., and Okano, H., “Transplantation of *in vitro*-expanded fetal neural progenitor cells results in neurogenesis and functional recovery after spinal cord contusion injury in adult rats,” *Journal of Neuroscience Research*, vol. 69, no. 6, pp. 925-933, 2002.
 46. Cao, Q., Xu, X. M., DeVries, W. H., Enzmann, G. U., Ping, P., Tsoulfas, P., Wood, P. M., Bunge, M. B., and Whitemore, S. R., “Functional recovery in traumatic spinal cord injury after transplantation of multilineurotrophin-expressing glial-restricted precursor cells,” *The Journal of Neuroscience*, vol. 25, no. 30, pp. 6947-6957, 2005.
 47. Cummings, B. J., Uchida, N., Tamaki, S. J., Salazar, D. L., Hooshmand, M., Summers, R., Gage, F. H., and Anderson, A. J., “Human neural stem cells differentiate and promote locomotor recovery in spinal cord-injured mice,” *Proceedings of the National Academy of Sciences of the United States of America*, vol. 102, no. 39, pp. 14069-14074, 2005.
 48. Keirstead, H. S., Nistor, G., Bernal, G., Totoiu, M., Cloutier, F., Sharp, K., and Steward, O., “Human embryonic stem cell-derived oligodendrocyte progenitor cell transplants remyelinate and restore locomotion after spinal cord injury,” *The Journal of Neuroscience*, vol. 25, no. 19, pp. 4694-4705, 2005.
 49. Iwanami, A., Kaneko, S., Nakamura, M., Kanemura, Y., Mori, H., Kobayashi, S., Yamasaki, M., Momoshima, S., Ishii, H., Ando, K., Tanioka, Y., Tamaoki, N., Nomura, T., Toyama, Y., and Okano, H., “Transplantation of human neural stem cells for spinal cord injury in primates,” *Journal of Neuroscience Research*, vol. 80, no. 2, pp. 182-190, 2005.
 50. Karimi-Abdolrezaee, S., Eftekharpour, E., Wang, J., Morshead, C. M., and Fehlings, M. G., “Delayed transplantation of adult neural precursor cells promotes remyelination and functional neurological recovery after spinal cord injury,” *The Journal of Neuroscience*, vol. 26, no. 13, pp. 3377-3389, 2006.
 51. Xu, L., Yan, J., Chen, D., Welsh, A. M., Hazel, T., Johe, K., Hatfield, G., and Koliatsos, V. E., “Human neural stem cell grafts ameliorate motor neuron disease in SOD-1 transgenic rats,” *Transplantation*, vol. 82, no. 7, pp. 865-875, 2006.
 52. Benn, S. C., and Woolf, C. J., “Adult neuron survival strategies-slammung on the brakes,” *Nature Reviews Neuroscience*, vol. 5, no. 9, pp. 686-700, 2004.
 53. Yuan, J., and Yankner, B. A., “Apoptosis in the nervous system,” *Nature*, vol. 407, no. 6805, pp. 802-809, 2000.
 54. Snyder, E. Y., Deitcher, D. L., Walsh, C., Arnold-Aldea, S., Hartweg, E. A., and Cepko, C. L., “Multipotent neural cell lines can engraft and participate in development of mouse cerebellum,” *Cell*, vol. 68, no. 1, pp. 33-51, 1992.
 55. Martínez-Serrano, A., and Björklund, A., “Immortalized neural progenitor cells for CNS gene transfer and repair,” *Trends in Neurosciences*, vol. 20, no. 11, pp. 530-538, 1997.

56. Lee, H. J., Kim, K. S., Kim, E. J., Choi, H. B., lee, K. H., Park, I. H., Ko, H., Jeong, S. W., and Kim, S. U., "Brain transplantation of immortalized human neural stem cells promotes functional recovery in mouse intracerebral hemorrhage stroke model," *Stem Cells*, vol. 25, no. 5, pp. 1204-1212, 2007.
57. Youdim, M. B. H., and Buccafusco, J. J., "Multi-functional drugs for various CNS targets in the treatment of neurodegenerative disorders," *Trends in Pharmacological Sciences*, vol. 26, no. 1, pp. 27-35, 2005.
58. Nicodemus, G. D., and Bryant, S. J., "Cell encapsulation in biodegradable hydrogels for tissue engineering applications," *Tissue Engineering Part B: Reviews*, vol. 14, no. 2, pp. 149-165, 2008.
59. McDonald, J. W., "Repairing the damaged spinal cord," *Scientific American-American Edition*, vol. 281, pp. 64-73, 1999.
60. Svendsen, C. N., and Smith, A. G., "New prospects for human stem-cell therapy in the nervous system," *Trends in Neurosciences*, vol. 22, no. 8, pp. 357-364, 1999.
61. Workman, V. L., Dunnett, S. B., Kille, P., and Palmer, D. D., "Microfluidic chip-based synthesis of alginate microspheres for encapsulation of immortalized human cells," *Biomicrofluidics*, vol. 1, no. 1, pp. 141-145, 2007.
62. Wieduwild, R., Krishnan, S., Chwalek, K., Boden, A., Nowak, M., Drechsel, D., Werner, C., and Zhang, Y., "Noncovalent Hydrogel Beads as Microcarriers for Cell Culture," *Angewandte Chemie International Edition*, vol. 54, no. 13, pp. 3962-3966, 2015.
63. Yu, L., Chen, M. C., and Cheung, K. C., "Droplet-based microfluidic system for multicellular tumor spheroid formation and anticancer drug testing," *Lab On A Chip*, vol. 10, no. 18, pp. 2424-2432, 2010.
64. Freeman, T. B., Cicchetti, F., Hauser, R. A., Deacon, T. W., Li, X. J., Hersch, S. M., Nauert, G. M., Sanberg, P. R., Kordower, J. H., Saporta, S., Isacson, O., "Transplanted fetal striatum in Huntington's disease: phenotypic development and lack of pathology," *Proceeding of the National Academy Sciences*, vol. 97, no. 25, pp.13877-13882, 2000.
65. Anderson, D. J., "Stem cells and pattern formation in the nervous system: the possible versus the actual," *Neuron*, vol. 30, no. 1, pp. 19-35, 2001.
66. Aboody, K. S., Brown, A., Rainov, N. G., Bower, K. A., Liu, S., Yang, W., Small, J. E., Herrlinger, U., Ourednik, V., Black, P. M., Breakefield, X. O., and Snyder, E. Y., "Neural stem cells display extensive tropism for pathology in adult brain: evidence from intracranial gliomas," *Proceedings of the National Academy of Sciences*, vol. 97, no. 23, pp. 12846-12851, 2000.
67. Matzinger, P., "The danger model: a renewed sense of self," *Science*, vol. 296, No. 5566, pp. 301-305, 2002.
68. Kouhzaei, S., Rad, I., Mousavidoust, S., and Mobasheri, H., "Protective effect of low molecular weight polyethylene glycol on the repair of experimentally damaged neural membranes in rat's spinal cord," *Neurological Research*, vol.35, no. 4, pp. 415-423, 2013.

CHAPTER V

Encapsulated Droplet Interface Bilayers *via* Droplet Microfluidics

5.1 Synthetic biology

The term “synthetic biology” was first mentioned by Stéphane Leduc in his publications at the beginning of the twentieth century [1]. In the last few decades, through rapid progress in molecular biology, scholars have gained a greatly enhanced understanding of the building blocks of life through the study of gene sequences. Synthetic biology is considered to be the next challenge for the bioscientists, who aim to synthesize artificial organisms by using devised genomes [2]. In the late 1970s, Arber, Nathans and Smith discovered the restriction enzymes that not only permit the processing and analysis of a single gene sequence, but also enable the construction and evaluation of novel genes by rearranging existing DNA molecules [3].

Nowadays, synthetic biology is an interdisciplinary subject that envelopes molecular biology, system biology, genetic biology, computer science, and microengineering [4]. Metaphorically, biologists learn about living organisms by building them rather than by tearing them apart. Synthesizing an artificial organism requires standardization and modification of the basic biological units. Biomolecular and genome engineering allows the fabrication of oligonucleotides, recreation of devised DNA sequences, and the programming of biological components from non-living substances. Those components are assembled as a circuit to form a complicated biological system, which performs high-level functionalities such as chemical transformation and information processing [5]. The ultimate goal of synthetic biology is to fabricate biological devices with special functionalities for practical applications such as drug discovery, targeted therapy, material fabrication, food production, and energy generation [6].

Several milestones of synthetic biology have come of age. The genetic toggle switch and the repressilator were the first synthetic gene networks to perform

computing and logical behaviors in biological systems, and are inspired by electronics. [7, 8] In these frameworks, basic transcriptional regulatory elements were designed and assembled to realize the biological equivalents of electronic memory storage and timekeeping, and they have been applied in the construction of genetic switches [9], memory elements [10], oscillators [11], pulse generators [12], digital logic gates [13] and communication modules [14]. In addition, a new therapeutic platform has been established for disease mechanism identification, therapeutic targeting, and drug delivery and treatment by rational and model-guided construction of biological parts. [15-17] For instance, gene therapy has shown promising advances in clinical treatment due to the construction of non-native pathways, and it provides unique and versatile approaches for studying metabolic networks and disorders, as well as accelerating drug discovery [18]. Gene therapy is more effective in the treatment of hereditary and metabolic disease, in comparison with traditional drug therapy. Moreover, synthetic biology tools have been exploited in the generation of biofuels and novel materials [16, 19]. Compared with the agricultural approach, engineered microorganisms achieve a more efficient conversion of biomass into biofuels (such as ethanol and biobutanol) by optimizing biosynthetic pathways [20, 21].

However, current progress of synthetic biology is limited by two constraints: the complexity of the biological systems, and the physical variations in biological behaviors [22]. In an organism, the biological components are sophisticated, and their interactions have not been well characterized. Bio-signal transmission is disturbed by multiple bypass pathways due to the stochastic behavior of each component [23, 24]. Those nonspecific activities induce unavoidable interferences in the process, which makes an experiment unreliable. In this case, high-throughput experimental methods (which accommodate a large number of complex and parallel reactions) are necessary

for acquiring reliable data in order to better understanding biological systems [25]. This is currently being realized by coupling a series of screening equipment, including microarrays, microplate readers, flow cytometers and fluorescence microscopes [26]. Nevertheless, limited sample space and lack of control over the experimental environment reduce screening efficiency, which makes synthetic biology time-consuming and expensive [27].

Microfluidics technology, also known as micro total analysis systems, provides an ideal platform to conduct biological experiments as shown in Figure 5.1.

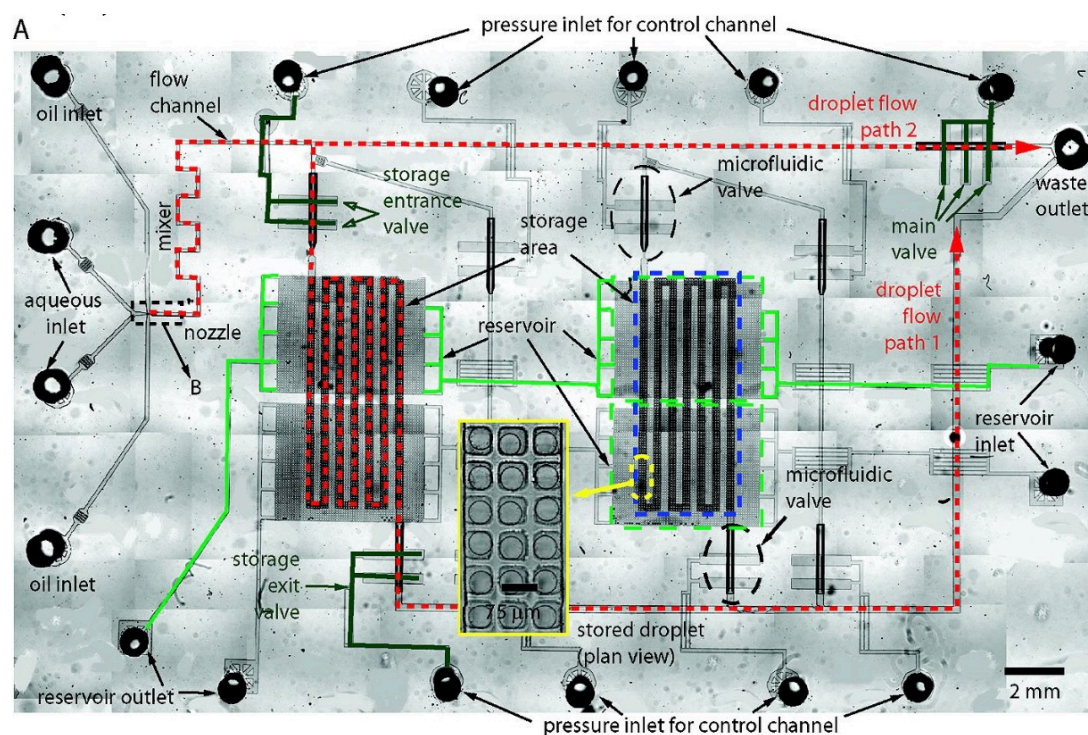


Figure 5.1 Compartment based microfluidic chip for simultaneous determination of gene expression and enzyme activity [28].

In contrast with the conventional methods, microfluidics has several unprecedented advantages, including miniaturized sample volumes, maximized sample sets, fast response, high-resolution, high-throughput, and high fidelity and precision. Droplet based microfluidics, as an important subcategory of microfluidics, is an efficient tool that is used to generate uniform, well-defined emulsion droplets, which in turn can be used as discrete microreactors to carry out a wide range of biological events, such as

cell cultivation, genetic activation, and bacterial quorum-sensing. In a devised microfluidic system, 1.5 million samples can be analyzed simultaneously in a massive docking array, and thousands of synthetic organisms can be processed every hour [29]. This largely increases the efficiency of profiling for gene expression and regulation, and accelerates the de novo construction of artificial biological systems *in vitro*. In addition, the planar microfluidic chip enables the integration of several functionalized modules on the same chassis to accommodate serial activities such as sampling, assaying and screening (as shown in Figure 5.2). Stephan and co-workers devised a microfluidic device to generate gradient fluid flow by using a complex microfluidic network to control the diffusion and concentration of biochemicals and biomolecules [30]. Song and co-workers demonstrated an optofluidics device that reduces the use of external imaging devices and light sources for chip modules [31]. Wang and co-workers developed microfluidic devices coupled with optical tweezers to study the mechanism of chemotaxis in *Escherichia coli* [33]. Compared with traditional instruments, those microfluidic modules generate more accurate and reproducible data.

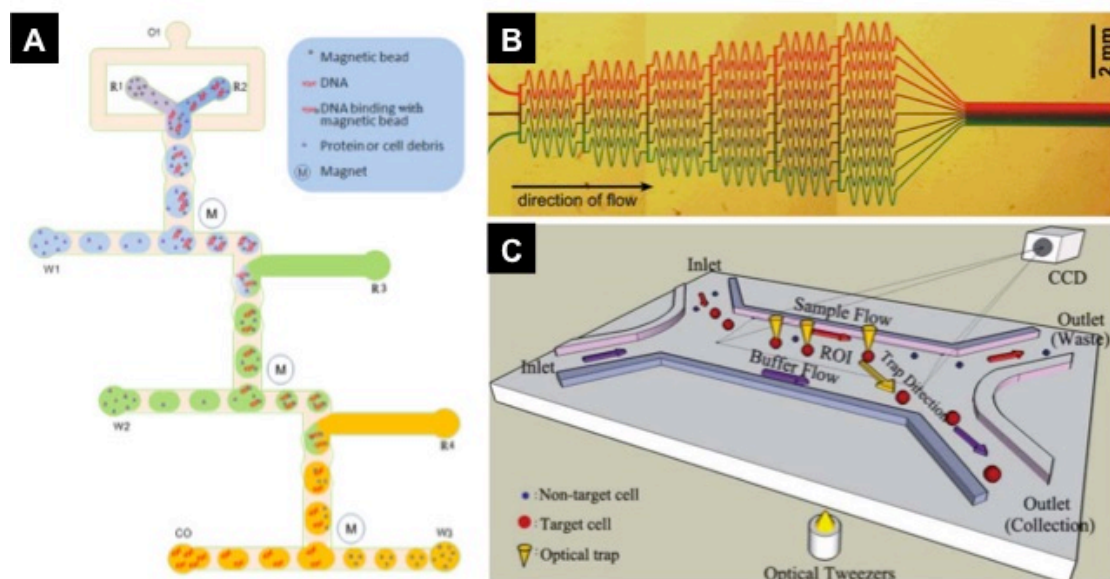


Figure 5.2 Functionalized microfluidics modules for biological researches. **A.** Schematic drawings of droplet solid phase extraction system for DNA extraction [32]. **B.** Photograph of a microfluidic device to generate fluid gradients [30]. **C.** Schematic drawing of optical tweezers utilized in microfluidics for cells and particles sorting [33].

Furthermore, a feedback loop can be devised to control the function units in microfluidic circuits, which in turn provide a programmable environment for biological experiments. This offers the facilities for specific operations such as time-lapse reactions that are necessary to ascertain the dynamics of gene networks in an organism [34]. With genome-wide data, it is possible to detect intra/extracellular metabolites [35], and perform the whole-cell analysis [36].

Synthesizing artificial cells is one of the goals of synthetic biology. An artificial cell, or prototype cell, is an engineered particle that mimics one or many functions of a biological cell such as simple metabolism, information storage, and mutation [37, 38]. The artificial protocell should in theory comprise a self-organized, endogenously ordered, spherical collection of phospholipids. Such lipid assemblies mainly appear as three structures in the solvent medium - micelle, liposome and bilayer sheet [39] - and can form membranes that in turn form enclosed compartments separating matter from the external environment (Figure 5.3). To mimic cell membrane transport systems, nuclear pores can be fabricated by adding specialized proteins [40, 41]. Such functionalized bilayers allow for the importation of the growth factors and exportation of waste, and they facilitate the research of metabolic activities. Droplet-based microfluidic technology is an efficient method for producing monodispersed vesicles with lipid assemblies over the droplet surface [41-43]. The key challenges affecting successful bilayer formation in microfluidics are reagent selection and the dewetting instability [44]. For instance, polymersomes are generated from water/oil/water double emulsion droplets, whereby the oil phases dissolve diblock copolymers, which in turn will form a bilayer after the oil has evaporated [45]. Based on the same emulsion templates, phospholipid vesicles can be produced using a similar approach. The morphology of vesicles can be formed as a complicated

structure (such as multiple levels, and bilayered and multiple compartments) in stepwise emulsification mechanisms.

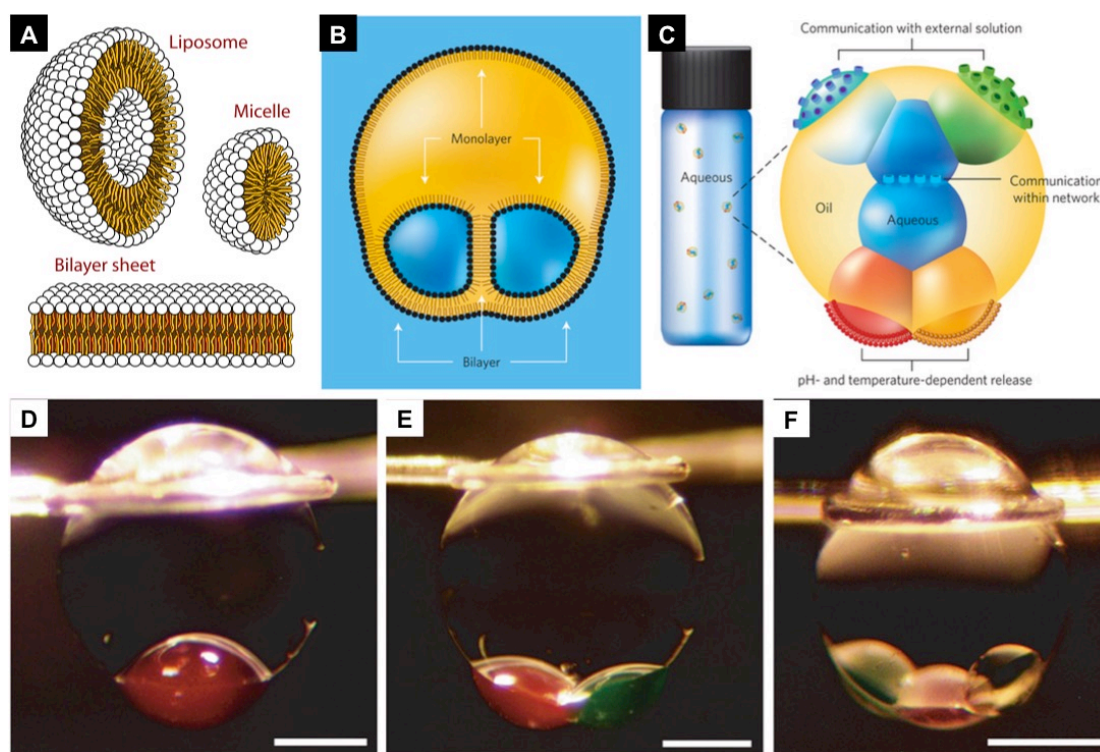


Figure 5.3 Bilayers and multisomes. A. Schematic drawing of three main structures of phospholipid assemblies in solution. B. Schematic drawing of a water/oil/water double emulsion droplet with encapsulated double interface bilayers. C. Schematic drawing of the multisomes with communication network by planting proteins in bilayers. D-F. Photographs of multisomes with diverse inner droplets [41].

In this chapter, a microfluidic approach for the mass production of encapsulated droplet interface bilayer (DIB) assemblies in freestanding oil droplets is demonstrated. The microfluidic approach of using sequential flow-focusing geometries in a micromilled PMMA chip enables precise and repeatable control over the size, number, and arrangement of internal aqueous droplets. This facilitates the high-throughput generation of encapsulated DIB assemblies that are not accessible by conventional manual pipetting or injecting methods. Crucially, this approach involves controlling the interface of the internal DIB network with the external environment *via* modulation of carrier phase hydrophilicity. By controlling the outermost continuous fluid phase in which the DIB containing oil droplets are formed, one is

able to either; (a) totally isolate the aqueous droplets of DIB assemblies from the continuous fluid environment (w/o/o), or (b) facilitate the direct interfacing of the internal aqueous droplets with the external environment through bilayers formed at the oil droplet perimeter between the internal droplets of the DIB assembly and the external aqueous environment (w/o/w) (multisomes). This approach could allow for different applications (e.g. drug screening vs. drug delivery) using the same microfluidic device. In both cases, by employing a polymerisable continuous carrier phase of TMPTA or alginate (respectively), these encapsulated DIB constructs can be fixed for prolonged storage or application in more rugged materials or structures.

5.2 The experiment

5.2.1 Solvent preparation

Lipid DPhPC was purchased from Avanti Polar Lipids and dissolved in chloroform in a vial at 10mg /ml. When preparing the oil phase solvent, the chloroform was evaporated using continuous nitrogen flow. Then, the residues were then re-solubilized in squalene and subjected to 30 minutes sonication to extrapolate the oil phase for the experiment. The DPhPC concentration in squalene was controlled within a 0.1mg/ml to 0.2mg/ml range. Oil red O was added in the oil phase to assist the observation. Deionized water was used as the water phase (with a pH value equal to 7). The continuous phase was either pure TMPTA or 3% alginate solution (as described in Chapter IV) for the preparation of the water/oil/polymer and water/oil/hydrogel double emulsions, respectively.

5.2.2 Microfluidic device fabrication

The PMMA disks were used to fabricate the planar microfluidic chips. The milling processes for the PMMA disks are the same as those used for the PTFE disks,

except that the rotating speed of the mill tools was set to 50,000 rpm, and the linear movement velocity of the pen head was set to 24mm/s to achieve a smooth surfaces without melting the PMMA. The manufactured chips did not need surface polishing, as the PMMA disks were transparent and flat. A piece of circular PMMA film (0.05mm, Goodfellow-LS421806LO) was placed over the chip, and it enclosed the microchannels for the purpose of uniform wettability.

5.2.3 Droplets generation and collection

As described in Chapter II, the double emulsion droplets were formed by the serial connected droplet forming junctions, in a two-step mechanism (shown in Figure 5.4). The attained core-shell shaped droplets were harvested either in a chamber machined in the channel or in a pool pre-filled with continuous phase off-chip (shown in Figure 5.5 C&D).

5.3 Result and discussion

5.3.1 Formation of the double emulsion droplets

Initially, monodispersed deionized water droplets were formed in neat squalene *via* a flow-focusing junction (Figure 5.4A), as the PMMA substrate is more wetted by squalene than water. The size of the water droplets was controlled by tuning the input flow-rate ratio. Next, the double emulsion droplets were formed at a bat-wing junction (Figure 5.4B,C), as the template of polymersome. Since PMMA is an acrylic monomer, an acrylate solution such as TMPTA can be employed as the continuous phase to form discrete squalene segments due to its higher surface affinity, compared with other involved phases. The bat-wing junction was employed as the second droplet forming junction to control the morphology of the double emulsion droplets. However, the water/squalene/TMPTA double emulsion was not stable in the

PMMA channel, as the water droplets were observed to be migrating from the squalene membrane (Figure 5.4D). This was due to the high interfacial tension between the water phase and squalene, whereby the spreading parameter S has a negative value (see 1.7.1.4). This issue can be solved by adding low HLB emulsifying agent, for example oleic acid and Span 80, to reduce the interfacial tension and stabilize the W/O interface. DPhPC has the same effect as those emulsifiers, and also forms a lipid monolayer over the water droplet surface. By adding 2% v/v DPhPC to the squalene, consistent water/squalene/TMPTA double emulsion droplets were formed on the PMMA microfluidic chip (Figure 5.4. E-H).

Moreover, W/O/W double emulsions were formed in the PMMA microfluidic chips to produce multisomes. To produce the multisomes, 2% v/v oleic acid was added in the aqueous continuous phase (deionized water), and the channel after the second droplet forming junction was well wetted by the continuous phase solution prior to delivery of the W/O emulsion. The number of encapsulated water droplets

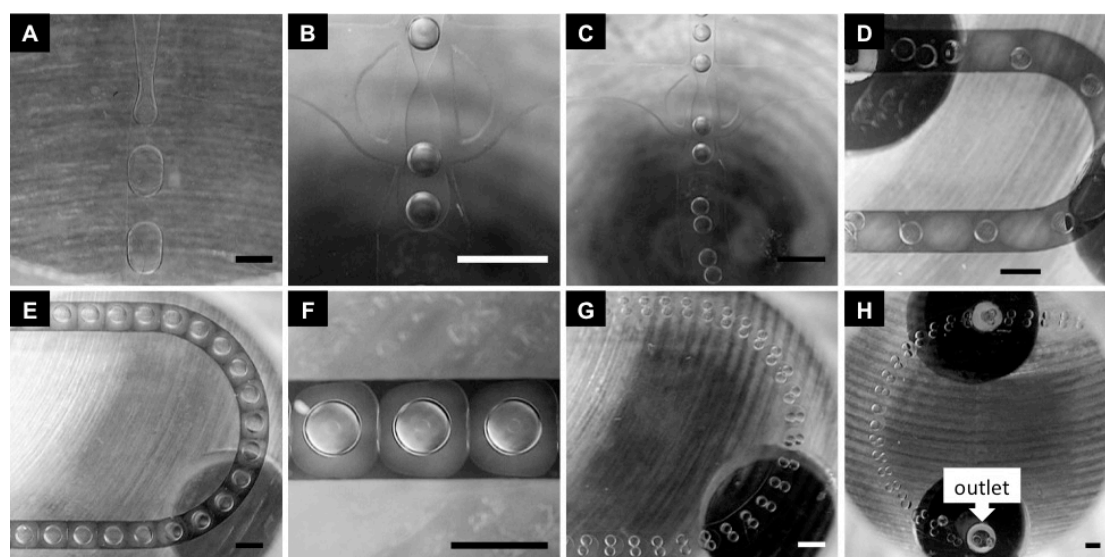


Figure 5.4 Water/squalene/TMPTA double emulsion formation on a PMMA microfluidic chip. **A.** Water droplets were sheared off by squalene phase at the first droplet-forming junction. Scale bar is 600 microns. **B, C.** Double emulsion droplets formed at the bat-wing junction. **D.** Water droplets moved out from squalene segments without DPhPC when flowed in the channel. **E, F.** With the presence of DPhPC in squalene phase, the double emulsion droplets were stabilized in the continuous flow. **G, H.** Squalene droplets with two water cores. B-H scale bars represent 1.2mm.

was controlled by the continuous phase flow rate at the bat-wing junction. An alternative continuous phase used to form W/O/W emulsions droplets on PMMA is the 3% alginate solution without surfactant. The alginate solution is highly viscous and focuses the first emulsion in the middle of channel. The breakup of W/O emulsion occurred downstream, and the multi-cored squalene droplets formed due to double emulsion droplet coalescence.

5.3.2 Bilayer formation

The next objective was to produce the droplet interface bilayer assemblies on-chip. In one attempt, two-core water/squalene/TMPTA double emulsion droplets were generated and flowed through a square-section channel to observe bilayer formation in continuous fluid flow. The input rate of the continuous phase was tuned to control the travel time of the squalene segment in the microfluidic channel. Nevertheless, all the two encapsulated water droplets in the DPhPC-bearing squalene membrane ended up coalescing in a sudden fashion, and no bilayer was formed between the water droplet interfaces.

Initially, it was considered that the DIB assembly might require the formation of a lipid monolayer around the water droplet prior to the formation of the double emulsion droplets. To test this hypothesis, the fluid delivery was cut off to allow the water droplets to remain stationary in the 2% v/v DPhPC-squalene phase for 30 minutes, before the squalene segments were sheared off at the bat-wing junction. However, the coalescence of water droplets still took place when the inflows were restarted, and the double emulsion droplets were suspended in the TMPTA phase by stopping the flow. (Figure 5.5 A,B)

Next, the two-core double emulsion droplets were collected in a devised chamber on-chip rather than being flowed through a long square section channel. The chamber had a rectangular shape with a trapezoid loft confined by the pillars. It was placed alongside the second droplet forming-junctions, and connected with the outlet. The double emulsion droplets flowed into the chamber and slowly entered the loft as the chamber zone distributed the TMPTA flow, and the pillars confined the droplet movement (in contrast with the square section channel). The bilayers were formed between the interfaces of the encapsulated water droplets when the packed squalene segments moved downward towards the outlet. (Figure 5.5 C,D) This on-chip DIB formation process is highly reproducible and DIBs can be collected in a container. (Figure 5.6) Moreover, the DIB can be assembled between the two aqueous cores containing diverse ingredients using the same approach, as shown in Figure 5.7 A-C. The number of encapsulated water droplets in squalene segments is tunable, and various layouts of DIBs can be observed (Figure 5.7 D-F). The bilayer formation in the water/squalene/alginate multisome double emulsion droplets was further investigated. As shown in the Figure 5.8, the multisomes droplets are suspended on the top of the alginate bath without coalescence, forming a tissue-like aggregates.

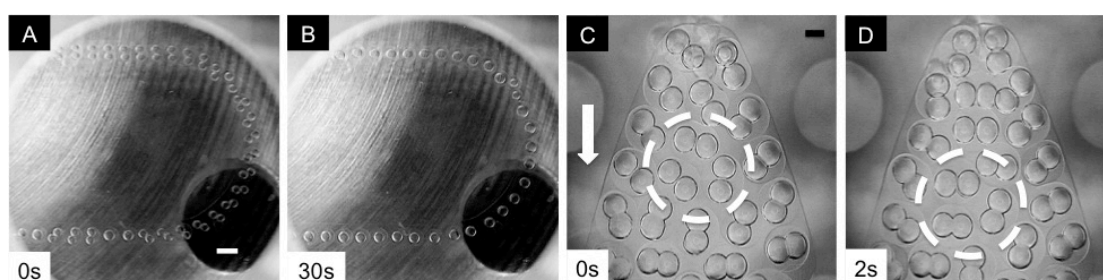


Figure 5.5 Photographs of bilayer formation on PMMA microfluidic chips. A. Two-core water/DPhDC-squalene/TMPTA double emulsion droplets stayed still in the curved PMMA channel. The white scale bar is 1.2mm. **B.** After 30s, most of the water droplets in squalene segments were coalesced to one. **C,D.** Two-core water/DPhDC-squalene/TMPTA double emulsion droplets in the devised chamber, forming bilayers at the water droplets interfaces. White arrow indicates the flow direction. The black scale bar is 250 microns.

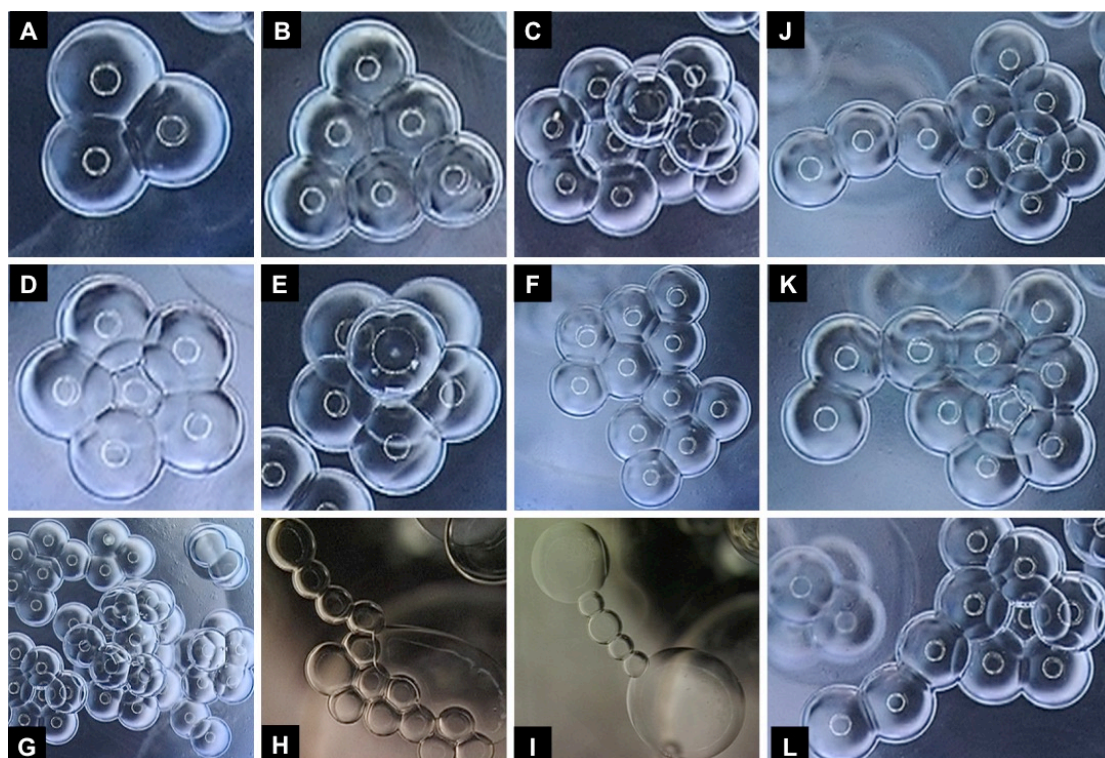


Figure 5.6 Photographs of water/DPhDC-squalene droplet interface bilayer assemblies. The diameter of water droplet units is 250 microns. **A-G.** Diverse layouts of DIB networks. The squalene double emulsion droplets were merged together, and the encapsulated DIB assemblies combined with each other and formed diverse structures. **H-I.** The DIBs were disrupted by the droplet coalescence. **J-L.** These three images focused on the same DIB network and indicated that the DIBs were flexible, which could move around the water droplet surface (as seen of the ‘tail’).

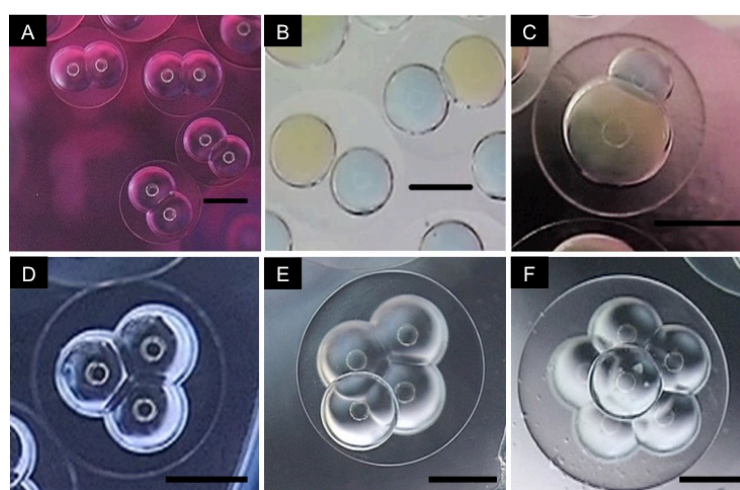


Figure 5.7 Photographs of encapsulated DIBs of water/DPhDC-squalene/TMPTA double emulsion droplets. All scale bars are 250 microns. **A.** Two-core squalene microdroplets with encapsulated DIBs that the inner droplets were same. **B, C.** Two-core squalene microdroplets with encapsulated DIBs that the inner droplets had different reagents and size. **D-F.** Diverse number of water droplets with DIBs confined in squalene droplets.

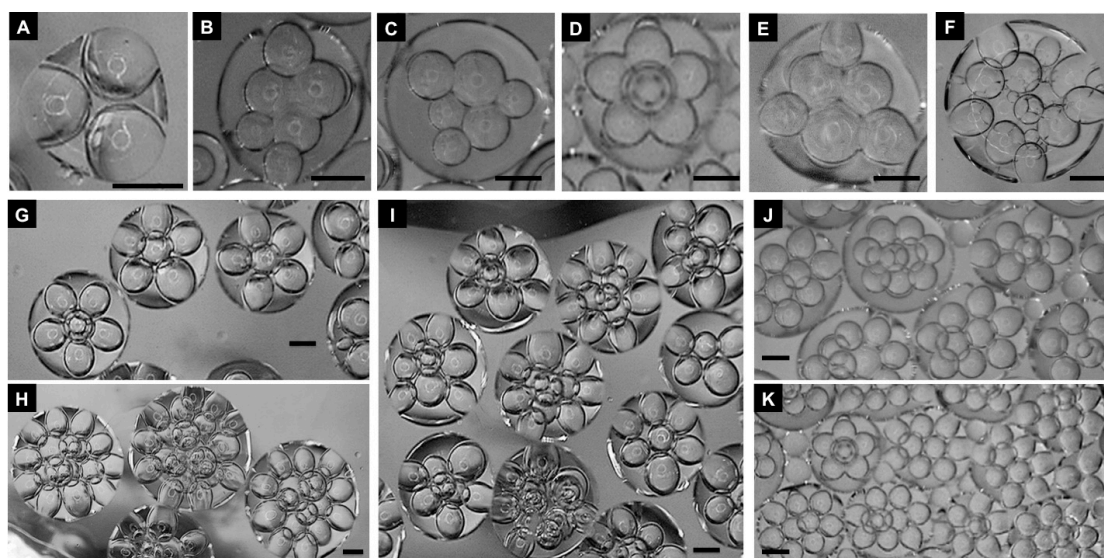


Figure 5.8 Photographs of multisomes made from the water/DPhDC-squalene/alginate double emulsion template. A-I, Diverse layouts of multisome. A, B, E, and F have shown that bilayers were formed between internal water droplets and external alginate solution. J, K. The multisomes colonized together without coalescence and formed tissue-like structure.

5.3.3 Interfacial reactions

In this section, a brief droplet motility mechanism induced by Gibbs-Marangoni instability is shown. The Marangoni instability occurs in the presence of the interfacial tension gradient in a fluid system, and causes mass transfer from a low surface tension region into a higher surface tension region (Figure 5.9). For a spherical oil droplet in a water bath, the imbalance of the interfacial tension around the droplet surface will force the droplet to move, counteracting the instability [46]. Figure 5.10 shows a typical experiment of a motile oil droplet (heavy nitrobenzene) in a high-pH water phase. The oil phase contains oleic anhydride, which can be hydrolyzed to produce two oleic acid molecules. The acid molecules lower the local pH value, and change the interfacial tension around the oil droplet to initiate its movement [47]. The convective flow inside the oil droplet brings the oleic anhydride to the interface, and this sustains its motile state [48].

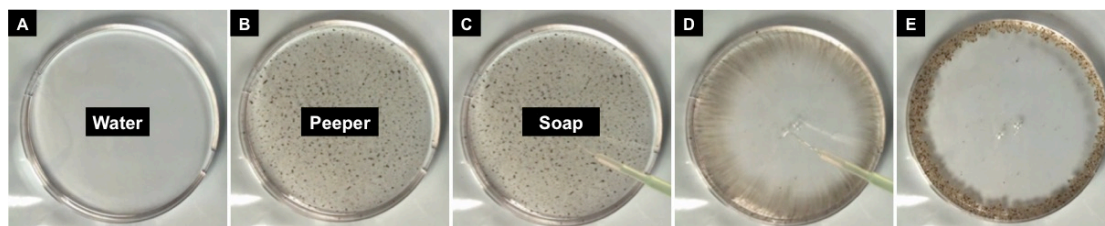


Figure 5.9 A demonstration of Marangoni effect. A, B. Pepper was evenly sprinkled into the water in a petri dish. C. A drop of soap solution was dispensed to the center of the petri dish, which will create an interfacial tension gradient. D, E. After the soap droplet was dropped into the water, Marangoni instability drove the pepper to the edge of petri dish.

In the experiment for this study, 0.5 M oleic anhydride was added to DPdHC-squalene solution in order to prepare the emulsion. The core-shell shaped double emulsion double emulsion droplets were generated, and the DIBs were formed using the same approach. At the rear end of the chamber, a bottom inlet was placed to pump another water phase in order to drive the double emulsion droplets off chip from a top outlet. At the top of the PMMA chip, an open pool, shaped by the metal scaffold, was prefilled with the water phase, which contained 10mM of oleate pH12 micelles. This

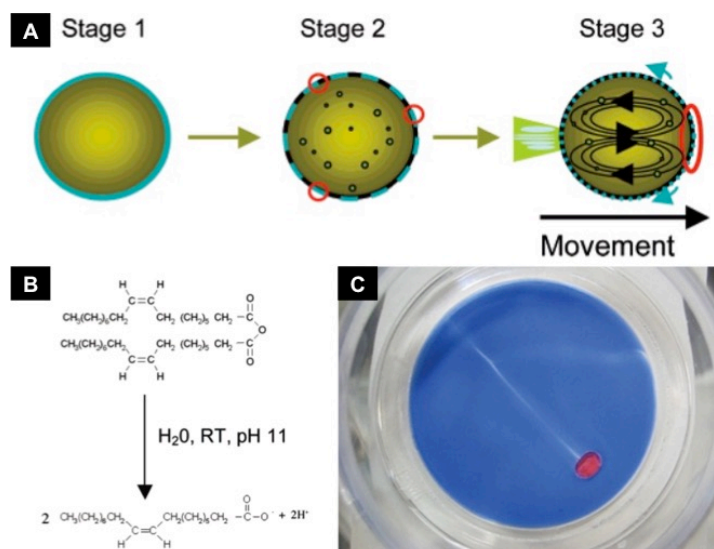


Figure 5.10 Mechanism of droplet motility in the solution environment [46-48]. A. Schematic drawing of the initial stages of oil droplet movement. Details can be found in related literature. B. Oleic anhydride was hydrolyzed in the presence of water at high pH and room temperature to form two amphiphiles. C. A demonstration of droplet (red) motility. The white line from top left to bottom right was the trail of the droplet movement, which was low pH and visualized by using pH-sensitive dye.

setup was used to investigate the interfacial reactions and the Gibbs-Marangoni effect on the squalene droplets with encapsulated DIBs.

5.3.3.1 Oil phase hydrolysis

When the double emulsion droplets with encapsulated DIB flowed to the open pool, the squalene droplets floated to the top of the solvent due to their buoyancy. The TMPTA phase accumulated at the bottom of the pool (top surface of the PMMA chip), since it is denser than the other involved fluids, and exhibits a higher affinity to the PMMA substrate. As soon as the oleic anhydride-bearing squalene membrane made contact with the oleate pH12 micelle-bearing water phase, the hydrolysis reaction took place and finished rapidly (Figure 5.11). The resulting fatty acids appeared as floccules in the aqueous solution, and was expelled from the remaining droplets to the edge of the pool. This phenomenon is evidence of the Gibbs-Marangoni effect, and

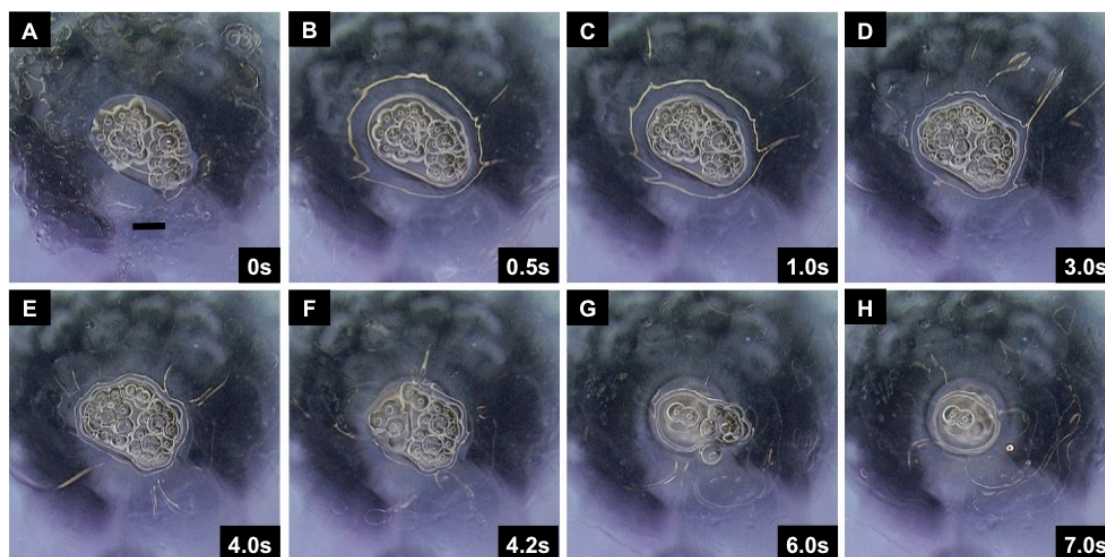


Figure 5.11 Time sequence images of the disruption of a double emulsion droplet with encapsulated DIBs. The scale bar is 500 microns. A. A squalene droplet with encapsulated DIBs flowed into the high pH water pool from a bottom inlet. **B-E.** The squalene membrane containing oleic anhydride was disrupted as soon as the hydrolyzation reaction commenced. The bright boundary indicated where the reaction occurred and the squalene segments were repelled from the droplet to the edge of pool, which was dominated by the Marangoni effect. **F-H.** When the squalene had driven away, the water droplet based DIBs network was collapsed from outside to inside.

could be utilized to remove squalene from the water droplets connected by the DIBs to produce multisomes. However, that was not achieved in this experiment, as the reaction rate was fast and no additional control was implemented on the reaction rate. When the squalene phase is torn away, the encapsulated water droplets merged with the external aqueous phase, despite the presence of the lipid monolayer. The double emulsion droplets with encapsulated DIBs exploded.

5.3.3.2 Water droplet expulsion

Further on, the input flow rate of the TMPTA phase was increased, and large globules of TMPTA containing several DIB double emulsion droplets were formed in the pool. The TMPTA phase separated the squalene droplets from the external aqueous phase to prevent hydrolyzation, as shown in Figure 5.12. When the squalene droplets migrated to the TMPTA/water interface under the influence of circulation, the hydrolysis of oleic anhydride occurred in a localized fashion at one pole of the squalene droplets. The asymmetric event induced a gradient of the interfacial tension over the squalene droplet surface, which drew out the squalene droplets from the TMPTA segment into the external water pool. The motile principle and behavior of these double emulsion droplets are the same as those of single emulsion droplets, as described in the previous literatures and as shown in Figure 5.10 A. However, the migration of the droplets produced in this experiment is predictable since the hydrolysis reaction only occurs in a confined region, whereas the motility of droplets in previous models is triggered by random droplet interface oscillation or by a self-organization of the oleic anhydride molecules (which are unpredictable). After the double emulsion droplets were expelled to the external aqueous environment, the squalene membrane was peeled off, and the encapsulated water droplets with DIBs were released (as described back in sub-section 5.3.3.1). This release mechanism

might be utilized for a smart drug delivery system or for mimicking an excretory system for building an artificial organism.

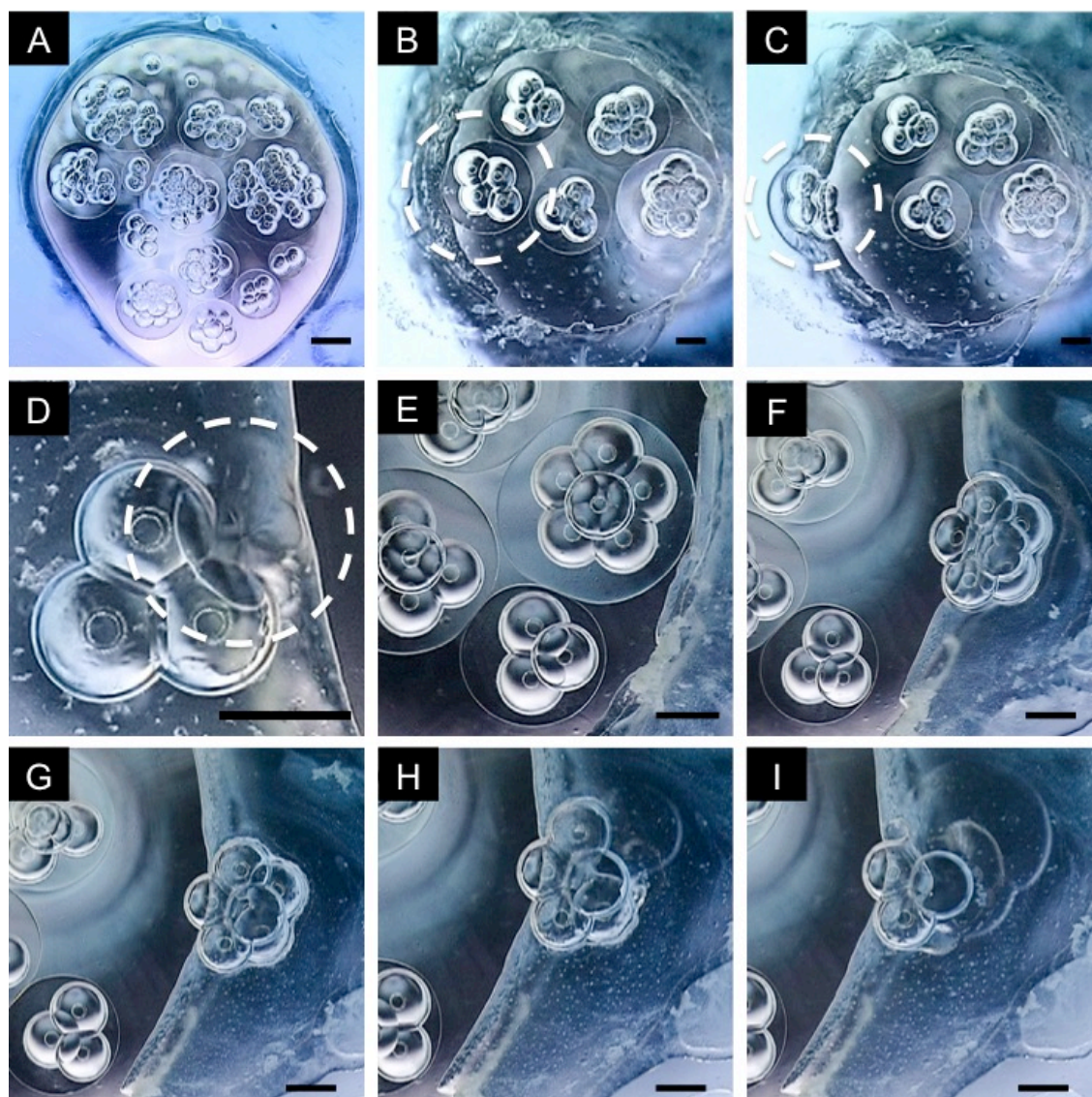


Figure 5.12 Release of squalene droplets with encapsulated DIBs. **A.** Photograph of water/squalene/TMPTA/water multiple emulsions. Scale bar is 500 microns. **B-I.** Scale bars are 250 microns. **B, C.** While the squalene droplets moved to the boundary of TMPTA and water, the hydrolyzation of oleic anhydride commenced at the interface and drew the whole squalene segment out of the TMPTA phase to the external high pH water environment. **D.** The squalene membrane was disrupted and the DIBs network began to collapse. The white dot circle showed the explosion of a water droplet. The white dusts are the product of oleic anhydride hydrolyzation. **E-I.** Sequence images of the squalene droplet release. **E.** Moving to the boundary. **F, G.** Oleic anhydride hydrolyzation and squalene membrane disruption. **H, I.** DIBs network collapse and water content release.

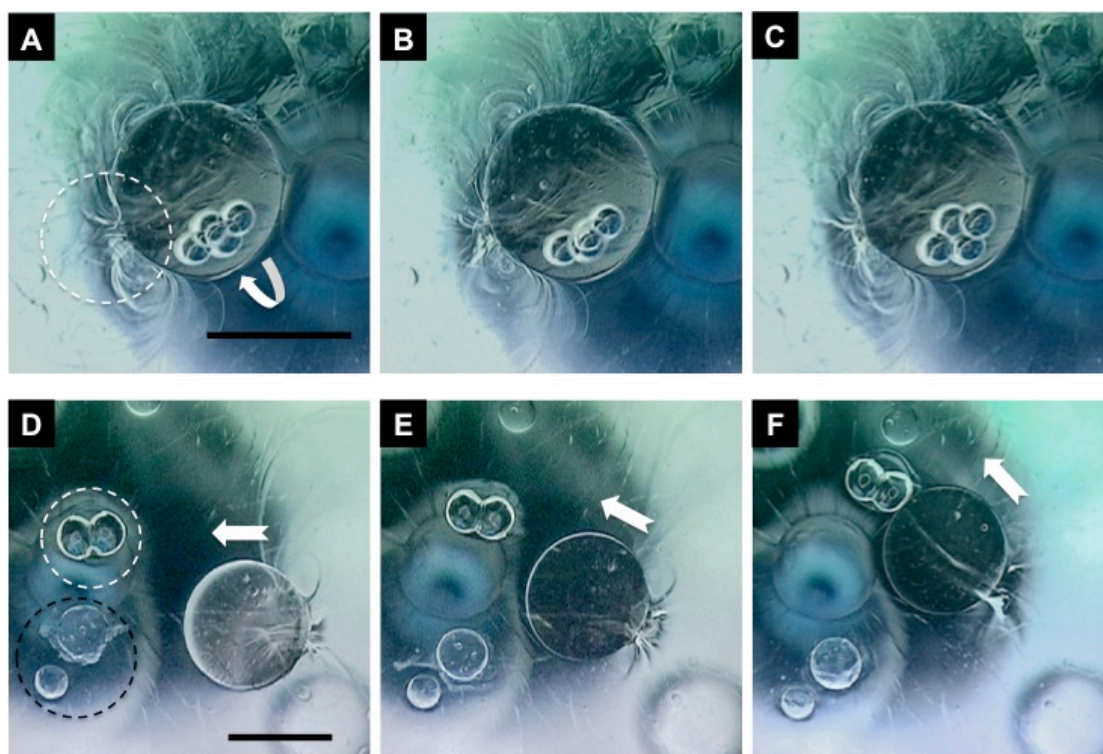


Figure 5.13 Photographs of squalene droplet motility with rotating encapsulated DIBs. **A-C.** The rotating of encapsulated DIBs network. The white arrow indicates the rotating direction of the water droplets. The water droplets would be released from the squalene droplets eventually. The white circle indicates the low pH zone that initiates the droplet movement. The scale bar is 1.5mm. **D-F.** The movement and ‘preying’ of squalene segment in high pH water solution. The squalene droplet moved towards a double emulsion droplet with encapsulated DIBs, engulf it, and released the water content. This brought more oleic anhydride molecules into the primary squalene droplets, and repeating this process sustained the motility more than 20 minutes. The white arrows indicate the moving direction of the primary squalene droplets. The white circle indicates the ‘food’. The black circle indicates other initiating squalene droplets. Somehow, they didn’t move but oscillation at the original place. The scale bar is 1.5mm.

5.3.3.3 Spinning oil droplet

In addition, the movement of an individual double emulsion droplet in the pool was investigated. Ethanol was added into the aqueous phase to reduce the interfacial tension. As shown in Figure 5.13 A-C, the convection flow was observed inside the squalene droplets, which also propelled the rotation of the water droplets with DIBs. When the water droplets moved to the low pH zone, they expelled out the squalene droplets and merged with the external water phase. This was due to a pair of

convection flows exist in activated double emulsion droplets, which has been described in previous models [29]. Furthermore, it was found that the squalene droplets, attracted by the other squalene droplets nearby, contacted with them, and eventually fusing together, thereby incorporating their encapsulated water droplets network and DIBs (Figure 5.13. D-F). In addition, the engulfed squalene droplets brought more oleic anhydride molecules to the primal droplets, which helped to sustain their motility for around 20 minutes. This simple active metabolism, made possible using droplet microfluidics, might reflect the creation of a primitive form of life, or a protocell in synthetic biology.

5.4 Conclusion

In this chapter, the generation of monodispersed water-cored squalene droplets *via* droplet microfluidics on PMMA substrates was demonstrated. The continuous phase was either an acrylate solution (TMPTA) or an aqueous solvent (3% alginate), and the rate of water droplet encapsulation was controlled by tuning the inflow ratio *via* the bat-wing junction. Following this, the formation of encapsulated DIBs on-chip proceeded, and various DIB arrangements in the squalene segments collected in a devised chamber on-chip were observed. The DIBs were not only formed between the homogenous water droplets, but could be formed between the droplets with the use of diverse volumes and reagents. Furthermore, oleic anhydride was added in the squalene phase, and the attained double emulsion droplets were sent into an alkaline environment (pH >12). The following were observed: (1) a hydrolysis reaction of oleic anhydride, and the disassembly of the squalene segments with encapsulated DIBs; (2) the motility of double emulsion droplets, and the release of water droplets with encapsulated DIBs; and, (3) the predatory behavior and growth of the primal droplet, which engulfed nearby squalene droplets to sustain its motility.

These experiments explored both the synthesis of artificial membranes, and the mimicking of simple metabolisms by the use of non-living substances *via* droplet microfluidics. The results might provide the inspiration for establishing a more complicated biological system, and may contribute to the creation of the protocell for synthetic biology research.

Reference:

1. Leduc, S., "Théorie Physico-chimique de la Vie, et Générations Spontanées," *Archives of the Roentgen Ray*, vol. 15, no. 4, pp. 160-161, 1910.
2. Szybalski, W. *In Vivo and in Vitro Initiation of Transcription*, In: A. Kohn and A. Shatky (Eds.), *Control of Gene Expression*, New York: Plenum Press, 1974, pp.23-24, 404-405, 411-412, 415-417.
3. Szybalski, W., and Skalka, A., "Nobel prizes and restriction enzymes," *Gene*, vol. 4, no. 3, p. 181, 1978.
4. Linshiz, G., Goldberg, A., Konry, T., and Hillson, N. J., "The fusion of biology, computer science, and engineering: Towards efficient and successful synthetic biology," *Perspectives in Biology and Medicine*, vol. 55, no. 4, pp. 503-520, 2012.
5. Heinemann, M., and Panke, S., "Synthetic biology-putting engineering into biology," *Bioinformatics*, vol. 22, no. 22, pp. 2790-2799, 2006.
6. Khalil, A. S., and Collins, J. J., "Synthetic biology: applications come of age," *Nature Reviews Genetics*, vol. 11, no. 5, pp. 367-379, 2010.
7. Gardner, T. S., Cantor, C. R., and Collins, J. J., "Construction of a genetic toggle switch in *Escherichia coli*," *Nature*, vol. 403, no. 6767, pp. 339-342, 2000.
8. Elowitz, M. B., and Leibler, S., "A synthetic oscillatory network of transcriptional regulators," *Nature*, vol. 403, no. 6767, pp. 335-338, 2000.
9. Atkinson, M. R., Savageau, M. A., Myers, J. T., and Ninfa, A. J., "Development of genetic circuitry exhibiting toggle switch or oscillatory behavior in *Escherichia coli*," *Cell*, vol. 113, no. 5, pp. 597-607, 2003.
10. Friedland, A. E., Lu, T. K., Wang, X., Shi, D., Church, G., and Collins, J. J., "Synthetic gene networks that count," *Science*, vol. 324 no. 5931, pp. 1199-1202, 2009.
11. Fung, E., Wong, W. W., Suen, J. K., Bulter, T., Lee, S., and Liao, J. C., "A synthetic gene-metabolic oscillator," *Nature*, vol. 435, no. 7038, pp. 118-122, 2005.
12. Basu, S., Mehreja, R., Thiberge, S., Chen, M. T., and Weiss, R., "Spatiotemporal control of gene expression with pulse-generating networks," *Proceedings of the National Academy of Sciences of the United States of America*, vol. 101, no. 17, pp. 6355-6360, 2004.
13. Anderson, J. C., Voigt, C. A., and Arkin, A. P., "Environmental signal integration by a modular AND gate," *Molecular Systems Biology*, vol. 3, no. 1, p. 133, 2007.
14. You, L., Cox, R. S., Weiss, R., and Arnold, F. H., "Programmed population control by cell - cell communication and regulated killing," *Nature*, vol. 428, no. 6985, pp. 868-871, 2004.
15. Weber, W., Schoenmakers, R., Keller, B., Gitzinger, M., and Grau, T., Baba, M. D., Sander, P., and Fussenegger, M., "A synthetic mammalian gene circuit reveals antituberculosis compounds," *Proceedings of the National Academy of Sciences*, vol. 105, no. 29, pp. 9994-9998, 2008.
16. Atsumi, S., Hanai, T., and Liao, J. C., "Non-fermentative pathways for synthesis of branched-chain higher alcohols as biofuels," *Nature*, vol. 451, no. 7174, pp. 86-89, 2008.

17. Martin, V. J. J., Pitera, D. J., Withers, S. T., Newman, J. D., and Keasling, J. D., "Engineering a mevalonate pathway in *Escherichia coli* for production of terpenoids," *Nature Biotechnology*, vol. 21, no. 7, pp. 796-802, 2003.
18. Dean, J. T., Tran, L., Beaven, S., Tontono, P., Reue, K., Dipple, K. M., and Liao, J. C., "Resistance to diet-induced obesity in mice with synthetic glyoxylate shunt," *Cell Metabolism*, vol. 9, no. 6, pp. 525-536, 2009.
19. Fernando, C. T., Liekens, A. M. L., Bingle, L. E. H., Beck, C., Lenser, T., Stekel, D. J., and Rowe, J. E., "Molecular circuits for associative learning in single-celled organisms," *Journal of the Royal Society Interface*, vol. 6, no. 34, pp. 463-469, 2009.
20. Alper, H., Fischer, C., Nevoigt, E., and Stephanopoulos, G., "Tuning genetic control through promoter engineering," *Proceedings of the National Academy of Sciences of the United States of America*, vol. 102, no. 36, pp. 12678-12683, 2005.
21. Ellis, T., Wang, X., and Collins, J. J., "Diversity-based, model-guided construction of synthetic gene networks with predicted functions," *Nature Biotechnology*, vol. 27, no. 5, pp. 465-471, 2009.
22. Vinuselvi, P., Park, S., Kim, M., Park, J. M., Kim, T., and Lee, S. K., "Microfluidic technologies for synthetic biology," *International Journal of Molecular Sciences*, vol. 12, no. 6, pp. 3576-3593, 2011.
23. Elowitz, M. B., Levine, A. J., Siggia, E. D., and Swain, P. S., "Stochastic gene expression in a single cell," *Science*, vol. 297, no. 5584, pp. 1183-1186, 2002.
24. Morange, M., "A new revolution? The place of systems biology and synthetic biology in the history of biology," *EMBO Reports*, vol. 10, no. 1S, pp. 50-53, 2009.
25. Breslauer, D. N., Lee, P. J., and Lee, L. P., "Microfluidics-based systems biology," *Molecular Biosystems*, vol. 2, no. 2, pp. 97-112, 2006.
26. Bennett, M. R., and Hastay, J., "Microfluidic devices for measuring gene network dynamics in single cells," *Nature Reviews Genetics*, vol. 10, no. 9, pp. 628-638, 2009.
27. Endy, D., "Foundations for engineering biology," *Nature*, vol. 438, no. 7067, pp. 449-453, 2005.
28. Shim, J., Olguin, L. F., Whyte, G., Scott, D., Babbie, A., Abell, C., Huck, W. T. S., and Hollfelder, F., "Simultaneous determination of gene expression and enzymatic activity in individual bacterial cells in microdroplet compartments," *Journal of the American Chemical Society*, vol. 131, no. 42, pp. 15251-15256, 2009.
29. Szita, N., Polizzi, K., Jaccard, N., and Baganz, F., "Microfluidic approaches for systems and synthetic biology," *Current Opinion in Biotechnology*, vol. 21, no. 4, pp. 517-523, 2010.
30. Jeon, N. L., Dertinger, S. K. W., Chiu, D. T., Choi, I. S., Stroock, A. D., and Whitesides, G. M., "Generation of solution and surface gradients using microfluidic systems," *Langmuir*, vol. 16, no. 22, pp. 8311-8316, 2000.
31. Song, W., Vasdekis, A. E., and Psaltis, D., "Elastomer based tunable optofluidic devices," *Lab On A Chip*, vol. 12, no. 19, pp. 3590-3597, 2012.
32. Pan, X. Y., Zeng, S. J., Zhang, Q. Y., Lin, B. C., and Qin, J. H., "Sequential microfluidic droplet processing for rapid DNA extraction," *Electrophoresis*, vol. 32, no. 23, pp. 3399-3405, 2011.

33. Ozkan, M., Wang, M., Ozkan, C., Flynn, R., and Esener, S., "Optical manipulation of objects and biological cells in microfluidic devices," *Biomedical Microdevices*, vol. 5, no. 1, pp. 61-67, 2003.
34. Locke, J. C. W., and Elowitz, M. B., "Using movies to analyse gene circuit dynamics in single cells," *Nature Reviews Microbiology*, vol. 7, no. 5, pp. 383-392, 2009.
35. Kraly, J. R., Holcomb, R. E., Guan, Q., and Henry, C. S., "Review: Microfluidic applications in metabolomics and metabolic profiling," *Analytica Chimica Acta*, vol. 653, no. 1, pp. 23-35, 2009.
36. Wakamoto, Y., Umehara, S., Matsumura, K., Inoue, I., Yasuda, K., "Development of non-destructive, non-contact single-cell based differential cell assay using on-chip microcultivation and optical tweezers," *Sensors and Actuators B: Chemical*, vol. 96, no. 3, pp. 693-700, 2003.
37. Johnson, R., "Nanoreactors: catalysis in compartments," *Nature Chemistry*, vol. 6, pp. 5-3, 2013.
38. Sakuma, Y., and Imai, M., "From vesicles to protocells: the roles of amphiphilic molecules," *Life*, vol. 5, no. 1, pp. 651-675, 2015.
39. Needham, D., "A brief history of multisomes," *Nature Nanotechnology*, vol. 6, pp. 761-762, 2011.
40. van Swaay, D., and deMello, A., "Microfluidic methods for forming liposomes," *Lab On A Chip*, vol. 13, no. 5, p. 752, 2013.
41. Villar, G., Heron, A. J., and Bayley, H., "Formation of droplet networks that function in aqueous environments," *Nature Nanotechnology*, vol. 6, no. 12, pp. 803-808, 2011.
42. Tan, Y. C., Hettiarachchi, K., Siu, M., Pan, Y. R., and Lee, A. P., "Controlled microfluidic encapsulation of cells, proteins, and microbeads in lipid vesicles," *Journal of the American Chemical Society*, vol. 128, no. 17, pp. 5656-5658, 2006.
43. Schlicht, B., and Zagnoni, M., "Droplet-interface-bilayer assays in microfluidic passive networks," *Scientific Reports*, vol. 5, pp. 1-7, 2015.
44. Perro, A., Nicolet, C., Angly, J., Lecommandoux, S., Meins, J. F. L., and Colin, A., "Mastering a double emulsion in a simple co-flow microfluidic to generate complex polymersomes," *Langmuir*, vol. 27, no. 14, pp. 9034-9042, 2010.
45. Foster, T., Dorfman, K. D., and Davis, H. T., "Giant biocompatible and biodegradable PEG-PMCL vesicles and microcapsules by solvent evaporation from double emulsion droplets," *Journal of Colloid and Interface Science*, vol. 351, no. 1, pp. 140-150, 2010.
46. Hanczyc, M. M., Toyota, T., Ikegami, T., Packard, N., and Sugawara, T., "Fatty acid chemistry at the oil-water interface: self-propelled oil droplets," *Journal of the American Chemical Society*, vol. 129, no. 30, pp. 9386-9391, 2007.
47. Hanczyc, M. M., "Metabolism and motility in prebiotic structures," *Philosophical Transactions of the Royal Society of London B: Biological Sciences*, vol. 366, no. 1580, pp. 2885-2893, 2011.
48. Hanczyc, M. M., and Ikegami, T., "Chemical basis for minimal cognition," *Artificial Life*, vol. 16, no. 3, pp. 233-243, 2010.

CHAPTER VI

Main Conclusions and Suggestions for Future Work

6.1 Main conclusions

Droplet microfluidics is a versatile and efficient tool for customized droplet synthesis and processing. Consuming limited reagents and energy, it achieves unparalleled experimental results in comparison to the conventional techniques in aspects of production uniformity, yield rate and reproducibility. With the development of fundamental devices, modules based microfluidic systems will be widely applied for droplet fabrication and analysis in various areas of science and industry.

In our work, we used affordable materials and equipment to build up our microfluidic devices and generate monodispersed multiple emulsion microdroplets, which have specific characteristics. The droplets were used to fabricate microparticles as well as carried out chemical reactions to gain advanced functionalities. The results might benefit follow-on works in future research.

In Chapter 2, we demonstrated the droplet formation mechanisms of a novel flow-focusing junction with devised layout both in the experimental work and CFD simulations. This junction, the bat-wing junction, exhibits the capabilities to control the droplet breakup point location and to eliminate satellite droplets by changing the continuous flow rate. It has been employed to generate consistent multiple emulsions and fabricate multi-cored polymeric microcapsules. The results indicate that the bat-wing junction allows more accurate control over the droplet formation, and increases the productivity of planar microfluidic chips.

In Chapter 3, we used the bat-wing junction to produce monodispersed water/TMPTA/oil double emulsion droplets for the fabrication of polymeric ICF target shells. The formation rate was reached up to 20Hz without coalescence by increasing the distance of adjacent droplets with additional continuous phase. The

attained droplets were consolidated by photoinitiated free radical polymerization. The impacts of photopolymerization kinetics on the shape of solid TMPTA microcapsules were studied. It was found that when the water/TMPTA/oil double emulsion droplets flowed upwards in the centerline of a circular capillary and were cured by evenly distributed UV irradiations (minimum exposure time 30 ms), the resulting shells possessed both good average sphericity and concentricity (both over 98.4%, best sphericity=99.69% and best concentricity=99.72%). The process was found to be highly reproducible with a 100% intact capsule yield rate, and it was possible to produce monodispersed microcapsules with relatively controllable (from 60 μm to 100 μm), uniform shell thicknesses. Furthermore, a photo-curable TMPTA-MCNT nanocomposite with fine MCNT dispersion was synthesized. The Young's module of the thin fibers formed from the functionalized TMPTA solution was higher than those formed from neat TMPTA (up to 50%). This composite can also be used to generate the double emulsions and produce intact solid microcapsules using the same process.

In Chapter 4, we demonstrated the generation of monodispersed alginate microgels (average diameter around 350 microns) with the bat-wing junction. Culture medium/alginate sheath flow was formed to control the cell density in discrete segments. The gelation of nanocrystalline CaCO_3 -bearing alginate phase was conducted on chip by injecting mineral oil containing acetic acid *via* two different circuit channel configurations. The mouse neuron stem cells encapsulated were successfully encapsulated in alginate microgels, and showed long term viability with evidence of proliferation, which indicates that the approach is applicable for stem cell encapsulation *in vitro*. This will support the next stage research of stem cell therapy in the treatment of spinal cord injury.

In chapter 5, both water/squalene/TMPTA and water/squalene/ alginate solution were produced with the bat-wing junction on PMMA substrates. Lipid (DPhPC) DIBs are formed between the encapsulated water droplets inside an on-chip chamber and various DIBs arrangements were observed. Furthermore, the double emulsion droplets were functionalized with motility by using previous models for single emulsion systems. Three phenomena were highlighted: (1) a hydrolysis reaction of oleic anhydride, and the disassembly of the squalene segments with encapsulated DIBs; (2) the motility of double emulsion droplets, and the release of water droplets with encapsulated DIBs; and, (3) the predatory behavior and growth of the primal droplet, which engulfed nearby squalene droplets to sustain its motility. These results might be exploited to create prototype cells with simple metabolic functions for the applications in synthetic biology.

6.2 Suggestion for future work.

In terms of droplet microfluidics, the difficulty to produce stable and uniform multiple emulsions are rising with the number of involved phases. The formations of high order multiple emulsions such as quadruple emulsions are still challenges to the current microfluidic devices. These multiple emulsion droplets, with multilayer and multi-compartments structures, will have large numbers of applications in the production of novel materials and processing of biochemical samples. To achieve this, future efforts may focus on the manufacture of specific microfluidic chips with controllable channel wettability. This will require surface treatment and advance fabrication technic such as 3D-printing.

For ICF target fabrication *via* droplet microfluidics, effort may focus on inner phase removal, foam shell formation, and on-the-fly cryogenic fuel filling. For stem cell encapsulation in microgels, should focus on the transplantation of cell-bearing

microgels within the SCI, and direct stem cell differentiations with controllable release of growth factors *in vivo*. For encapsulated DIBs, efforts should focus on embedding specific proteins to create nuclear pores through bilayers. These structures can mimic cell membrane transport systems for multisomes that enables the molecular and signal transfer.